INVESTIGATION OF DYNAMIC RESPONSES OF ON-ROTOR WIRELESS SENSORS FOR CONDITION MONITORING OF ROTATING MACHINES

Zainab Mones

Supervised by

Professor Andrew D. Ball and Professor Fengshou Gu

September 2018

School of Computing and Engineering

University of Huddersfield

The Author

Zainab Mones graduated from University of Benghazi, with a B.Sc. in electrical and electronic engineering in 2005 and got a M.Sc. degree in telecommunication engineering from the same University in 2008. In Oct 2014, she commenced the research on wireless condition monitoring that is presented in this thesis in the Centre for Efficiency and Performance Engineering (CEPE), School of Computing and Engineering at University of Huddersfield, UK.

List of Content

The Author 2
List of Content 3
List of Figures 7
List of Tables 12
List of Abbreviations 13
Abstract 15
Declaration 17
Acknowledgement 18
Publications 19
CHAPTER 1 INTRODUCTION 21
1.1 Maintenance Strategies and Condition Monitoring 22
1.1.1 Corrective Maintenance 22
1.1.2 Periodical Maintenance 23
1.1.3 Predictive Maintenance 23
1.2 Condition based Monitoring Techniques 24
1.2.1 Visual Inspection 25
1.2.2 Trend Monitoring 25
1.2.3 Performance and Behaviour Monitoring 26
1.2.4 Instantaneous Angular Speed Monitoring 27
1.2.5 Vibration Monitoring 27
1.3 Wireless Condition Monitoring 31
1.4 Research Motivation 32
1.5 Research Aim and Objectives 33
1.6 Thesis Layout 34
CHAPTER 2 DYNAMICS OF ROTATING MACHINES 36
2.1 Reciprocating Compressors 37
2.1.1 How the Reciprocating Compressor Works 38
2.1.2 Reciprocating Compressor Operation and Maintenance Costs 39
2.2 Single Stage Reciprocating Compressors 40
2.2.1 Dynamics of the Piston Mechanism 41
2.3 Multistage Reciprocating Compressor 43
2.3.1 Two Stage Reciprocating Compressor 44

2.3.1.1 Two-stage Piston and Crank Arrangement 46
2.3.1.2 Equation for Cylinder Volume 47
2.4 Reciprocating Compressors Valve Failures and its Practical Condition Monitoring 48
2.5 Gears Overview 50
2.5.1 Gears Failure 51
2.5.2 Gearbox Failure Cause 52
2.6 Planetary Gearbox 54
2.6.1 Characteristic Frequencies of Planetary Gearbox 56
2.6.2 Planetary Gearbox Characteristic Frequencies for Fault Diagnosis 57
2.6.2.1 Characteristic Frequency of Sun Gear with Local Fault 57
2.6.2.2 Characteristic Frequency of Planet Gear with Local Fault 57
2.6.2.3 Characteristic Frequency of Ring Gear with Local Fault 58
2.6.3 Planetary Gearbox Condition Monitoring 58
2.7 Summary 61
CHAPTER 3 MEMS TECHNOLOGY, WIRELESS TRANSMISSION AND ON-ROTOR SENSORS 62
3.1 Introduction 63
3.2 MEMS Devices 64
3.2.1 MEMS Accelerometer 65
3.3 Wireless Technology in Condition Monitoring 68
3.3.1 Wireless Protocols for WSN 70
3.3.1.1 WiFi over IEEE 802.11 70
3.3.1.2 ZigBee over IEEE 802.15.4 70
3.3.1.3 Bluetooth Classic and Bluetooth Low Energy over IEEE 802.15.1 71
3.4 Challenges of Remote Condition Monitoring 72
3.5 Wireless Technologies and MEMS Accelerometers for Condition Minoring 74
3.6 On-Rotor MEMS Accelerometer Measurements 76
3.6.1 Centripetal and Tangential Acceleration 78
3.6.2 Gravitational Acceleration Projection Signal 79
3.7 Tangential Acceleration Reconstruction 82
3.7.1 Performance Analysis 83
3.7.2 Error Analysis 86
3.8 Summary 88
CHAPTER 4 TEST RIG FACILITIES AND EXPERIMENTAL WORK 89
4.1 Test Rig Description 90

4.2 Measurement Transducers 92
4.2.1 Encoder 92
4.2.2 Dynamic Pressure Sensor 93
4.2.3 Static Pressure Sensor 94
4.2.4 Temperature Measurement 95
4.2.5 AX3 Data Logger 96
4.2.6 Wireless Sensor Node 98
4.3 Data Acquisition System 99
4.4 Measurement Practice, Data Management and Software for Data Processing 100
4.5 Fault Simulation and Seeding 102
4.5.1 Leaky Valve Simulation 103
4.5.2 Leak in Intercooler 104
4.5.3 Stator Asymmetries Faults 105
4.6 Summary 107
CHAPTER 5 MONITORING RC USING THE ACCELERATION RESPONSES IN TANGENTIAL DIRECTION OF THE ON-ROTOR SENSOR 108
5.1 Introduction 109
5.2 Test Procedure 109
5.3 Results and Discussion 109
5.4 Summary 116
CHAPTER 6 MONITORING RC USING ANGULAR SPEED RESPONSES FROM THE ON ROTOR SENSOR 117
6.1 Introduction 118
6.2 IAS Measurement Based on Encoder 119
6.2.1 Measurement Principle 119
6.2.2 Selection of Sensor 121
6.3 IAS Measurement Based on the On-rotor MEMS Accelerometer 121
6.3.1 Wireless Sensor Node 122
6.4 Comparison Study of IAS from Encoder and Wireless Accelerometer 122
6.4.1 Test Rig Setup 123
6.4.2 Test Procedure 124
6.5 Results and Discussion 124
6.6 Summary 130
CHAPTER 7 INVESTIGATION OF TWO APPROACHES TO THE CANCELLATION OF GRAVITATIONAL ACCELERATION BASED ON THE MONITORING OF RC CONDITIONS 131

7.1 Introduction 132
7.2 Gravitational acceleration cancellation using two MEMS sensors 133
7.3 Test Rig Facility 135
7.4 Test Procedure 136
7.5 Results and Discussion 136
7.6 Summary 140
CHAPTER 8 PLANETARY GEARBOX FAULT DETECTION AND DIAGNOSIS USING AN ON-ROTOR ACCELEROMETER 142
8.1 Introduction 143
8.2 Experimental validation 145
8.2.1 Test Rig-Setup 145
8.2.2 Fault Simulations 146
8.2.3 Test Procedure 147
8.3 Results and Discussion 147
8.4 Summary 157
CHAPTER 9 CONCLUSION AND FUTURE WORK 159
9.1 Review of Aim, Objectives and Achievements 160
9.2 Conclusions 162
9.3 Contributions to Knowledge 163
9.4 Recommended Future Work on Wireless MEMS Accelerometer 164
REFERENCES 166

List of Figures

Figure 1-1 Stages of a breakdown maintenance task. 22
Figure 1-2 Stages of a preventive maintenance task 23
Figure 1-3 Condition based maintenance main steps 25
Figure 1-4 Typical bathtub curve 26
Figure 1-5 Machinery performance 26
Figure 1-6 Wireless Technology Implementation in Industrie 32
Figure 1-7 Thesis Structure 35
Figure 2-1 Compressor Types 37
Figure 2-2 Life cycle costs of compressed-air energy use 39
Figure 2-3 (a) Single acting compressor and (b) Schematic diagram of single acting compressor 40
Figure 2-4 An ideal Pressure-Volume diagram 41
Figure 2-5 (a) Action of the gas pressure forces. (b) Forces due to gas pressure. 42
Figure 2-6 Multistage reciprocating compressors for liquid gas transfer (Source: Corken Company) 44
Figure 2-7 Schematic of a two-stage compressor 44
Figure 2-8 An ideal P-V diagram for a two-stage compressor 45
Figure 2-9 Illustration of intercooler on a two-stage reciprocating air compressor 45
Figure 2-10 Two-stage reciprocating compressor simplified model 46
Figure 2-11 Gears types: (a) Spur gear and (b) Helical gear 50
Figure 2-12 Modes of gear failure 52
Figure 2-13 Gearbox failures causes 53
Figure 2-14 Detailed analysis of gearbox failures 53
Figure 2-15 Planetary Gear Train 54
Figure 2-16 Planetary gear configuration under study 55
Figure 2-17 Planetary gear system with a single planet 59
Figure 3-1 Schematic illustration of MEMS components 65
Figure 3-2 The structure of a MEMS accelerometer 66
Figure 3-3 Accelerometer block diagram 67
Figure 3-4 Types of wireless networ 69
Figure 3-5 Acceleration analysis of a mass Q rotating around point C 77

Figure 3-6 Accelerations measurements (a) tangential acceleration and gravity signal projected on Y-axis gy in time domain (b) frequency components ..... **Error! Bookmark not defined.**
Figure 3-7 Angular speed (a) time domain waveform and (b) its representation frequency domain...84
Figure 3-8 True accelerations and their spectrum (a) centripetal acceleration ac, (b) tangential acceleration at, (c) gravity signal projected on X-axis gx and (d) gravity signal projected on Y-axis gy. 85
Figure 3-9 Processed signals and their spectrum (a) signal in X-axis ax, (b) signal in Y-axis ay and (c) true tangential signal at and the reconstructed signal atr 86
Figure 4-1 Broom-Wade TS9 RC 90
Figure 4-2 Schematic diagram of a two-stage reciprocating compressor 91
Figure 4-3 RI32 encoder sensor 93
Figure 4-4 Optical encoder raw data 93
Figure 4-5 Dynamic pressure sensor on cylinder head 94
Figure 4-6 Online pressure sensors raw data 94
Figure 4-7 Static pressure sensor on air storage tank 95
Figure 4-8 Tank pressure sensor output 95
Figure 4-9 Temperature sensor installation 95
Figure 4-10 Online thermocouple digital output 95
Figure 4-11 AX3 accelerometer 96
Figure 4-12 Picture of AX3 installation on the compressor wheel 96
Figure 4-13 Ax3 raw data 97
Figure 4-14 Installation of (I) MEMS accelerometer and (II) microcontroller board 98
Figure 4-15 CED 1401 Plus data acquisition system 99
Figure 4-16 Schematic diagram of the compressor test system 100
Figure 4-17 Set up window of data acquisition software 101
Figure 4-18 Raw data acquired from test rig 102
Figure 4-19 2nd stage discharge valve parts 103
Figure 4-20 Leak in 2nd stage discharge valve plate 104
Figure 4-21 Leak in the intercooler 104
Figure 4-22 External resistor bank 105
Figure 4-23 Schematic diagram of extrenal resistance connection 106
Figure 4-24 The effect of different fault conditions on compressor performance 106
Figure 5-1 Acceleration signal at 100 psi pressure (a) X axial (b) Y axial (c) Z axes 110

Figure 5-2 Acceleration signal and its spectra with pressure at 0.689MPa (100 psi) (a) X-axis and (b) Y-axis 111
Figure 5-3 Reconstructed signals having 0.689MPa or 80 psi as tank pressure. (a) Temporal domain and (b) frequency domain 112
Figure 5-4 Tangential acceleration at conditions of tank pressure in spectral feature modes (a) as a waterfall-plot; amplitude of (b) fundamental component, (c) 2nd harmonic, (d) 3rd harmonic and (e) 4th harmonic. 113
Figure 5-5 Amplitude corresponding to (a) fundamental frequency; (b) 2nd harmonic; (c) 3rd harmonic and (d) 4th harmonic of the reconstructed acceleration signal plotted against the tank pressure 114
Figure 5-6 3rd harmonic amplitude vs. fundamental frequency amplitude 115
Figure 5-7 Fault signal classification: residual vs. fundamental frequency 115
Figure 6-1 (a) Encoder principle and (b) operations of measuring elapsed time 120
Figure 6-2 Transmitter circuit schematic 122
Figure 6-3 IAS extraction block diagram 123
Figure 6-4 Schematic of a 2-stage reciprocating compressor along with the installation of (I) MEMS accelerometer, (II) microcontroller board and (III) optical encoder 123
Figure 6-5 Acceleration signals at pressure of 0.55 MPa (80 psi) (a) X-axis, (b) its spectra, (c) Y-axis and (d) spectra 125
Figure 6-6 Tangential acceleration at conditions of tank pressure at 0.55 MPa or 80 psi; (a) temporal domain and (b) frequency domain. 125
Figure 6-7 Spectral mode representation of tangential acceleration under tank pressures condition ranging from 0.14 MPa or 20 psi to 0.83 MPa or 120 psi, (a) as a waterfall plot; amplitude of (b) fundamental frequency; (c) 2nd harmonic; (d) 3rd harmonic and (e) 4th harmonic 126
Figure 6-8 IAS signal (in time domain) calculated using optical encoder 127
Figure 6-9 Comparison from the wireless sensor and encoder. (a) wireless sensor time domain, (b) wireless sensor frequency domain, (c) encoder signal time domain, (d) encoder signal frequency domain 127
Figure 6-10 Tangential acceleration comparison from the wireless sensor and encoder. (a) wireless sensor temporal domain, (b) wireless sensor frequency domain, (c) encoder signal temporal domain, (d) encoder signal frequency domain 128
Figure 6-11 Amplitude corresponding to (a) fundamental frequency; (b) 2nd harmonic; (c) 3rd harmonic and (d) 4th harmonic of the reconstructed acceleration signal plotted against the tank pressure 129
Figure 6-12 Plots of fault signal classification for (a) 3rd harmonic against fundamental frequency (b) residual against fundamental frequency 130

Figure 7-1Accelerations measurements (a) tangential acceleration and gravity signal projected on Y-axis gy in time domain (b) frequency components 132
Figure 7-2 Acceleration analysis of two mass (A and B) rotating around point O [145] 133
Figure 7-3 MEMS sensor sampling rate correction steps 134
Figure 7-4 MEMS accelerometers installation on the reciprocating compressor flywheel 135
Figure 7-5 The 1st On-rotor MEMS acceleration measurements and their spectra at pressure of 0.55 MPa (around 80 psi): (a) signal measured at X-axis and (b) signal measured at Y-axis 136
Figure 7-6 The 2nd On-rotor MEMS acceleration measurements and their spectra at pressure of 0.55 MPa (around 80 psi): (a) signal measured at X-axis and (b) signal measured at Y-axis 137
Figure 7-7 True tangential acceleration signals measured at tank pressure of 0.55 MPa (80 psi) and their spectra: (a) One MEMS method (b) Two MEMS method 138
Figure 7-8 The amplitude of the tangential acceleration harmonics against tank pressure: (a) fundamental, (b) second, (c) third and (d) fourth harmonics for one MEMS method 139
Figure 7-9 The amplitude of the tangential acceleration harmonics against tank pressure: (a) fundamental, (b) second, (c) third and (d) fourth harmonics for two MEMS method 139
Figure 7-10 Plots showing fault classification: (a1) 3rd harmonic against fundamental; (b1) residual against fundamental frequency [one MEMS method]; (a2) 3rd harmonic against fundamental; (b2) residual against fundamental frequency [two MEMS method] 141
Figure 8-1 On-rotor vibration measurement geometry 144
Figure 8-2 Schematic diagram of planetary gearbox test facility 145
Figure 8-3 Planetary gearbox test rig and 145
Figure 8-4 Sun Gear Tooth Fault simulation 146
Figure 8-5 Planet Gear Tooth Fault simulation 147
Figure 8-6 X-axis filtered acceleration signals and its spectra with 90% load and 30% speed for (a) Sensor 1 and (b) Sensor 2 148
Figure 8-7 Tangential acceleration signal and spectra at 30% speed and 90% load 148
Figure 8-8 Spectrum in the low frequency range for the healthy and sun fault cases at 30% speed . 149
Figure 8-9 Spectrum in the low frequency range for the healthy and planet fault cases at 30% speed 150
Figure 8-10 Spectrum in the high frequency range for the healthy and sun fault cases 151
Figure 8-11 Spectrum in the high frequency range for the healthy and planet fault cases 152
Figure 8-12 Amplitude of acceleration signal at the sun gear fault frequency vs. load (a) Fixed accelerometer and (b) MEMS 153

Figure 8-13 Amplitude of acceleration signal at $3f_{pm}+frs$ frequency vs. load (a) Fixed accelerometer and (b) MEMS.....153
Figure 8-14 Amplitude of acceleration signal at $3f_{pm}-f_{rs}$ frequency vs. load (a) Fixed accelerometer and (b) MEMS 154
Figure 8-15 Amplitude of acceleration signal at $3f_{pm}-f_{sf}$ frequency vs. load (a) Fixed accelerometer and (b) MEMS 154
Figure 8-16 Amplitude of acceleration signal at the sun gear fault frequency vs. load 155
Figure 8-17 Amplitude of acceleration signal at the 2nd harmonics of sun gear fault frequency vs. load 155
Figure 8-18 Average amplitude for sun fault under different loads.....156
Figure 8-19 Amplitude of acceleration signal at the planet gear fault frequency vs. load.....156
Figure 8-20 Amplitude of acceleration signal at the 2nd harmonic of the planet gear fault frequency vs. load.....156
Figure 8-21 Aveage amplitude for planet fault under different loads.....157

List of Tables

Table 1-1 Comparison of maintenance strategies 24
Table 1-2 Definition of common statistical parameters 28
Table 2-1 Valve actuations per time with variable compressor speed 49
Table 3-1 Features for wireless standards. 72
Table 3-2 Absolute error of harmonics for one MEMS sensor method 87
Table 3-3 Parameter ranges for the Monte-Carlo simulation. 87
Table 3-4 Error results of the Monte-Carlo test for one MEMS sensor method 88
Table 4-1 Specifications of the motor and the Broom Wade TS9 reciprocating compressor. 92
Table 4-2 AX3 features 97
Table 4-3 specification of the ADXL345 98
Table 4-4 CED 1401 Plus channel 100
Table 4-5 Test cases description 103

List of Abbreviations

ALC	Autocorrelation Local Cepstrum
ASW	Asymmetric Stator Winding
BDC	Bottom Dead Centre
BL	Baseline Signal
BLE	Bluetooth-Low-Energy
CBM	Condition-Based Maintenance
CEPE	Centre of Efficiency and Performance Engineering
DAQ	Data Acquisition System
DSSS	Direct Sequence Spread Spectrum
DVL	Discharge Valve Leakage
EMD	Empirical Mode Decomposition
ER	Energy Ratio
ETSI	European Telecommunications Standards Institute
FRMS	Root Mean Square Of The Filtered Signal
GA	Genetic Algorithm
GUI	Graphical User Interface
HT	Hilbert Transform
IAS	Instantaneous Angular Speed
IL	Intercooler Leakage
ISM	Industrial, Scientific and Medical
LAN	Local Area Network
LCC	Life Cycle Costs
LED	Light Emitting Diode
MAC	Medium Access Controller
MAN	Metropolitan Area Network
MCU	Microcontroller
MEMS	Micro Electro Mechanical Systems
MSB-SE	Modulation Signal Bispectrum Based Sideband Estimator

NCEL	Neale Consulting Engineers Ltd
NSDS	Normalized Summation Difference Spectrum
OFDM	Orthogonal Frequency Division Multiplexing
PAN	Personal Area Network
RAN	Regional Area Network
RVM	Relevance Vector Machine
S/N	Signal To Noise Ratio
SI	Sideband Index
SIG	Bluetooth Special Interest Group
SLF	Sideband Level Factor
SPWVD	Pseudo-Wigner-Ville-Distribution
TDC	Top Dead Centre
UI	User Interface
WAN	Wide Area Network
WPT	Wavelet Packet Transform

Abstract

The most common sensors that are used to monitor the condition of a machine health are wired accelerometers. The big advantages of using these types of accelerometers are their high performance and good stability. However, they have certain drawbacks as well. These accelerometers are large in size and require a cable for external power source. Hence a more reliable and cheaper alternatives of these conventional accelerometers are needed that can eliminate the drawbacks of the wired accelerometers. This thesis reports the application of wireless Micro-Electro-Mechanical System (MEMS) accelerometer for machinery condition monitoring. These sensors are so small that they can be easily mounted on the rotating machine parts and can acquire dynamic information very accurately.

One critical problem in using an on-rotor accelerometer is to extract the true tangential acceleration from the MEMS outputs. In this research, the mathematical model of an on-rotor triaxial MEMS accelerometer output signals is studied, and methods to eliminate the gravitational effect projected on X-axis (tangential direction) are proposed. The true tangential acceleration that correlates to the instantaneous angular speed (IAS) is reconstructed by combining two orthogonal outputs from the sensor that also contain gravitational accelerations.

To provide more accurate dynamic characteristics of the rotating machine and hence achieving high-performance monitoring, a tiny MEMS accelerometer (AX3 data logger) has been used to obtain the on-rotor acceleration data for monitoring a two-stage reciprocating compressor (RC) based on the reconstruction of instantaneous angular speed (IAS). The findings from the experiments show that the conditions of the RC can be monitored and different faults can be identified using only one on-rotor MEMS accelerometer installed on compressor' flywheel.

In addition, the data collection method is improved by considering the wireless data transmission technique which enables online condition monitoring of the compressor. Thus, a wireless MEMS accelerometer node is mounted on the RC to measure the on-rotor acceleration signals. The node allows the measured acceleration data to be streamed to a remote host computer via Bluetooth Low Energy (BLE) module. In addition, the device is miniaturised so that can be conveniently mounted on a rotating rotor and can be driven by a battery powered

microcontroller. To benchmark the wireless sensor performance, an incremental optical encoder was installed on the compressor flywheel to acquire the instantaneous angular speed (IAS) signal.

Furthermore, conventional accelerometer mounted on the machine's housing provide lower accuracy in diagnosis the faults for planetary gearboxes because of the planet gears' varying mesh excitation due to its carrier movement. In contrast, installation of the smaller AX3 MEMS accelerometers is done at diametrically opposite direction to the each other of the planetary gearbox's low-speed input shaft, allowing measurement of the acceleration signals which are used for condition monitoring of the gearbox. The findings from the experiments demonstrate that when tangential acceleration is measured at the planetary gearbox's low-speed input shaft, effective fault identification is possible, offering reliability and economy in monitoring the health of planetary gearboxes.

Declaration

This work is put forward towards the requirement of the partial fulfilment for the degree of Doctor of Philosophy at the University of Huddersfield. I hereby declare that neither the present thesis nor any part of it has been elsewhere submitted for the requirement of obtaining any other degree or any other qualification at any other institution or university.

Acknowledgement

This work has been carried out in the Centre for Efficiency and Performance Engineering (CEPE), School of Computing and Engineering at University of Huddersfield, UK. It was financially funded by Libyan higher education through the Libyan cultural affairs in London. I am very grateful for their support during all stages of my PhD study.

I would like to thank my supervisor, **Professor Andrew D. Ball**, for all his guidance and help during my study. I am especially grateful to my co-supervisor **Dr Fengshou Gu**, for his encouragement, excellent guidance and support from the initial to the final level that enabled me to develop an understanding of the subject and to gain a good experience.

Also, many thanks to all members of the CECP group especially **Dr Guojin Feng** who is always willing to help, share ideas and give his best suggestions.

I would also like to thank my friend **Hala Alaneizi** who has supported me throughout my study and heartily thanks to all my relatives and friends back home.

Last and always, special and grateful thanks to my mother, **Noura**, my sisters: **Sarah**, **Saida** and **Hanan** and my brother, **Omar**, who always keep supporting and encouraging me to do my best.

Publications

1- **Mones, Z.,** Zhen, D., Alqatawneh, I. Zeng, Q., Gu, F. & Ball. A.D. (2018, September). Fault Diagnosis of Planetary Gearboxes via Prossesing the On-Rotor MEMS Accelerometer Signals. In *Automation and Computing (ICAC), 2018 24th International Conference*. IEEE.

2- Tang, X., **Mones, Z.,** Wang, W., Gu, F., & Ball, A. D. (2018, September). A Review on Energy Harvesting Supplying Wireless Sensor Nodes for Machine Condition Monitoring. In *Automation and Computing (ICAC), 2018 24th International Conference*. IEEE.

3- Alqatawneh, I., Kuosheng, J., **Mones, Z**., Zeng, Q., Gu, F., & Ball, A. D. (2018, September). Condition Monitoring and Fault Diagnosis Based on Multipoint Optimal Minimum Entropy Deconvolution Adjusted Technique. In *Automation and Computing (ICAC), 2018 24th International Conference.* IEEE.

4- **Mones, Z**., Zeng, Q., Hu, L., Tang, X., Gu, F., & Ball, A. D. (2017, September). Planetary gearbox fault diagnosis using an on-rotor MEMS accelerometer. In *Automation and Computing (ICAC), 2017 23rd International Conference on* (pp. 1-6). IEEE.

5- Zeng, Q., **Mones, Z**., Shao, Y., Gu, F., & Ball, A. D. (2017, September). Planetary gear fault diagnosis based on instantaneous angular speed analysis. In *Automation and Computing (ICAC), 2017 23rd International Conference on* (pp. 1-6). IEEE.

6- **Mones, Z**., Feng, G., Tang, X., Haba, U., Gu, F., & Ball, A. (2017). A comparative study of gravitational acceleration cancellation from on-rotor MEMS accelerometers for condition monitoring. In B. Gibbs (Ed.), *Proceedings of the 24th International Congress on Sound and Vibration, ICSV 2017* International Institute of Acoustics and Vibration, IIAV.

7- Ogbulafor, U. E., Feng, G., **Mones, Z**., Gu, F., & Ball, A. (2017). Application of Wavelet Packet Transform and Envelope Analysis to Non-stationary Vibration Signals For Fault Diagnosis of a Reciprocating Compressor.

8- Haba, U., Shaeboub, A., **Mones, Z**., Gu, F., & Ball, A. (2017, September). Diagnosis of Compound Faults in Reciprocating Compressors Based on Modulation Signal Bispectrum of Current Signals. In *Proceedings of the 2nd International Conference on Maintenance Engineering, IncoME-II 2017,(University of Manchester, 5-6 September 2017)*. University of Manchester.

9- **Mones, Z**., Feng, G., Ogbulaor, U. E., Wang, T., Gu, F., & Ball, A. (2016, October). Performance evaluation of wireless MEMS accelerometer for reciprocating compressor

condition monitoring. In *Power Engineering: Proceedings of the International Conference on Power Transmissions 2016 (ICPT 2016), Chongqing, PR China, 27–30 October 2016* (No. 2016, pp. 893-900). Taylor & Fran-cis.

10- Feng, G., Hu, N., **Mones, Z**., Gu, F., & Ball, A. D. (2016). An investigation of the orthogonal outputs from an on-rotor MEMS accelerometer for reciprocating compressor condition monitoring. *Mechanical Systems and Signal Processing*, *76*, 228-241.

CHAPTER 1 INTRODUCTION

In recent years, modern industrial processes have become more complicated, which means that maintenance tasks have become more important and the need for good, simple and cheap maintenance planning has grown. This research aims to introduce a new wireless condition monitoring method achieving an effective reduction in maintenance cost.

This chapter begins with an overview of maintenance strategies and the most well-known condition monitoring techniques. Then, it presents the wireless condition monitoring system, after which the research aim and study objectives are described. Finally, it explains the thesis structure.

1.1 Maintenance Strategies and Condition Monitoring

The main goal of any investment made by industrial companies is to reduce costs, enhance product quality and achieve maximum profit, which is a challenge faced by many companies. As today's industrial machines are becoming more automated, larger scale, more complicated, integrated and involving hundreds of pieces, the unexpected breakdowns of a single item not only damages the component itself but might also affect the other related components [1]. Due to this, many different faults and failures can occur in the machinery, resulting in performance reduction, significant economic loss, and even worse, catastrophic accidents such as explosions and personal injury.

Every year, industries spend billions of dollars on machine maintenance, allocating around 40% of the total production budget for this [2]. Besides, it is proposed that a large chunk of the net maintenance costs, approximately one-third, is unnecessarily expended due to poor planning, overtime or poor use of preventive maintenance [3]. A significant saving in maintenance costs can be successfully achieved by implementing effective and sufficient maintenance programmes.

Different maintenance strategies have recently been developed to keep machines running in a normal condition and reduce downtime. Breakdown maintenance, preventative maintenance, and predictive maintenance are the most well-known strategies used by industrial companies.

1.1.1 Corrective Maintenance

Breakdown maintenance, also termed by run-to-failure maintenance, is carried out only when the machine completely fails, and there are no predetermined actions required to prevent system failure. It involves repairing or replacing failed equipment so that the machines are made able to perform their required functions after they have failed [4]. Figure 1.1 illustrates the different stages of breakdown maintenance.

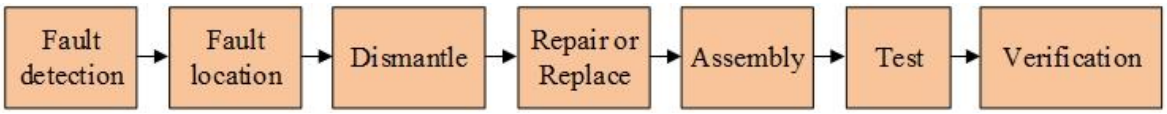

Figure 1-1 Stages of a breakdown maintenance task [5].

This strategy is generally applied when, for example, the cost of a new replacement machine is cheaper than maintenance costs, and all known failures are safe and do not result in critical

damage or cause ruinous accidents. On the other hand, run-to-failure maintenance strategy is the most expensive among maintenance strategies when it is applied to critical equipment.

1.1.2 Periodical Maintenance

Periodical maintenance, which is basically scheduled for predetermined periods, is one of the older methods used to examine machines in industries to detect faults at an earlier time than failure, and is shown in stages in Figure 1.2.

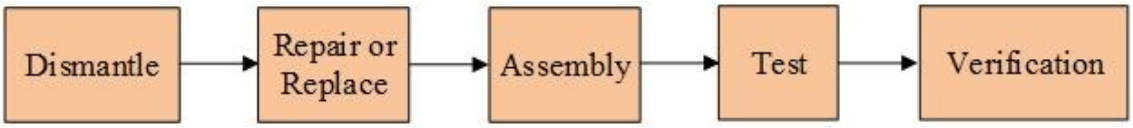

Figure 1-2 Stages of a preventive maintenance task [5].

This approach sets maintenance tasks to be performed at specific time intervals to avoid equipment failure through repairs, maintenance or even replacement of components [6]. Compared with breakdown maintenance, a scheduled maintenance strategy can result in savings in maintenance costs. However, this method is still expensive, in which about 30-40% of preventive maintenance costs are spent on unnecessary actions, and incorrect priorities are chosen and implemented [2]. Besides, in some cases, machines parts are replaced while their condition is still good. Also, unexpected failures may occur before the next scheduled maintenance session, leading to machine downtime.

1.1.3 Predictive Maintenance

This strategy is also indicated as Condition-Based Maintenance (CBM). It monitors the machine's condition and performance to detect any changes in the system, and this can provide useful information about the machine's state. The information measured is compared with the normal machine parameters, and then a decision on whether maintenance is required can be taken. The predictive maintenance strategy is a powerful approach in which detecting abnormal conditions and faults early can give time to plan maintenance schedules and prevent system failure. However, a successful CBM strategy needs experts to analyze the data obtained from the additional investment in instrumentation, and also to suggest maintenance tasks. The benefits of CBM are the potential to avoid unexpected failures, minimize downtime, reduce cost by avoiding unnecessary machinery maintenance and improve reliability and safety.

Various predictive maintenance techniques, including noise level monitoring, instantaneous angular speed (IAS) analysis, vibration monitoring, temperature measurements and ultrasonic analysis, can be applied to detect any change, and thereby, machine condition can be indicated and its performance can be predicted. Table 1.1 summarizes a comparison of the maintenance strategies explained above.

Table 1-1 Comparison of maintenance strategies

Strategy	**Summary**	**Cost to implement**	**Advantages**	**Disadvantages**
Breakdown maintenance	Fix when it breaks	Low	Ideal for unimportant equipment	Can cause a huge repair cost (production loss)
Periodical maintenance	Maintenance at predetermined intervals	Average	• No expertise required. • Reduces accident rates	• Not easy to determine the ideal maintenance interval. • Interrupts production
Predictive maintenance	Machinery condition- based maintenance	High	Can be cost effective by reducing the unnecessary schedule of preventive maintenance.	• Expensive as extra instrumentation is needed • Needs experts to analyze data

1.2 Condition based Monitoring Techniques

Condition based monitoring programmes rely on data gathered from monitoring machine condition to inform maintenance activities. This approach seeks to eliminate unneeded maintenance, with activities only implemented where abnormal readings which may indicate a fault are found. Effective organization and implementation of CBM can minimise maintenance costs, with fewer unneeded maintenance work being undertaken.

Figure 1.3 shows a typical CBM procedure, including three essential steps, which are [7]:

1- Data collection: acquiring parameters including vibration, noise level, temperature, motor current and pressure, etc.

2- Data processing: information collected in step one is analyzed to provide an accurate description of the machine's condition.
3- Fault diagnosis and decision making: recommending effective maintenance policies.

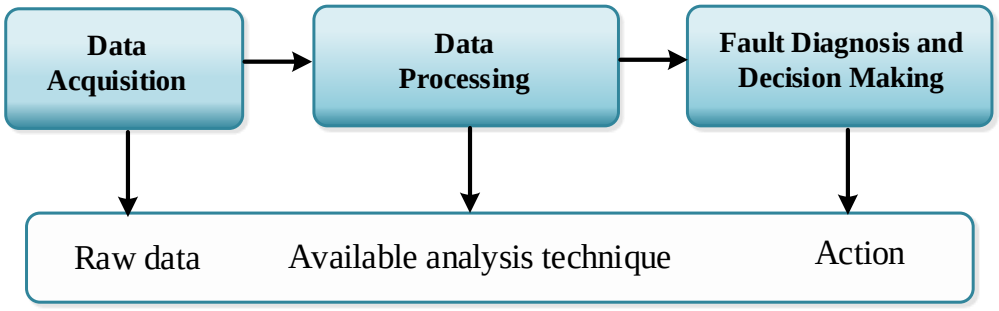

Figure 1-3 Condition based maintenance main steps [7]

Different parameters can be used by the machine as languages to inform the investigator about its condition, and different techniques are used to enhance the accuracy, reliability and applicability of condition monitoring systems. This brings an important question: which physical parameters are to be monitored to obtain an accurate and quick description of the machine's condition, allowing the correct maintenance to be carried out? Noise level, current and voltage signals, vibration, acoustic emission, and many other parameters can be used individually, or they may be combined to offer better diagnosis [8].

1.2.1 Visual Inspection

Visual inspection based condition monitoring is a conventional method based on basic human senses such as smell, sight and hearing. It offers a simple, easy and cost effective method to detect problems such as leakages, loose mountings, cracks, corrosion and structural cracks [9]. Although the cost of this method is low compared with modern techniques for condition monitoring and it does not require any extra instrumentation to be installed on the equipment, a high skilled person based on long experience is required to obtain a good diagnosis [7]. Besides, different findings may be concluded for the same machine by different examiners as they have different personal skills and experiences.

1.2.2 Trend Monitoring

In this monitoring technique, a parameter, such as pressure, speed, temperature, torque, electrical current and power consumption, is repeatedly measured to identify any change in

machine characteristics. The recorded data is typically plotted on a graph against time and compared with another group of measurements measured to represent the acceptable or normal machine operation. Differences between these two data sets are used to identify any machine abnormality and assessed to detect any fault.

Generally, the typical machine's statistical life as shown in Figure 1.4, can be divided into three parts: start up, useful life and wear out [10].

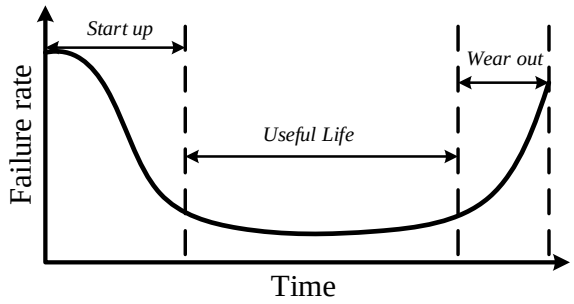

Figure 1-4 Typical bathtub curve [10]

In the first stage, which takes place during the first few weeks of machine operation, the failure rate is relatively high because of installation issues, design errors and manufacturing defects. The failure probability rate decreases rapidly when these problems are discovered and corrected. After the start-up phase, the machine progresses into a steady period named the useful life period, during which the rate of failure is relatively low. The last period is the wear out stage, in which probability of failure rises as the machine gradually becomes nearer to the end of its operating life [10]. Therefore, it is clear that measuring and plotting data on graphs can assist the tracking of developments through trend monitoring.

1.2.3 Performance and Behaviour Monitoring

Any machine is designed to perform specific functions. As shown in Figure 1.5, the main aim of performance and behaviour monitoring is to determine whether the machine is performing the required functions: for instance, converting energy from one form to another [11].

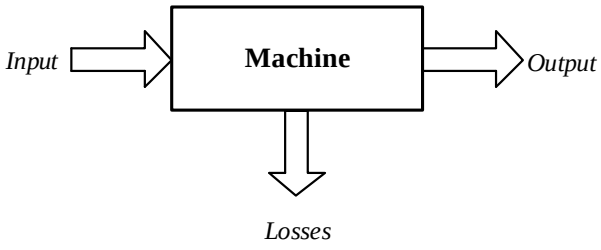

Figure 1-5 Machinery performance

In general, the performance of machines such as compressors, gas turbines and heat engines deteriorates over time and their efficiency decreases, power consumption increases and the operating cost rises. Physical changes in machine components is the main reason that causes deterioration in system performance. A good indication of machine condition can be obtained from information collected by performance monitoring using highly accurate transducers that detect change in load, pressure, flow, power etc. [11], [12].

1.2.4 Instantaneous Angular Speed Monitoring

The instantaneous angular speed (IAS) of rotating and reciprocating machinery contains significant information about machine conditions. More attention has recently been given to IAS based condition monitoring for rotating machines such as diesel engines, electric motors and gears, utilising IAS [13]. A typical and precise way of measuring IAS is installing an optical encoder on one end of the rotor. Traditional encoders have been used for a long time in industry to monitor machines' performance and for fault detection. However, these sensors are usually expensive, are not suitable for isolated environments and their installation is difficult [14].

In this study, an optical encoder has been used to measure the IAS of a reciprocating compressor and used to confirm the results obtained from a wireless MEMS sensor.

1.2.5 Vibration Monitoring

Rotary and reciprocating machines naturally generate a vibration that can provide valuable information about running machinery conditions. Vibration based method is a well-known technique applied in industrial environments to monitor the condition of machines. Many faults across a wide range of rotating machines such as gearboxes, shafts, reciprocating compressors, motors, and engines can be detected by vibration analysis methods. According to Devendiran, vibration measurement is able to identify around 90% of all machine faults by examining the change in vibration signals produced by the machine, allowing a precise prediction for the future failure to be given[15].

Conventionally, an accelerometer is fixed on the machine to obtain vibration waveforms. Because of the complexity of machine constructions, the mounting position of the accelerometer often influence the signal quality and hence diagnostic accuracy significantly. Particularly, problems with it can arise from different influential issues such as vibration and noise from other sources, the presence of complicated non-linear and non-stationary process

and the influence of transmission paths[16]. Different signal processing methods have been developed to process vibration signals in order to reduce the influence of these problems, which can be reviewed according to three general groups: time-domain, frequency domain and time-frequency domain.

1.2.5.1 Time-domain Analysis

Time domain analysis of vibration signals is one of the simplest techniques applied for fault detection. This can be done simply by visual observation of vibration signals or may involve work to process the data for extracting various waveform feature parameters or statistical measures. Commonly used such measures are Peak Value (PV), Skewness (Sk), Kurtosis, Crest Factor (CF) and Root Mean Square (RMS) [17]. Table 1-2 provides the definitions of the common statistical parameters used for machinery condition monitoring.

Table 1-2 Definition of common statistical parameters [18]

Method	Formula	Characterisation of Waveforms
Root Mean Square (RMS)	$RMS = \sqrt{\frac{1}{N}\sum_{i=1}^{N} x_i^2}$	Measures the energy evolution of the input signal
Peak to peak value (P2P)	$P2P = \frac{\max(x_i) - \min(x_i)}{2}$	Measure the maximum difference within the input signal
Skewness (Sk)	$SK = \frac{\frac{1}{N}\sum_{i=1}^{N}\left(x_i - \tilde{x}\right)^3}{\left[\sqrt{\frac{1}{N}\sum_{i=1}^{N}\left(x_i - \tilde{x}\right)^2}\right]^3}$	Measures the asymmetry of the input signal about its mean value.
Kurtosis (KT)	$SK = \frac{N\sum_{i=1}^{N}\left(x_i - \tilde{x}\right)^4}{\left[\sum_{i=1}^{N}\left(x_i - \tilde{x}\right)^2\right]^2}$	Measures the peakedness, smoothness and the heaviness of tail in the input signal.
Crest factor (CF)	$SK = \frac{P2P}{RMS}$	Measures the ratio between P2P and RMS.

Using waveforms allows the detection of changes in vibration signatures which occur due to a fault, but it is challenging to diagnose the source of a fault using these time domain analysis methods.

1.2.5.2 Frequency domain Analysis

The frequency domain denotes to the display the vibration data based on the frequency and it is conventionally applied as an effective analysis method for identifying and diagnosing a fault developing in rotating machines [19]. It analyses spectral information of vibration signal by transforming the signal to the frequency domain.

Researches show that there are frequently greater benefits from spectral components of signals as compared with measured time-domain to assess the condition of machines, due to the high complexity of time-domain signals and the benefits of dividing these into a number of components in the frequency domain allowing the frequencies which are most useful in diagnosing faults to be analysed [19]. This makes frequency domain analysis an essential way for rotating machine fault detection and diagnosis.

Spectrum analysis is the most frequently used technique for rotating machines condition monitoring and fault detection. The main idea of spectral analysis is to look at the whole spectrum or only certain frequencies of interest and therefore extract features from the signal [20], [21]. The spectral information $X(m)$ of a discrete time series data $X(n)$ is typically calculated using a discrete Fourier transform (DFT):

$$X(m) = \sum_{n=0}^{N-1} x(n)\, e^{-j2\pi nm/N} \tag{1-1}$$

The common used tool in spectrum analysis is the power spectrum, which can be defined by:

$$P = E\left[X(m) * X^{*}(m) \right] \tag{1-2}$$

Where $X^{*}(m)$ denotes the complex conjugate of $X(m)$ and E represents expectation.

Due to the poor efficiency of DFT, Fast Fourier Transform (FFT) is the common technique used in condition monitoring to transform vibration signals into frequency domain. The technique gives reasonable results where there is no time varying in the recorded signal, meaning that the machinery's speed of rotation does not vary. However, FFT-based techniques are not suitable for non-stationary signals.

1.2.5.3 Time- Frequency domain Analysis

Either the time or the frequency domain method generates monitoring features that relate to the specific domain but not to the other. It means that there is no spectral information provided by the time-domain analysis, and when transforming time-domain signals into a frequency-domain, details of the time-domain are not kept. Therefore, the two approaches are limited. Moreover, use of FFT is restricted to stationary signal. For non-stationary signals, FFT is applied to determine the presence of various spectral elements, but does not identify the time-points where components are present. Where data on time is needed, FFT cannot be used. Time-frequency analysis allows data to be obtained about the way in which the spectral components in signals change over time, meaning that temporary events including impacts can be identified [22]. Recently, techniques for representing time-frequency have been developed, including Short-Time Fourier Transform (STFT) [23] and Wavelet Transform (WT) [24]. A summary of how joint time frequency analysis is applied in diagnosing machine faults is given in [25].

- Short-Time Fourier Transform

Short-Time Fourier Transform (STFT) is one of the most powerful techniques used to analysis non-stationary signals. It can provide information about the signal in frequency over time. STFT can be implemented by applying FFT to a short part of signal separated by a window function moving along the time direction. The STFT for a discrete signal $x(n)$ over a time window $w(m)$ can be calculated by:

$$X\left(m,k\right)=\sum_{n=-\infty}^{\infty}x\left[n\right]w\left[n-m\right]e^{-j2\pi kn/N} \tag{1-3}$$

Although STFT is a powerful technique introduced to overcome the limitations of the FFT in analysing non-stationary signals. However, it has well known disadvantages regarding time-frequency resolution mainly due to using a fixed window function size [26].

- Wavelet Transform

The Wavelet Transform technique can be applied as an alternative method to the STFT. It has been quickly developed and its effective application can be found in many fields including mechanical fault detection and diagnosis [27], [28]. A continuous wavelet transform can be defined as[29]:

$$W(a,b)=\frac{1}{\sqrt{a}}\int_{-\infty}^{\infty}x(t)\,\psi^{*}\left(\frac{t-a}{a}\right)dt \tag{1-4}$$

Where $x(t)$ is the original waveform signal, a is the scale parameter b is the time parameter and ψ^{*} indicates a wavelet.

1.3 Wireless Condition Monitoring

Currently, the extensive and successful application of wired online condition monitoring techniques can be found in many industrial fields. However, the high cost of these systems has restricted their application for a wide range of critical industrial machines [30]. With the development of wireless transmission techniques, communications technologies, and electronics, it is becoming feasible and popular to use wireless sensors for machinery condition monitoring, to avoid wired online condition monitoring problems. As the cables used in wired condition monitoring can cost from £40 to £80 per foot, with a cost of up to £2000 per foot in dangerous, non-reachable and harsh environments [31], so the main benefit obtained by bringing in wireless technologies for condition monitoring is in reducing the cost. Besides, wireless sensors can be easily installed on machinery located in isolated environments, as well as allowing easier replacement and upgrading than wired condition monitoring. Moreover, the use of wireless sensors can provide a way to monitor the rotor part of a machine by mounting the sensor directly on-rotor, as explained in this research.

WSN technology has recently begun to be applied in numerous commercial areas, including for example; environmental monitoring [32], construction health observation [33] and temperature monitoring in product distribution [34]. Nevertheless, the environment of industry and its applications cause further difficulties in the usage of wireless sensors for machine condition monitoring and fault detection, for example processing mixed sensor signals, provide higher sampling rates, required faster data transfer rates, and offer higher reliability [30]. Figure 1.6 shows a simplified roadmap for wireless technology implementation in an industrial environment.

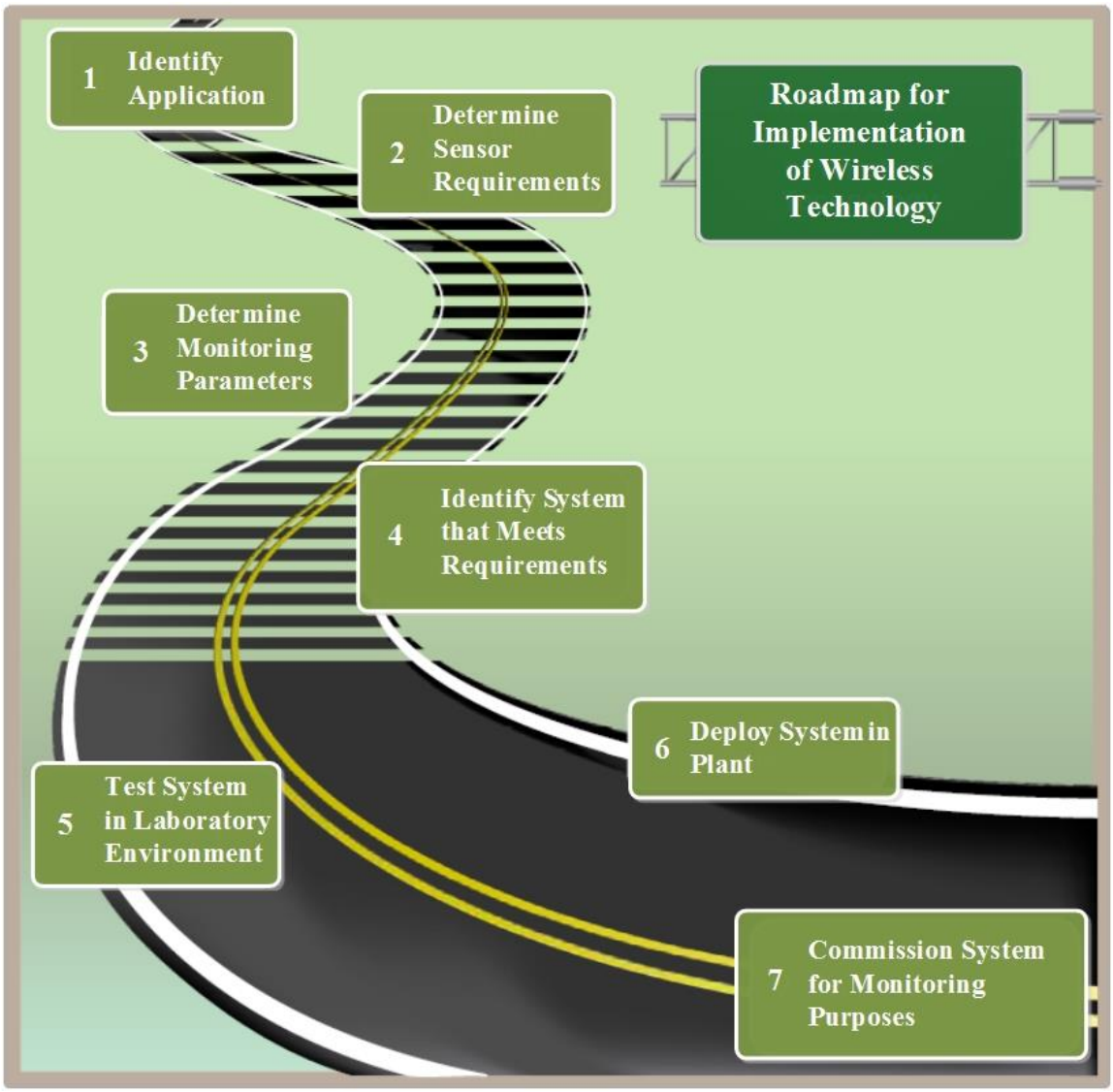

Figure 1-6 Wireless Technology Implementation in Industries [35]

1.4 Research Motivation

Rotating machines such as motors, gearboxes, bearings, pumps and compressors are widely used in many mechanical systems and are an important area of machine condition monitoring research. To monitor such machines, many methods have been applied in order to detect defects early, before downtime occurs. Rotating machine condition monitoring is usually achieved using conventional wired sensors. By analyzing the rotating part vibration using an accelerometer installed in the stationary part of the rotating machine, as well as the

instantaneous angular speed (IAS), measured, for example, using a shaft encoder installed at the end of the rotor, many faults can be detected.

Developments in MEMS technology and wireless techniques can help to improve the condition monitoring method for rotating machines by measuring on-rotor accelerations at low cost. As MEMS accelerometers measure gravitational acceleration as well as acceleration caused by motion, so obtaining the true tangential acceleration that is characterized the rotor dynamics precisely is the most challenging issues in wireless MEMS based sensors for rotary condition monitoring. This research focuses on the usage of MEMS accelerometer and wireless transmission techniques to develop a new method used for rotating machinery condition monitoring in which the wireless MEMS sensor is attached directly to the rotor to record acceleration information.

The motivation for this research is to develop a cheap, accurate and reliable system for fault detection and diagnosis of rotating machine based on the on-rotor acceleration acquired by a wireless MEMS sensor.

1.5 Research Aim and Objectives

This research aims to use advanced wireless transmission techniques and MEMS technologies for condition monitoring applications by directly installing the MEMS accelerometer on the rotating part of the machine. To achieve this target, the project will be carried out through the following steps:

Objective one: Review the popular condition monitoring techniques used in industry and choice an effective method to monitor the health status of both reciprocating compressor and planetary gearbox.

Objective two: Review MEMS technology and the availability of accelerometers made based on this technology that can be used for on-rotor measurements.

Objective three: Investigate different wireless protocols that can be used in wireless condition monitoring and study the advantages and disadvantages of each protocol and how to select a suitable protocol for various applications.

Objective four: Perform mathematical analysis and modelling of orthogonal outputs from wireless on-rotor MEMS accelerometer. Introduce a novel way to remove the gravitational

acceleration that is projected on both measurement axes so that the dynamics information regarding the rotor can be obtained.

Objective five: Benchmark the performance of usage of the reconstructed signals for rotating machines condition monitoring.

Objective six: Achieve a remote condition monitoring for a reciprocating compressor by using wireless MEMS accelerometer.

Objective seven: Measure the IAS of the reciprocating compressor using an optical encoder and compare the results with that obtained from on-rotor MEMS accelerometer.

Objective eight: Compares between two methods used to eliminate the gravitational acceleration projection effect.

Objective nine: Introduces a novel method for planetary gearboxes condition monitoring in which a tiny on-rotor MEMS accelerometers have been installed on the input shaft to measure the acceleration signals.

Objective ten: Evaluate the performance of usage on-rotor measurement for planetary gearbox condition monitoring by comparing it with the vibration measurement obtained by a conventional fixed accelerometer.

1.6 Thesis Layout

The thesis is organized into nine chapters to describe the work that was done to achieve the main aim of this research.

Chapter 2 provides general information about the rotating and reciprocating machines and focuses on the reciprocating compressors and planetary gearbox as they are used in the experimental work.

In **Chapter 3**, an overview of wireless communication techniques and MEMS technology is presented. Besides, it studies a method used to eliminate gravitational acceleration from the MEMS output signals to obtain the tangential acceleration that may be employed in condition monitoring and fault diagnosis.

Then, the test rig used to carry out the investigation is introduced in **Chapter 4**.

Data acquired by a MEMS accelerometer (AX3 data logger) installed on the compressor flywheel to classify faulty signals is presented in **Chapter 5**.

The work achieved in Chapter 5 is improved upon, in which the measured information is sent remotely to a host computer using Bluetooth Low Energy (BLE) protocol. **Chapter 6** analyzes data collected wirelessly and compares the results with those obtained from the shaft encoder used to measure the IAS of the compressor flywheel.

Chapter 7 presents another method that might be employed to get rid of acceleration due to gravity using two MEMS accelerometers and compares the results with the results presented in Chapter 5.

Chapter 8 studies the usage of an on-rotor MEMS accelerometer in planetary gearbox condition monitoring and fault diagnosis to confirm that the on-rotor accelerometer is an effective method and can be used for different machines to detect faults early.

Finally, **Chapter 9** presents the conclusions, summarizes the achievements of the project and gives suggestions for possible future work.

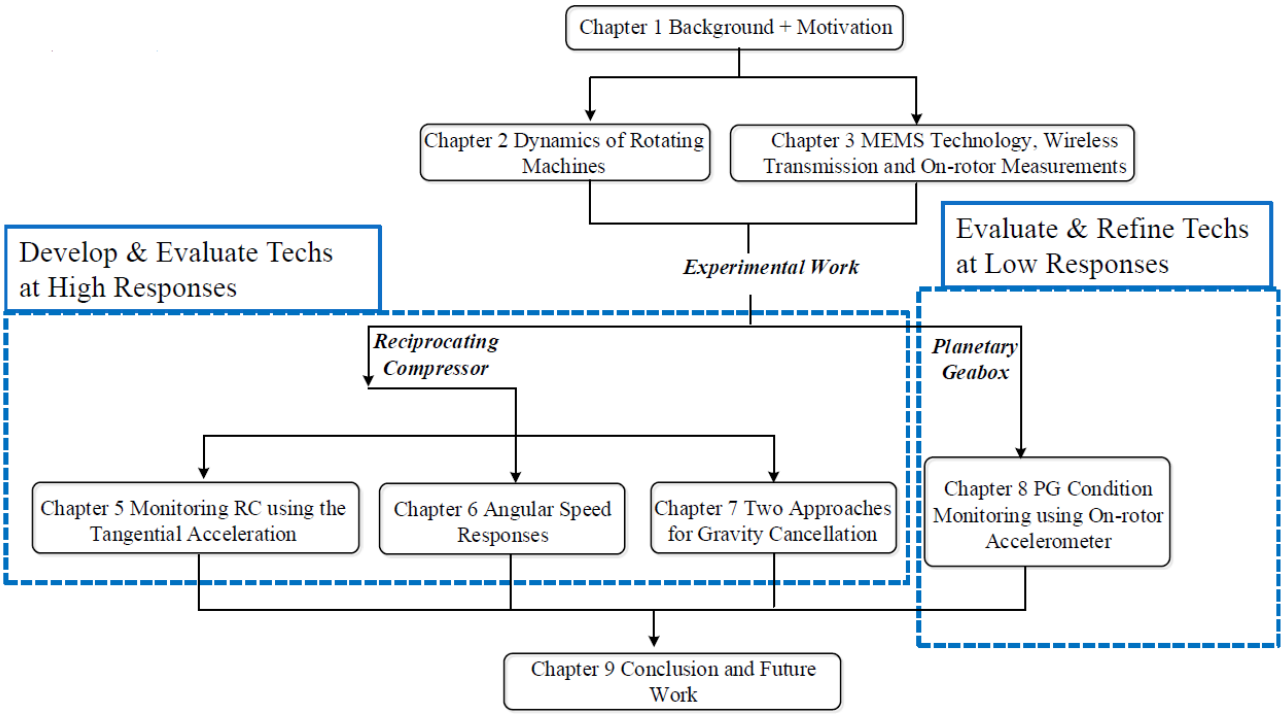

Figure 1-7 Thesis Structure

CHAPTER 2 DYNAMICS OF ROTATING MACHINES

This chapter provides information about the reciprocating compressor and planetary gearbox. It is divided into two parts in which the first one covers reciprocating compressor and the second part deals with the planetary gearbox. The first part begins with an introduction on reciprocating compressors and their working principles followed by dynamic modeling of both single-stage and two-stage reciprocating compressors, and it will end with a discussion of reciprocating compressor valve failures and condition monitoring. The second part introduces the gears and their failure. It then gives general information about planetary gearboxes and their characteristic frequencies of fault. Next, different condition monitoring techniques adopted for planetary gearboxes have been explained.

2.1 Reciprocating Compressors

In general, compressors are machines that change mechanical energy into internal energy in a gas. However, part of the work done by the compressor is also converted into non-usable forms such as heat losses [36].

There are various types of compressor, with specific configurations being tailored to the applications needed, but generally, compressors may either be intermittent or continuous in their mode of operation. Intermittent compressors use a cyclical technique in which they first take in a set volume of gas, exert compressive force on this gas and then expel it, after which the cycle begins again with new gas. By contrast, continuous compressors take in, exert force on and then expel a continual flow of gas. There are two main types of intermittent or positive displacement compressor; rotary and reciprocating compressors [37]. The main types of compressor are illustrated in Figure 2.1.

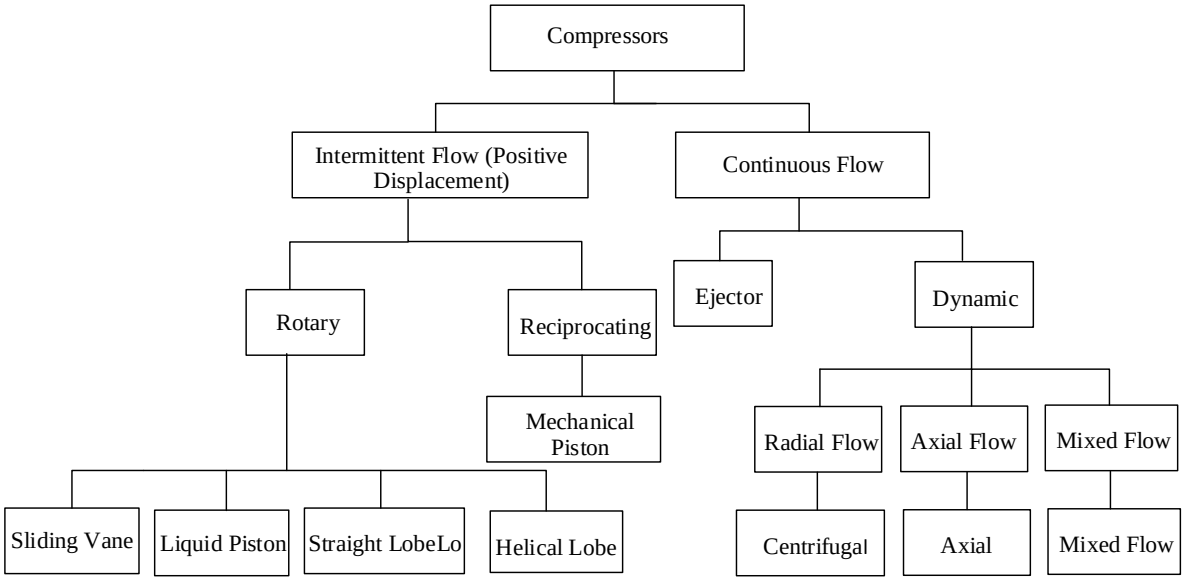

Figure 2-1 Compressor Types [37]

This work focuses on reciprocating compressors, which fall under the positive displacement type and are one of the most widely-employed compressors in industry [38]. These are used to compress air or any other gas from a low pressure, which is commonly the atmospheric pressure, to a higher desired pressure level [36]. The inlet air pressure is increased by reducing its volume and the work required to increase air pressure obtained from the prime mover driving the compressor. An electric motor and turbine are normally used as prime movers [39].

The main components of a reciprocating compressor are a piston, a connecting rod, a shaft, a crankshaft and a flywheel. Besides these, one of the most important parts of a reciprocating compressors is the valve, of which there are two types of valves; a suction and a discharge valve.

Generally, such machines play an essential part in industry: for example, they are the major component in factories' air and gas transmission, gas pipelines, oil refineries, and natural gas handling plants. Like any machinery in industry, reciprocating compressor reliability should stay as high as possible and this can be achieved through condition monitoring techniques to detect any fault at an earlier stage.

2.1.1 How the Reciprocating Compressor Works

There are a wide range of reciprocating compressors, which may have a single cylinder and one stage cycle for compressing air, or may comprise multiple -cylinders and service processes as gas compressors. However, no matter their size or the service they provide, all reciprocating compressors are based on identical operating principles and follow similar fundamental designs.

According to [36], the operational steps of the reciprocating compressor, based on a reciprocal piston action within the cylinder can be described as follows: firstly, the position of the piston is at the top point, indicated as the Top Dead Centre (TDC), and both the inlet and delivery valves are closed. After that, the piston starts the movement in the downward direction. When the air pressure within the cylinder goes below the atmospheric pressure, the inlet valve will start opening and this allows the air to come into the cylindrical region. As pressure difference starts to decrease, the inlet valve steadily closes and will be completely closed when the air pressure inside the cylinder is equal to the atmospheric pressure. At this point, the piston will be at the Bottom Dead Centre (BDC) and both the inlet and delivery valve remain closed. Next, the piston will start moving up, increasing the pressure inside the cylinder space. When a pressure differential arises between the receiver and the space inside the cylinder, the delivery valve then begins to open, allowing the compressed air to move into the receiver. The upward movement of the piston brings it nearer to the top of the cylinder, the air pressure decreases, leading the delivery valve to begin to shut. At this point, the initial cycle is complete, and the next one follows in the same way [36].

2.1.2 Reciprocating Compressor Operation and Maintenance Costs

From the available literature on energy use in industry, air compression systems utilize 10% of consumption, and compressed air represents a comparatively costly resource for industrial plants. When viewing life cycle costs (LCC) overall, the resources initially invested and costs of maintenance are just a fraction of the actual spend on compressed air systems, with energy use generally accounting for at least 75% of costs annually. Energy consumption is therefore often the largest expense in the lifecycle of these systems, and may be over 5 times greater than the cost of acquiring and installing the system (see Figure 2-2) [40].

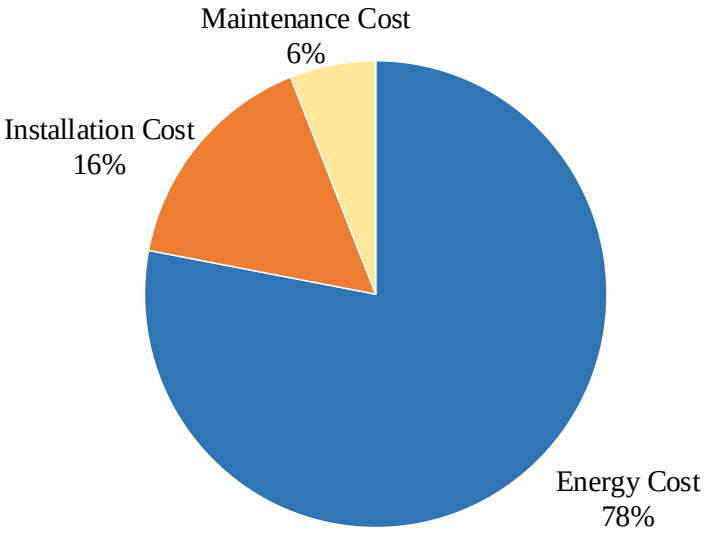

Figure 2-2 Life cycle costs of compressed-air energy use

The two major variables affecting costs associated with compressed air are the compressor control approach and selecting an appropriately-sized compressor. Compressor systems which are too large or which are not controlled efficiently consume larger amounts of energy and cost more to operate annually [40], [41].

As mentioned above, the maintenance cost for a reciprocating compressor is the smallest value among the other costs, however, unanticipated downtime in reciprocating compressors frequently leads to a significant

reduction in plant output in which the compressor domntime cost per only one hour might be up to $20,625 [42] . Therefore, detecting and diagnosing faults before systems failure is essential to preventing production losses. This is typically achieved through continuous condition monitoring techniques.

2.2 Single Stage Reciprocating Compressors

Simple single stage reciprocating compressors comprise a moving piston which performs a constraint reciprocating motion within the cylindrical confinement. This piston has a mechanical connection with the crankshaft via a connecting rod. Thus, as the crankshaft rotates about its axis drives the connecting rod which, in turn, results in the up-down motion of the piston that remains constraint within the cylindrical chamber. This chamber contains the valve pockets through which the suction and discharge of gases takes place across the respective valves. Figure 2-3 (a) presents a single acting compressor and (b) shows the schematic representation of the described single acting compressor.

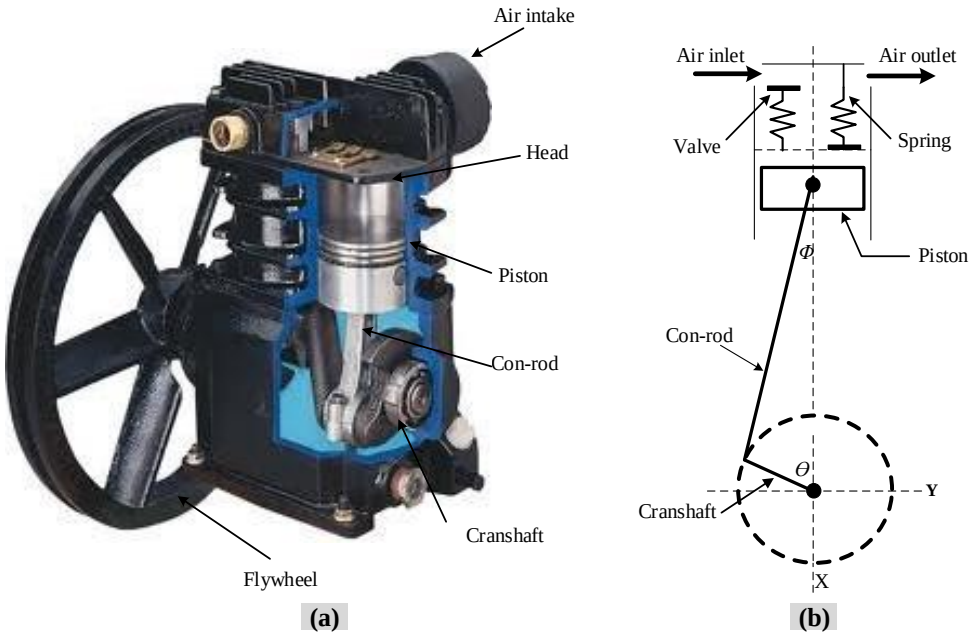

Figure 2-3 (a) Single acting compressor and (b) Schematic diagram of single acting compressor

According to [43], and as shown in Figure 2-4, the single stage reciprocating compressor cycle has four basic events, summarized as follows:

1- Intake: in this phase, the suction valve is open and then the air cylinder is filled with air.

2- Compression: at this stage both valves are closed and the piston starts moving up towards the valves, reducing the air volume and increasing its pressure.

3- Discharge: the discharge valve opens during this phase, allowing the air to move out of the cylinder and enter high pressure storage.

4- Expansion: Both valves are closed in this part of the cycle. The piston moves down and away from the valves, causing the air volume to increase, which means that the pressure inside the cylinder reduces.

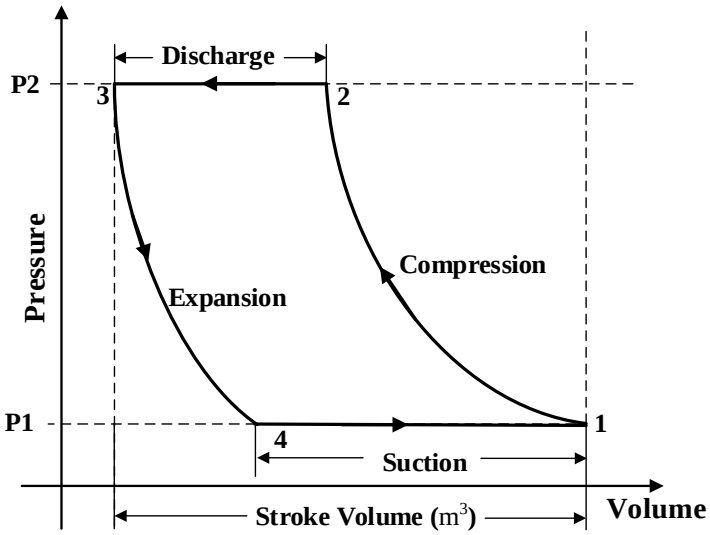

Figure 2-4 An ideal Pressure-Volume diagram [44]

2.2.1 Dynamics of the Piston Mechanism

Figures 2-5 (a) and (b) show the piston-cylinder scheme used typically in reciprocating compressors. It is assumed that the piston is connected to a crank having a radius of *r* through a connecting rod of length *l* and is driven by a reciprocating motion from their actions. When the crankshaft rotates, it will cause the connecting rod to move the piston in the cylinder, compressing the air by applying a force *F* directed against the motion of the piston. From Figure 2-5 (a), it can be seen that the reaction to the force *F* can be resolved into two components: the magnitude of the first one is $F/\cos\varphi$, acting along the connecting rod, and the second one is of magnitude $F/\tan\varphi$, acting in the Y direction. The force $F/\cos\varphi$ produces a torque M_t to rotate the crankshaft in a clockwise direction about Z.

$$M_t = \left(\frac{F}{cos\varphi}\right) r sin\left(\theta + \varphi\right) \tag{2-1}$$

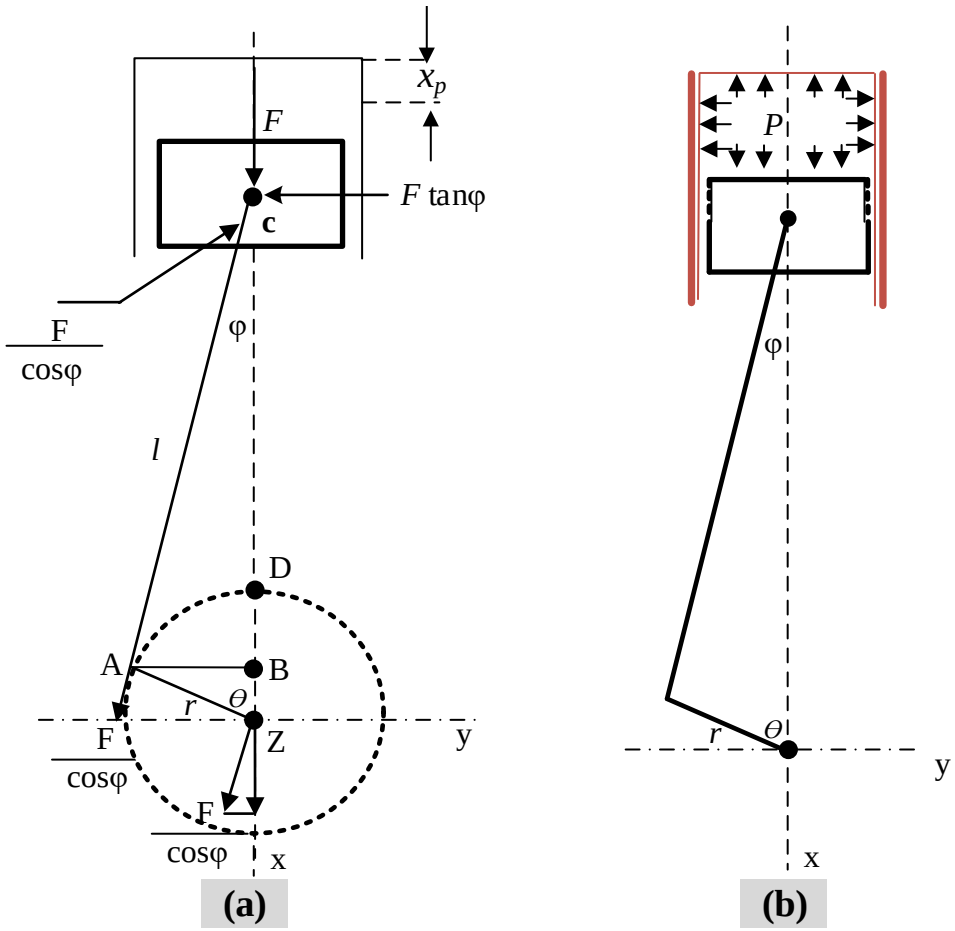

Figure 2-5 (a) Action of the gas pressure forces. (b) Forces due to gas pressure.

Besides, assuming that the crankshaft is rotating at steady angular speed of ω, the displacement of the piston can be calculated as a function of the crank angle θ.

$$x_p = r\left(1-\cos\left(\theta\right)\right)+l\left(1-\cos\left(\varphi\right)\right) \tag{2-2}$$

By considering the geometry of the crankshaft and connecting rod

$$l\sin\left(\varphi\right) = r\sin\left(\theta\right) \tag{2-3}$$

And,

$$l^2 = l^2\cos^2\left(\varphi\right)+r^2\sin^2\left(\theta\right) \tag{2-4}$$

As a result,

$$\cos^2\left(\varphi\right) = \frac{l^2 - r^2\sin^2\left(\theta\right)}{l^2} \tag{2-5}$$

Therefore,

$$cos(\varphi) = \sqrt{1 - \frac{r^2}{l^2} sin^2(\theta)} \tag{2-6}$$

By substituting $cos(\varphi)$ from equation 2-6 into equation 2-2, x_p can be expressed as [45]:

$$x_p = r(1 - cos(\theta)) + l\left(1 - \sqrt{1 - \frac{r^2}{l^2} sin^2(\theta)}\right) \tag{2-7}$$

The velocity of the piston can be obtained by differentiation equation 2-7 and is expressed as [45]:

$$\dot{x}_p = \omega r\, sin\theta\left(1 - \frac{r}{l} cos\theta\right) \Big/ \left(\sqrt{1 - \frac{r^2}{l^2} sin^2\theta}\right) \tag{2-8}$$

According to [46], the relation between the crank radius *r* and connecting rod of length *l* is usually equal to 1:4 making the term $r^2 / l^2 sin^2$ much smaller than 1, and it can be neglected. Considering this assumption, equation 2-8 can be recast as [45]:

$$\dot{x}_p = \omega r\, sin\theta\left(1 - \frac{r}{l} cos\theta\right) \tag{2-9}$$

Equation 2-10 expresses the acceleration of the piston, which is simply calculated by differentiating the velocity given in equation 2-9 [45].

$$\ddot{x}_p = \omega^2 r\left(cos\theta - \frac{r}{l} cos2\theta\right) \tag{2-10}$$

2.3 Multistage Reciprocating Compressor

Multistage compressors play an important role in air and gas compression and distribution applications. Figure 2-6 shows a multistage industrial reciprocating compressor offered by Corken Company and used for liquid gas transfer. The use of multistage compressors is essential to producing high pressures of more than about 300kPa, and according to general gas laws, as the pressure increases, the temperature will also increase. This additional heat can be removed using an intercooler, which is very important for this type of compressor and is considered to be a significant factor in making the multistage compressor more expensive than the single one [36].

Also, to reach higher pressures the power needed to drive the compressor rises. However, the use of multistage compressors reduces the input power requirements and increase system efficiency.

Figure 2-6 Multistage reciprocating compressors for liquid gas transfer (Source: Corken Company)

2.3.1 Two Stage Reciprocating Compressor

Figure 2-7 displays the block diagram and the air flow through a two–stage reciprocation compressor. Meanwhile, the ideal overall working cycle of a two stage reciprocating compressor, including two sequences; each one with four typical phases of intake, compression, discharge, and expansion, is presented in Figure 2-8.

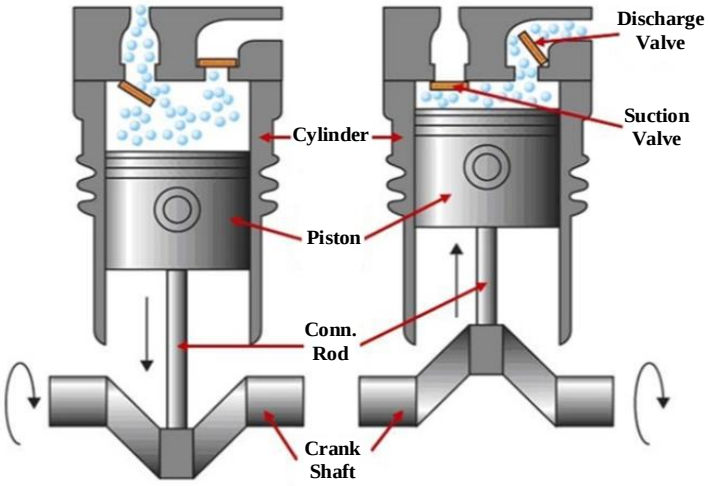

Figure 2-7 Schematic of a two-stage compressor [47]

For the first cycle, the inlet valve is open from 1 to 2, whereas the delivery valve is open from 3 to 4. Similarly, the inlet valve is open from 5 to 6 and the delivery valve is open from 7 to 8 in the second cycle.

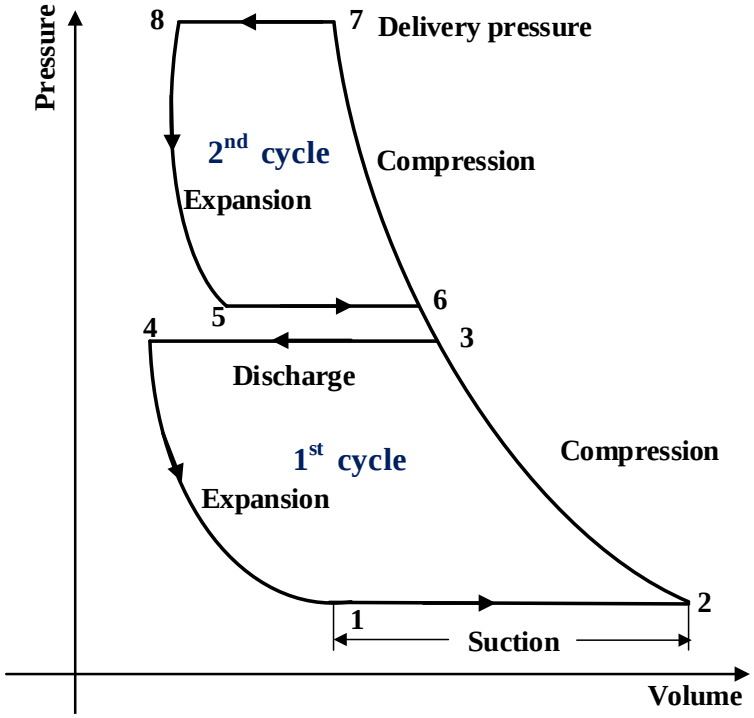

Figure 2-8 An ideal P-V diagram for a two-stage compressor

As explained in Section 2-3, the intercooler is an essential component in multistage reciprocating compressors which is used to reduce the compressed gas temperature, as shown in Figure 2.10.

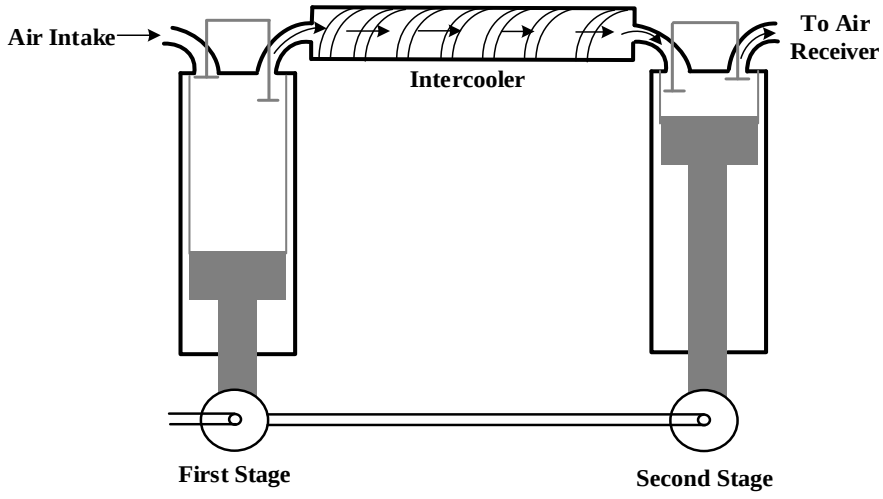

Figure 2-9 Illustration of intercooler on a two-stage reciprocating air compressor [48]

Use of an intercooler between reciprocating compressor stages is necessary and brings many benefits including:

- Cooling the gas allows more of it to be compressed into the same space.
- Saving power; as the temperature increases, the gas will expand, which means more power is required to compress the gas. Rise in the inlet air temperature by 4 ^{0}C results in a higher consumption of energy by 1% to achieve the same output. Therefore, using the intercooler concept makes the temperature lower and therefore improves the energy efficiency of a compressor [49].

In most reciprocating compressors, the intercooler consists of a pipeline that carries the gas from the first stage to the second stage and is connected to the stages using joints, which should be serviced to avoid any leakages. A leak in the joints of the intercooler can arise because the joints are starting to loosen due to the effects of vibration. The joints should be served at a scheduled time and monitoring of their condition is necessary, as a very small leak will reduce the compressor's efficiency and a large intercooler leakage might lead to system failure.

2.3.1.1 Two-stage Piston and Crank Arrangement

Figure 2-10 shows a simplified dynamic model of a two-stage reciprocating compressor. As displays in this figure, the piston position for each cylinder is assumed to be positive when it moves downward.

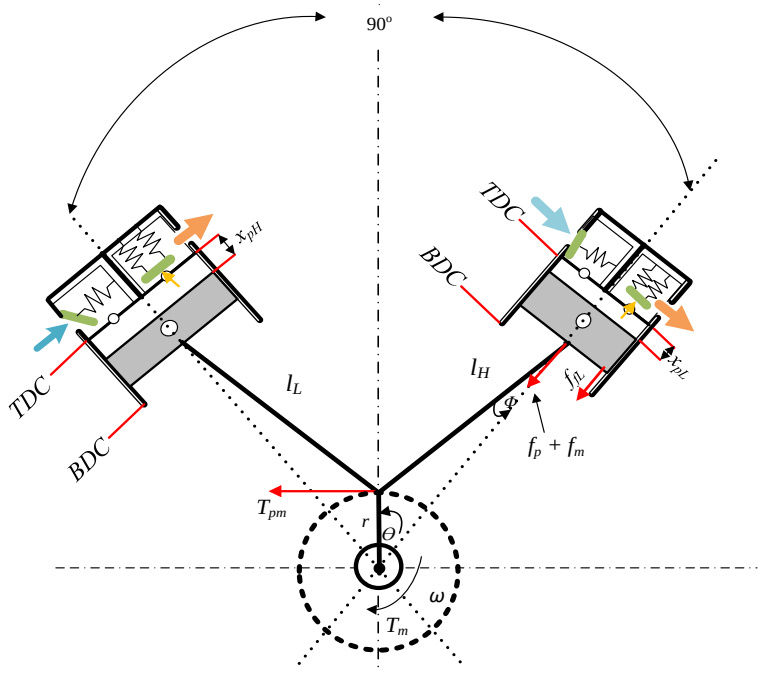

Figure 2-10 Two-stage reciprocating compressor simplified model

The maximum volume above the cylinder can be obtained when the piston resides at the lowest position within the cylinder, i.e. at the BDC: whereas the minimum volume above the cylinder will occur when the piston resides at the highest position within the cylinder, i.e. at the TDC.

For the compressor that has been used in this research, the displacement of the piston in the second stage leads to a displacement of the first stage by 90°. If the first stage is taken as the reference stage, the displacements of both the first and second stages can be written as [45]:

$$x_{pL} = r\left(1-cos\left(\theta\right)\right)+l\left(1-\sqrt{1-\frac{r^2}{l^2}sin^2\left(\theta\right)}\right) \tag{2-11}$$

$$x_{pH} = r\left(1-cos\left(\theta+\frac{\pi}{2}\right)\right)+l\left(1-\sqrt{1-\frac{r^2}{l^2}sin^2\left(\theta+\frac{\pi}{2}\right)}\right) \tag{2-12}$$

where the subscripts L and H demote low and high stages, respectively.

The velocity, $\dot{x}_{pL}$ & $\dot{x}_{pH}$, and acceleration, $\ddot{x}_{pL}$ & $\ddot{x}_{pH}$, of the pistons for the low pressure and high pressure cylinders can be obtained by differentiation as given in the following equations [45]:

$$\dot{x}_{pL} = \omega r\, sin\theta\left(1-\frac{r}{l}cos\theta\right)\Bigg/\left(\sqrt{1-\frac{r^2}{l^2}sin^2\theta}\right) \tag{2-13}$$

$$\dot{x}_{pH} = \omega r \sin\left(\theta+\frac{\pi}{2}\right)\left(1-\frac{r}{l}\cos\left(\theta+\frac{\pi}{2}\right)\right)\Bigg/\left(\sqrt{1-\frac{r^2}{l^2}sin^2\left(\theta+\frac{\pi}{2}\right)}\right) \tag{2-14}$$

$$\ddot{x}_{pL} = \omega^2\ r\left(cos\theta-\frac{r}{l}cos2\theta\right) \tag{2-15}$$

$$\ddot{x}_{pH} = \omega^2 r\left(\cos\left(\theta+\frac{\pi}{2}\right)-\frac{r}{l}cos2\left(\theta+\frac{\pi}{2}\right)\right) \tag{2-16}$$

2.3.1.2 Equation for Cylinder Volume

Generally, the volume of any cylinder is defined by:

$$V = \pi r^2 h \tag{2-17}$$

where r and h are radius and is the height, respectively.

For the reciprocating compressor, we consider the cylinder head, cylinder wall and the piston end-face as the control volume boundaries. The instantaneous cylinder volumes for the first and second stages can be written as presented in equations 2-18 and 2-19.

$$V(t) = V_c + \pi r^2 x_{pL} \tag{2-18}$$

$$V(t) = V_c + \pi r^2 x_{pH} \tag{2-19}$$

Where V_c is clearance volume, in m^3, x_{pL} is displacements of the first stages and x_{pH} is displacements of the second stages. By substituting x_{pL} & x_{pH} from equations 2-11 and 2-12 into equations 2-18 and 2-19, $V(t)$ for both stages can be written as:

$$V_{pL}(t) = V_{cL} + \pi r^2 \left\{ r\left(1 - cos(\theta)\right) + l\left(1 - \sqrt{1 - \frac{r^2}{l^2} sin^2(\theta)}\right)\right\} \tag{2-20}$$

$$V_{pH}(t) = V_{cH} + \pi r^2 \left\{ r\left(1 - cos\left(\theta + \frac{\pi}{2}\right)\right) + l\left(1 - \sqrt{1 - \frac{r^2}{l^2} sin^2\left(\theta + \frac{\pi}{2}\right)}\right)\right\} \tag{2-21}$$

2.4 Reciprocating Compressors Valve Failures and its Practical Condition Monitoring

The major problems in reciprocating compressors are caused by valve failures, which are stated as the main reason for unscheduled reciprocating compressor shutdowns. The majority of unscheduled reciprocating compressor downtime and maintenance costs can be attributed to the compressor valves, which is reported as a reason for around 36 % of unscheduled shut downs and about 50% of total repair costs [50]. Reciprocating compressor valves fail for different reasons, but grossly they follow two main categories, which are environmental and mechanical causes [38].

Different elements in the valves' environment can lead to valve failure. For example, foreign materials such as dirty air, carbonaceous deposits, liquids that come over the intercooler between stages and corrosive elements may form the reason for valve failure: particularly in the intake valve, in which the air or gas comes from outside and is of poor quality. This kind of failure can typically be prevented by choosing the proper valve material and processing the gas using a filter before the intake phase. The second category, mechanical causes, can be

defined as valve failures that occur due to different reasons including fatigue resulting from high repeated cyclic stress, as shown in Table 2-1, which illustrates the number of times each valve operates in eight hours, in a day and in a month at different compressor speeds [36]. Also, abnormal mechanical action of the valves can be caused by spring failure, valve fluttering, pulsations and wrong valve operation conditions. Mechanical causes related to operation factors and incorrect application can be controlled or eliminated by proper communication between a qualified and experienced user and the manufacturer [51].

Table 2-1 Valve actuations per time with variable compressor speed

	Compressor speed, rpm		
Time	300	600	1000
8 hours	144,000	288,000	480,000
1 day	432,000	864,000	1,440,000
1 month	12,960,000	25,920,000	43,200,000

To achieve high reliability for these critical reciprocating compressors, carrying out continuous condition monitoring of the system and performing analysis of the collected data is required, resulting in an improvement in both the time and cost needed for maintenance. Many researchers have investigated different methods using different physical parameters to check the circumstances of a reciprocating compressor to improve fault detection and diagnosis.

Liang et al. introduced a procedure using frequency and vibration time domain, and smoothed pseudo-Wigner-Ville-distribution (SPWVD) to detect and diagnose valve faults, including leaking, accumulation of deposits and deterioration of valve springs. [52]. Besides, common reciprocating compressor faults such as discharge valve leakage and intercooler leakage have been classified in [53], in which the vibration signals acquired using an accelerometer mounted on the pressure cylinder were decomposed based on two techniques: Wavelet Packet Transform (WPT) and Empirical Mode Decomposition (EMD). Also, Ahmed et al. presented a procedure for reciprocating compressor diagnosis. They used a relevance vector machine (RVM) with genetic algorithm (GA)-based attribute selection from the vibration signals' envelope spectrum. Their findings show that the classification method is accurate and can be

used to classify different faults [54]. Furthermore, Elhaj et al. compared and evaluated different condition monitoring techniques for reciprocating compressors, including dynamic cylinder pressure and crankshaft Instantaneous Angular Speed (IAS) [55]. In addition, Gu and Ball studied diagnosis of faults occurring in different machines involving reciprocating compressors. Some of their research on reciprocating compressors fault detection with condition monitoring can be found in [45], [56], [57], [58], and [59].

This research introduces a novel method for reciprocating compressor condition monitoring and fault detection in which on-rotor MEMS accelerometers are installed directly on the flywheel to measure acceleration signals, which are used to indicate the compressor's condition.

2.5 Gears Overview

Gears have generally been used in most mechanical devices to transmit power and obtain different speed ratio between shafts by means of successively engaging teeth [60]. Gears are available in a range of capacities, sizes, speed ratios and made from different materials. They have a wide range of industrial applications. However, gears are mainly used to transmit the speed from an input to a different output speed based on gear's specifications [61]. According to the shape of the tooth, gears are classified into many types, and the spur and helical gears have the most important use in an industry.

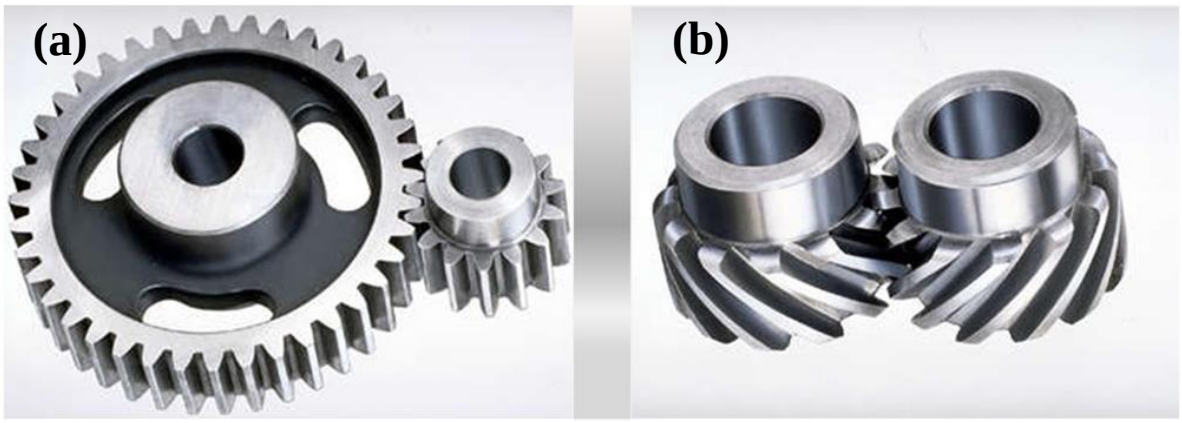

Figure 2-11 Gears types: (a) Spur gear and (b) Helical gear [62]

As shown in Figure 2-11 (a), the spur gears have the straight teeth mounted and run on the parallel direction with the shafts that drive the gears. Generally, when two gears are in

meshing, the gear with fewer teeth is indicated as the pinion, whereas with larger teeth is called gear [63]. Increase or decrease in rotational speeds will depend on the arrangement of the pinion and gears. It gets reduced when the pinion drives the gear, and vice versa. The spur gears have many advantages such as they are simple and easy to design, also spur gears usually have constant speed ratio and they are quite reliable having no issue of axial thrust. All these benefits of spur gears have made them extensively used in many applications; however, they produce loud noise particularly at high speeds which might become unacceptable [64]. Teeth of helical gears, shown in Figure 2-11 (b) are cut at an angle to the face of the gear making helical gears operated much more smoothly and quietly comparing with spur gears. Also, this arrangement leads to the less noise and vibration produced during meshing [63].

2.5.1 Gears Failure

As gears typically work under high stress and tough conditions, different failures can be occurred. As shown in Figure 2-12, these failures are classified into two main groups: local faults including tooth breakage, cracked tooth, chipping local wear [65], and distributed faults including wearing, pitting, scuffing [66], [67].The main difference between the local and the distributed faults is the long time period between the initiation of gear's failure and the loss of serviceability. In the first type, the fault develops quickly once it is started and it has most significant effects on the transmission of power, while faults development is quite slow in the second type, which indicates that the time period between the faults starting and the completion of system failure is usually long.

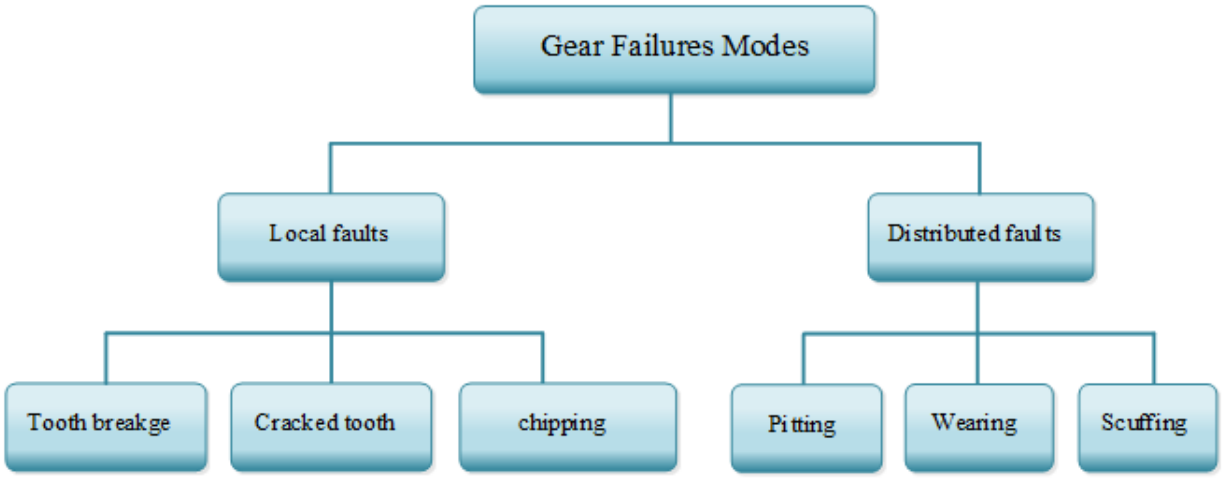

Figure 2-12 Modes of gear failure [67]

Tooth breakage is the ultimate and the most common type of gear failure as it might destroy the gear and it often damages other components like shafts or bearings. Tooth breakage is generally occurred due to many reasons, however the excessive load is the most common cause of tooth breakage [68]. This failure usually starts with a small crack and is developed rapidly causing a part or the whole entire tooth break off.

2.5.2 Gearbox Failure Cause

As stated in [69], [70] and [71], different reasons that can lead to the gear failure can be summarized as:

- The actual loading applied over the gear tooth exceeds the nominal loading for a long term of operations.
- Distribution of the load over the gear tooth is not uniform.
- Gear manufacturing errors and incorrect design.
- Improper lubrication.
- Bearings failure.
- Gear misalignment which affects the accuracy of the meshing and it is exhibited as an early pitting at one end of the tooth.

Gears are generally robust and reliable devices. However, as explained above, the faults occur due to many reasons. A survey of gearbox failures done by Neale Consulting Engineers Ltd (NCEL) has claimed that failures often start with the bearing, rather than the gear itself and as shown in Figure 2-13. About half of the gear failures are found as a result of bearing failures [72].

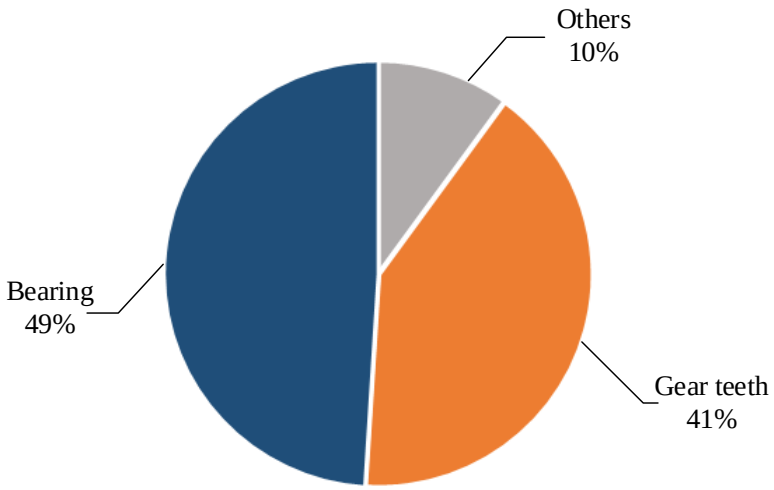

Figure 2-13 Gearbox failures causes [72]

NCEL have studied the causes of gearbox failures in more details, and according to their finding, the reasons of the gear failures in industrial area can be divided into nine categories presented in Figure 2-14.

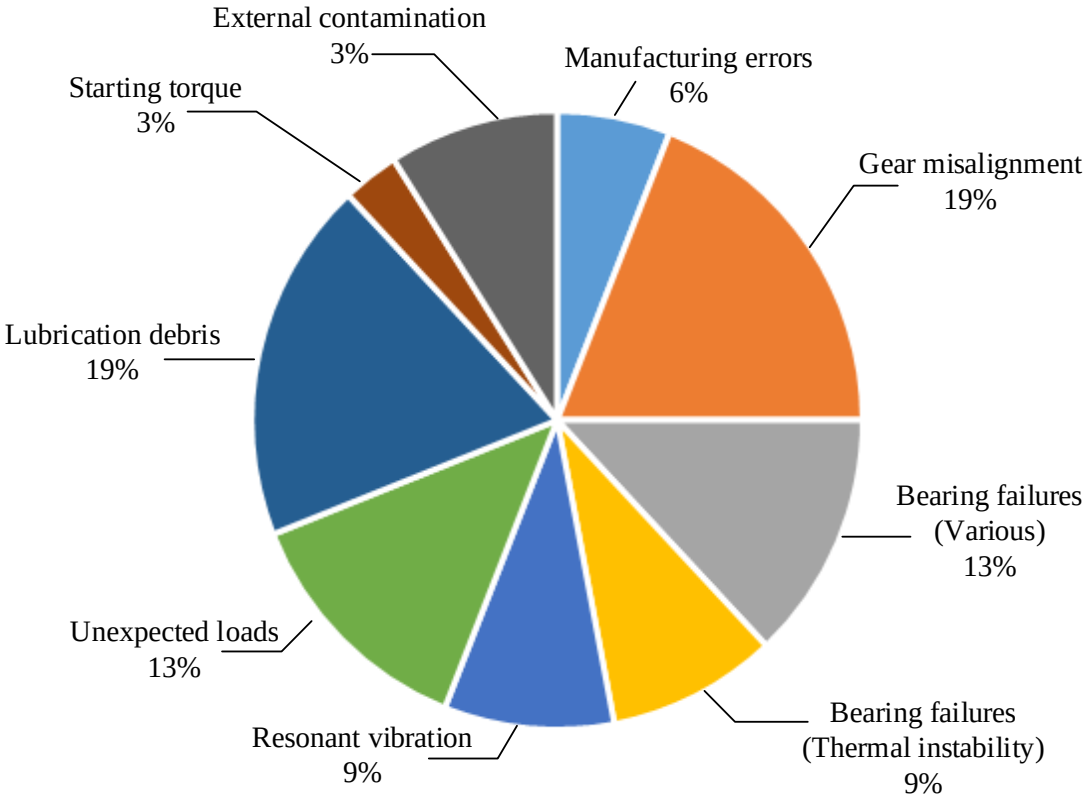

Figure 2-14 Detailed analysis of gearbox failures [72]

Some gearbox failures do occur for multiple causes and it is not easy to determine, for instance, it cannot be concluded that 19% of all gear failures in industries are caused by gear misalignment; which was only a partial reason in some cases examined in this analysis.

2.6 Planetary Gearbox

Planetary gearboxes, which is also known as epicyclic gearboxes, are commonly used in drivetrains of helicopters, heavy industrial applications and wind turbines owing to their heavy load bearing capacity, high transmission ratio and the improved transmission efficiency [73, 74]. As shown in Figure 2-15, the most common type of planetary gearbox is constructed basically with four components: the sun gear, one or more planets gears, a ring gear and a carrier. The planet gears remain adhered to a planet carrier that rotates about the centre around which sun gear also rotates but with a dissimilar speed. Besides, planet gear not only revolves about its own unfixed centres but also rotates about the sun gear centre.

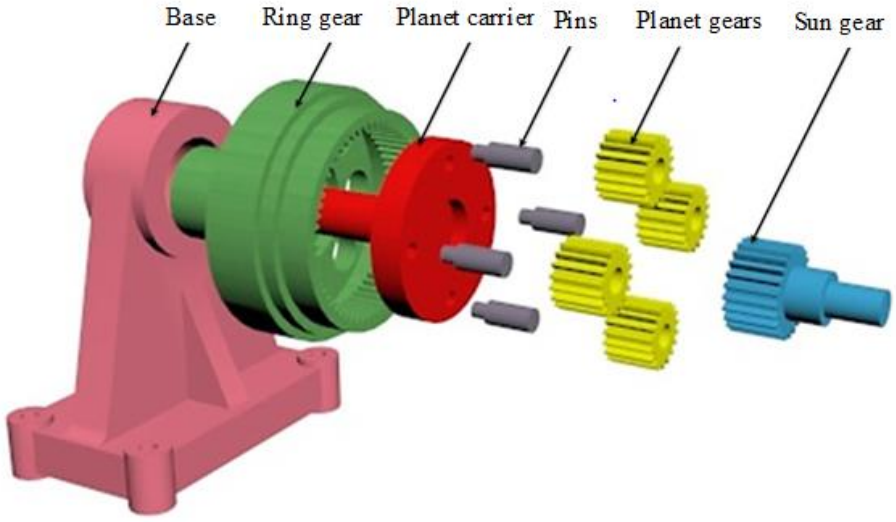

Figure 2-15 Planetary Gear Train [75].

Planetary gearbox can offer different speeds ratios, turning direction and provide high torque amount with the same construction, depending on planetary gear configuration, i.e. which component is the input gear, which is the output one; and which one remains motionless [75]. This makes planetary gearboxes an ideal option to be used in wind turbines, automatic vehicle transmissions and helicopters and [76],[77], [78]. Below are the some examples of planetary gearbox applications based on the speed transmission ratio [79].

- A large reduction low speed can be obtained by using the sun gear as a driver (input), the carrier as a driven (output) and the ring gear is stationary. Thus, a low reverse speed will be obtained.
- When the carrier used as a driver, the ring gear as the driven and the sun gear is stationary an overdrive is obtained.

Figure 2-16 shows the planetary gearbox type that has been studied in this chapter where the sun gear rotates about its own centre and three planet gears rotate about their own unfixed centres as well as about the centre of the sun gear. The planet gears are located between the sun gears and the stationary ring gear. They are also attached to the carrier that perform the input shaft and mesh simultaneously with the planet gears.

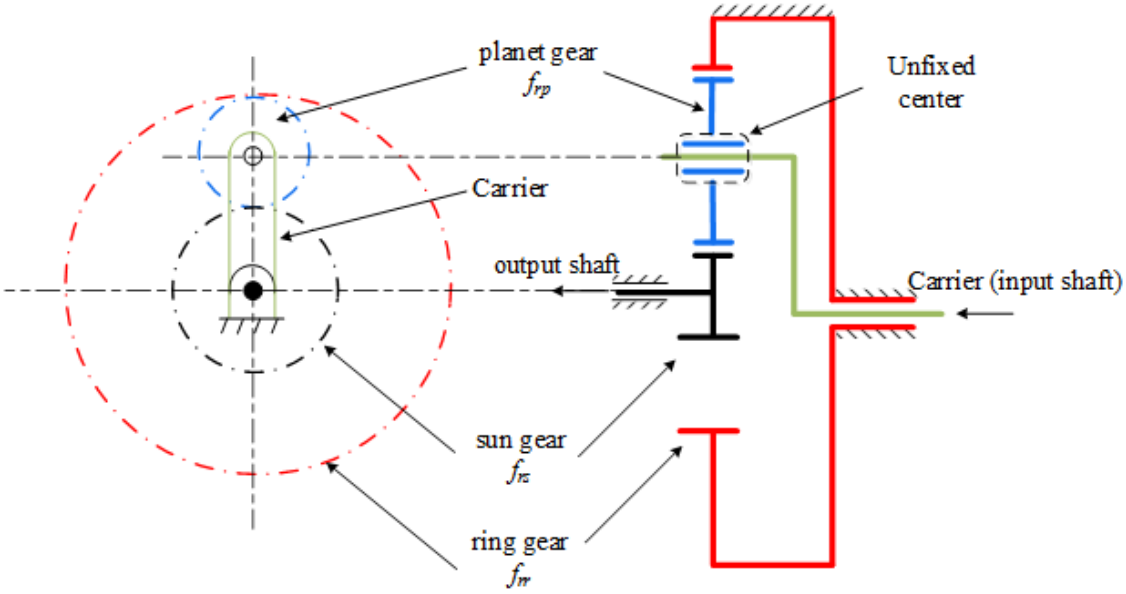

Figure 2-16 Planetary gear configuration under study

From planetary gears configuration and their transmission structure, it has been found that they generally have the following behaviours that make them different from fixed-axis gearboxes [80].

- According to the planet gears transmission structure, the vibration transmission paths are time-varying multiple paths traversing from gear meshing points to the sensors, fixed on planetary gearbox housing [81].

- As the speed transmission ratio is quite large, one component at least rotates under low speed i.e., in low frequency range which has the possibility of heavy noise contamination in the acquired signal. Therefore, it will be quite complicated to detect the fault characteristics of the planetary gear components rotating at low speed [80].
- The vibration signals from the epicyclic gear are excited by the simultaneous meshing of the multiple planet gears with the ring gear and the sun gear [80, 81].

As a consequence, the vibration signal sensed by a fixed accelerometer at the planetary gearbox housings more complicated than that measured from the fixed-axis gearboxes. Therefore, the effective faults detection methods used for fixed-axis gearboxes may have less efficiency when applied to the planetary gears. Although of the complexity of its' working principle, it has several advantages over conventional fixed-axis shaft gear and got particular attention in the industrial area. Planetary gears are very compact construction, light weight, high power intensity, and high torque conversion. Different speed ratios can be obtained depending on the combinations of the driving and driven.

2.6.1 Characteristic Frequencies of Planetary Gearbox

The planetary gearbox considered in this experimental study is provided and manufactured by STM Power Transmission Ltd manufactured and supplied the planetary gearbox used in this experiment, which comprises 3 planet gears, a planet gear carrier connected with the input, a central sun gear assumed to be connected with the output shaft and lastly, a ring gear fixed within the gear housing. For the planetary gearbox used in this work, Z_s=10 is the number of sun gear teeth, Z_p=26 is the number of the three planet gears' teeth, Z_r=62 is the number of ring gear teeth. Therefore, the transmission ratio is defined as [82];

$$i = 1 + \frac{Z_R}{Z_S} \tag{2-22}$$

According to [80] and [83], the rotational frequencies of the sun and planet gears can be calculated using the following equations:

$$f_{rs} = \frac{(z_r + z_s)}{z_s} f_{rc} \tag{2-23}$$

$$f_{rp} = \frac{(z_p + z_r) z_s}{(z_r + z_s) z_p} f_{rs} \tag{2-24}$$

Also, the meshing frequency can be expressed as:

$$f_m = \frac{z_r z_s}{\left(z_r + z_s\right)} f_{rs} = z_r f_{rc} \tag{2-25}$$

2.6.2 Planetary Gearbox Characteristic Frequencies for Fault Diagnosis

Many studies have shown that any type of fault in the planetary gearbox leads to the development of mechanical vibrations, and by examining the changes in characteristic frequency spectrum of the vibration signal around the meshing frequency and its harmonics, these faults can be detected and diagnosed [84]. Assuming that K is the number of planetary gears moving within the carrier, the characteristic vibration frequencies around the meshing frequency are unique for each type of planetary gearbox fault, as identified by [80].

2.6.2.1 Characteristic Frequency of Sun Gear with Local Fault

Assuming that a local fault on the sun gear is present and the system starts rotating, the vibration signal will have two different conditions. When the local fault overlaps with one of the planet gears, the vibration signal will be modulated by an impulse signal, and when the local fault leaves the meshing area, the vibration signal will return to its normal condition [83]. This modulating phenomenon happens $_K$ times in one revolution of the sun gear. In the ideal case of an error-free manufacturing, the characteristic frequency of a sun gear with a local fault , f_{sf} , can be expressed as [84]:

$$f_{sf} = \frac{f_m}{z_s} = K\left(f_{rs} - f_{rc}\right) \tag{2-26}$$

where K is the planet gear number.

2.6.2.2 Characteristic Frequency of Planet Gear with Local Fault

When a local fault transpires on both sides of the planet gear tooth, the vibration signal modulation happens twice during its one period revolution. Then, the characteristic frequency of the planet gear with local fault f_{pf} can be given as [84]:

$$f_{pf} = 2\frac{f_m}{z_p} = 2\left(f_{rp} + f_{rc}\right) \tag{2-27}$$

2.6.2.3 Characteristic Frequency of Ring Gear with Local Fault

Similar to the result of the sun gear with local fault frequencies, the characteristic frequency of a ring gear with local fault f_{rf} can be obtained as [84]:

$$f_{rf} = \frac{f_m}{z_r} = K f_{rc} \tag{2-28}$$

2.6.3 Planetary Gearbox Condition Monitoring

As mentioned earlier, the applications of planetary gearboxes are quite critical and their failure may cause major shutdown of the entire train resulting in large economic losses, therefore the condition monitoring of the planetary gearboxes has received a significant attention to avoid any unexpected interruptions and accidents that might be caused by the failure [80, 84].

As explained in the comprehensive review of the planetary gearbox by Lei et al. [80], Samuel et al. [85], and Yuksel et al. [86], many condition monitoring techniques have been studied for planetary gearbox fault diagnosis to detect different gear faults including tooth breakage, gear pitting and crack. Lei et al proposed two diagnostic parameters based on vibration characteristics of the planetary gearboxes collected using tri-axial accelerometer installed on the planetary gearbox casing. The first method computes the root mean square of the filtered signal (FRMS) and second one calculates the normalized summation of positive amplitudes for difference spectrum between the unknown signal and the baseline (NSDS). Their findings show that these two proposed methods for planetary gearbox condition monitoring and diagnosis perform better than the other existing methods such as energy ratio (ER), sideband index (SI) and sideband level factor (SLF) [87]. Besides, recent work has studied the efficacy of employing the torsional vibration signal as a mean for fault diagnosis of planetary gearbox, and it has been concluded that the planetary gear torsional vibration can pose as an effective and suitable alternative method for condition monitoring of planetary gears [88]. Also, a novel method based on modulation signal bi-spectrum based sideband estimator (MSB-SE) analysis of vibration signals to diagnose the compound faults in the planetary gearboxes has been presented in [89]. Their outcome demonstrate that this method can detect both the bearing faults and the gear faults effectively in the planetary gearbox with severity index under high load conditions. In addition, a study achieved in [90] has investigated IAS based planetary gearbox diagnostics in which gears dynamics are not influenced by the moving mesh gears.

According to this study, the IAS based planetary gearbox condition monitoring system is more cost-effective and easier to be implemented online, compared with the conventional vibration methods over a wide range of operating conditions.

Furthermore, a review study on the methodologies of planetary gearbox condition monitoring and fault diagnosis is presented in [80] and, according to this study, most planetary gearbox diagnostic systems have used the vibration signal measured by an accelerometer mounted on the housing of the planetary gearbox. In the most studies, the vibration was measured using an accelerometer fixed on the gear housing. As shown in Figure 2-17, the position of the planet gear and the carrier at time t is indicated by the angle θ between the planet gear and the accelerometer.

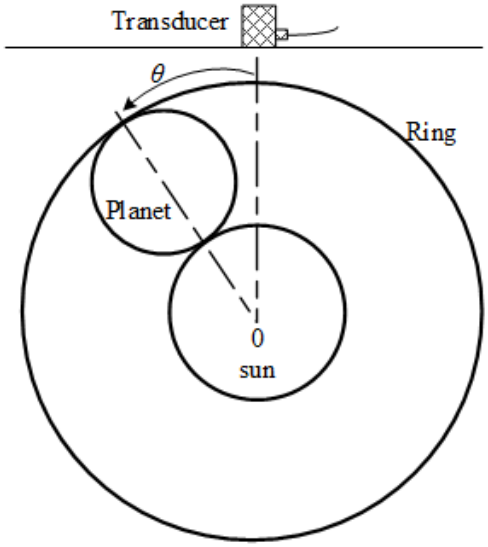

Figure 2-17 Planetary gear system with a single planet [91]

When the carrier rotates the transmission path from the meshing between planets and annulus to the accelerometer always varies. The distance of the path is shortest while the planet comes closest to transducer, at $\theta = 0, 2\pi, 4\pi, \ldots$. The amplitudes of the perceived vibration will be highest at these times. Conversely, the amplitudes of the meshing vibration will be least when the planet gear is at extreme end from the accelerometer, at $\theta = \pi, 3\pi, 5\pi, \ldots$Hence the amplitudes of the vibration will have some intermediate values in between these two positions[91]. The meshing locations for both of the sun gear–planet gear and planet gear–ring gear with respect to the transducers change with time, resulting in amplitude modulation (AM)

on the vibration signal perceived by the sensors. Moreover, it will increases the complexity of the signal [92].

Generally, this vibration signal, *z(t),* contains valuable diagnostic information regarding the planetary gear-set, and can be considered as the superposition of vibrations from planets meshing with the annulus and sun gear [93].

$$z(t) = \sum_{i=1}^{p} \omega_i(t)\left[x_i(t)+y_i(t)\right] \tag{2-29}$$

The window function $\omega_i(t)$ is used to describe the phenomenon of amplitude modulation attributed to the relative motion among the fixed accelerometer and the rotating planets within the carrier [93, 94]. This phenomenon can be explained as follows: as a planet rotates and gets closer to the fixed accelerometer, its vibration dominates the sensory data and the level of its impact attains a peak when the planet is almost under the accelerometer; thereafter, it decreases when the planet moves away from the accelerometer. The signal $x_i(t)$ in the Equation (10-5) denotes the vibration resulting from the ring gear and i^{th} planet mesh, which is periodic at the fundamental gear mesh frequency f_m, whilst the $y_i(t)$ indicates the vibration resulting from the sun gear and i^{th} planet mesh, which is also periodic at the fundamental gear mesh frequency f_m. As a result, the sidebands in the observed vibration signal sensed by a fixed accelerometer have a complex nature, which makes the application of conventional vibration-based diagnostic techniques a challenge for planetary gearbox [93].

Another issue with the measuring of the planetary gearbox vibration signal using fixed accelerometer is the transmission path. The transmission of the vibration signal for the meshing of sun and planet gears follows the path via sun gear, rotating shaft, bearing and the gearbox housing as well as transmitted through the planet gears to annulus and finally to the accelerometer. On the other hand, there is a direct transmission path for the vibration signal produced from the planet-annulus meshing to the sensor. There may exist other transmission paths through planet gear, shaft, bearings, sun gear and the gearbox casing however, if the accelerometer is positioned very close to the annulus then it will have the strong influence of the vibration from the meshing of the planets and annulus and the flow path of vibrational energy will be direct [91].

The above problem can be resolved by mounting an on-shaft accelerometer that will provide a fixed distance from the rotating planets to the sensor.

2.7 Summary

This chapter gave general information about the reciprocating compressor and planetary gearboxes. It introduced their principles, common faults and reviewed different techniques used to monitor their condition.

CHAPTER 3 MEMS TECHNOLOGY, WIRELESS TRANSMISSION AND ON-ROTOR SENSORS

This chapter begins with general information about MEMS accelerometers and presents the basic principle of their operation. Then, it gives an overview of wireless communication technology, followed by a literature review of wireless sensors used for machine condition monitoring. In addition, this chapter studies a method used to remove the effect of the gravitational acceleration from on-rotor MEMS accelerometer outputs. It explains the mathematical model of the orthogonal acceleration signals obtained from an on-rotor MEMS sensor and studies how the gravitational acceleration signal is eliminated. The last section presents the performance of the proposed method.

3.1 Introduction

In recent years, conventional wired condition monitoring has been applied in many industrial machines. Because the system relies on different types of cables for field applications, installation, maintenance and cost become major obstacles to its wider application. Moreover, for rotor condition monitoring and fault diagnosis, it is impossible to deploy a wire sensor directly to the rotating part, so conventional sensors are usually attached to the static parts of rotating machines to monitor their condition and detect any abnormalities. To be able to install sensors directly on the rotor, wireless sensors are essential. Since the main problem associated with wired condition monitoring for rotating systems is as a result of using cables, wireless data transmission is highly desirable and eliminates any requirement for special cables, resulting in installation cost reduction compared with wired condition monitoring [95].

With recent advances in wireless transmission techniques and MEMS technology, it has been feasible and easier to monitor rotating machine conditions by mounting a tiny wireless MEMS sensor directly on the rotor, providing more accurate dynamic characteristics for the rotating machine. As the sensor is directly attached to a rotor, it is able to acquired dynamic characteristics of the rotating part with a high degree of accuracy, making a wireless MEMS sensor a good alternative to expensive conventional sensors [96, 97].

Many studies have employed MEMS accelerometers in the condition monitoring field to investigate their performance. However, few research projects have used MEMS accelerometers to measure the on-rotor acceleration for condition monitoring.

Albarbar et al [98] studied the possibility of using MEMS accelerometers in machine condition monitoring and investigated the performance of three different MEMS accelerometers provided by different manufacturers. From their investigation, it is concluded that MEMS sensors could be used instead of standard sensors, especially for wireless implementation. Arebi et al [99] developed a wireless MEMS accelerometer (WMA) that was attached directly on a rotating shaft and the results demonstrated that different degrees of misalignments can be successfully monitored using MEMS accelerometer. Furthermore, Arebi et al studied and compared response from data collected employing a MEMS accelerometer and shaft encoder under different degrees of shaft misalignment. Findings from their study

showed the WMA have improved performance over the shaft encoder in detecting small shaft misalignment [96].

Baghli et al. developed a new kind of instantaneous torque sensor based on a MEMS accelerometer. They installed two MEMS accelerometers on the coupling of a rotor shaft to acquire the instantaneous torque measurements used for induction motor condition monitoring, and the study proved the effectiveness and accuracy of using on-rotor MEMS accelerometers to measure instantaneous torque [100]. Jiménez et al. introduced a novel topology for enhanced vibration sensing, whereby a MEMS accelerometer was embedded within a hollow rotor allowing the rotational speed to be measured. The speed estimation algorithm presented in that study was tested on a rotor operating at a range of speeds between 200 RPM and 2000 RPM and, by comparing the results obtained using the MEMS accelerometer with the speed measured by the encoder, they confirmed that their method was robust and could be applied to rotors independent of the state of vibration and during both acceleration and deceleration [101].

3.2 MEMS Devices

MEMS technology is a process used to produce tiny devices containing microstructures, microsensors, microactuators and microelectronics integrated into one silicon chip [102]. Each one of these parts has a specific function, and any change in the system's environment is detected by microsensors by measuring thermal, mechanical, chemical, magnetic, or electromagnetic information, which is processed by microelectronics, allowing a decision to be taken by microactuators and some forms of changes to be made. Figure 3-1 shows a schematic illustration of MEMS components.

The microelectronics technology expanded quickly from its first introduction in 1960, and by the following decade had already become well-established [103]. At an earlier stage, developers focused on micromachining essentially related to solid-state pressure transducers. However, at this point, integrating micromechanics and microelectronics was not a major focus, as the technologies needed to micromachine in large quantities and solid-state pressure transducers could not easily be integrated alongside microelectronic technologies. Moving parts using micromechanics were built for the first time in the late 1980s, using surface-micromachining technology [104] with electrostatic micromotors being introduced soon afterwards [105].

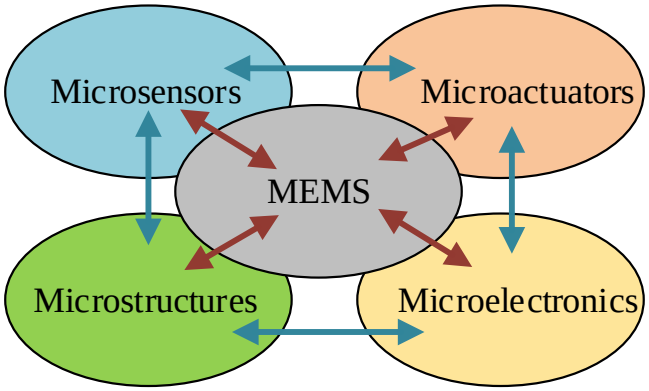

Figure 3-1 Schematic illustration of MEMS components

Many MEMS components are currently available on the market, and these can be generally divided into six groups including inertia sensor, pressure sensor, microfluidics / bioMEMS, RF MEMS, optical MEMS / MOEMS and others. The most well-known categories are pressure sensors and inertia sensors, which comprise many component types such as accelerometers and gyroscopes, produced by different manufacturers, including for example Motorola, Analog Devices, Sensonor and Delphi [106].

Recently, MEMS sensors have come to be widely used in machine condition monitoring to measure different signals such as vibrations, pressure and temperature [98, 107]. However, most of the previous research has used MEMS sensors as stationary transducers. This research focuses on the usage of on-rotor MEMS accelerometers for machine condition monitoring.

3.2.1 MEMS Accelerometer

The first MEMS accelerometer was designed at Stanford University in 1979, however, it took very long time, around 15 years, before such devices became acceptable for the real applications [108]. Modern MEMS accelerometers are tiny devices; made at different sizes from a few micrometres to millimetres, they are low cost and low power consumption, and they can measure dynamic acceleration (e.g., vibration) as well as static acceleration (e.g., gravity). Normally, these acceleration measurements are made in units of g, where $1g$ is the acceleration caused by Earth's gravity at 9.8 m/s^2 [109].

As shown in Figure 3-2, the main component of a typical MEMS accelerometer is the moving beam structure made up of two sets of fingers: the first finger set is stationary, mounted on a

solid ground plane on a substrate, while the other is a moving finger set, and is attached to a mass connected to springs.

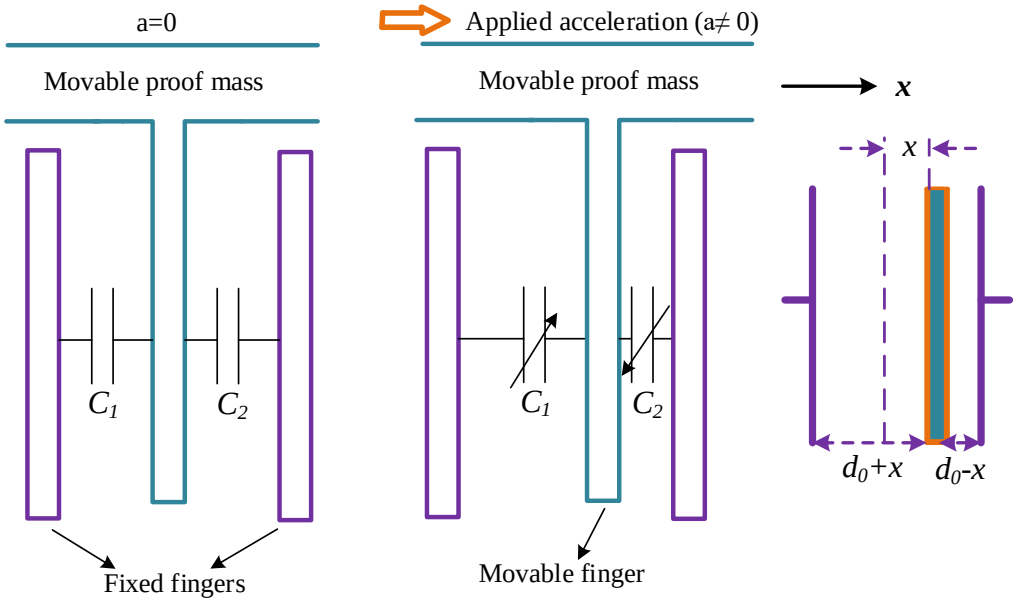

Figure 3-2 The structure of a MEMS accelerometer [110]

When the applied acceleration equal to zero (no acceleration), the movable fingers will be precisely at the middle between the right and left fixed fingers as presented in Figure 3-2. In this case, the capacitance of C_1 equal to C_2 and can be denoted as C_0 as calculated in Equation 3-1 [110].

$$C_0 = \frac{\varepsilon_0 \varepsilon_r N_s L_s h}{d_0} \tag{3-1}$$

Where ε_0 indicates the permittivity constant, ε_r denotes the dielectric constant of the air, h is the finger height, d_0 is the air gap distance between each movable finger and the fixed fingers, N_s is the sensing fingers number and L_s is the length of the sensing finger.

When there is an acceleration $(a \neq 0)$, the movable finger will be moving causing a change in both capacitances C_1 and C_2 because of displacement (x) of the movable as shown Finger 3-2.The capacitances C_1 and C_2 can be calculated using Equations 3-2 and 3-3 [110].

$$C_1 = \frac{\varepsilon_0 \varepsilon_r N_s L_s h}{d_0}\left[1+\frac{x}{d_0}\right] \tag{3-2}$$

$$C_2 = \frac{\varepsilon_0 \varepsilon_r N_s L_s h}{d_0}\left[1-\frac{x}{d_0}\right] \tag{3-3}$$

In such devices, the air gap between the fingers (d_0) should be very large compared with the displacement (x) and the maximum displacement is typically limited by 20% of d_0. Once the acceleration is existing, the capacitance of C_1 and C_2 become different, and the difference between them can be calculated as [110]:

$$\Delta C = C_1 - C_2 = \frac{2\varepsilon_0 \varepsilon_r N_s L_s h}{d_0}\left[\frac{x}{d_0}\right] = 2C_0\left[x/d_0\right] \tag{3-4}$$

This sensing technique is well known in terms of its stability, lower power loss, high accuracy, and simple structure to build. Most MEMS accelerometer sensors measure the displacement of a mass and then the measured signals are passed through an analogue-to-digital converter (ADC) to convert it into a digital electrical signal which can be used for digital processing.

In this research, ADXL345 is used to measure on-rotor acceleration. It is a small, thin, 3-axis accelerometer which has three separate outputs that determine acceleration along the axes (X, Y, and Z). Figure 3-3 shows the functional block diagram of ADXL345 accelerometer. More details about the MEMS accelerometer used in this work will be given in Chapter Four.

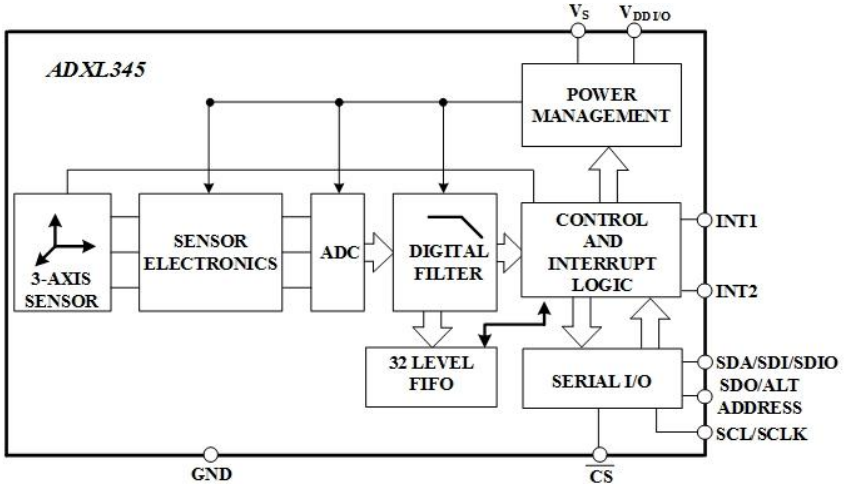

Figure 3-3 Accelerometer block diagram

For on-rotor MEMS accelerometer, some sensor specifications should be considered to choose the suitable one for rotating machines condition monitoring including sampling frequency, noise floor, sensitivity, dynamic range, size, number of outputs and power consumption level [111]. Below is brief descriptions of some specifications normally listed on their datasheet [98] [112].

- *Measurement Range:* it is the maximum range of the acceleration obtained by the accelerometer.
- *Shock Limit:* it can be defined as the maximum acceleration that one accelerometer can withstand without causing damage to the sensors.
- *Sensitivity:* is the ratio of output to the input. For MEMS accelerometer, it signifies the ratio of the electrical output (voltage/acceleration) to its mechanical input. For digital accelerometers, the sensitivity is expressed as LSB/g (least significant bit per g). If the amplitude of the vibration is small, one need to have high sensitive accelerometers to provide the signal with high signal to noise ratio (SNR).
- *Resolution:* is the smallest mechanical changing in the input for which a change in the electrical output is desirable. Resolution is specified in bits which can be further analyzed in acceleration unit of power 2. For example, if an accelerometer system has 13-bit resolution; that means it has 2^{13} or 8192 acceleration levels it can measure. For a ±16g measurement range this equates to a resolution of 0.0039 (32/8192) which is the smallest measurable acceleration level
- *Frequency Range*: It is the range beyond that the sensitivity of the transducer does not change that much from the rated sensitivity. This range can be limited by the transducer mechanical characteristics or its associated equipment.

3.3 Wireless Technology in Condition Monitoring

As mentioned earlier, wired online condition monitoring systems are successfully applied in many industrial settings. However, these systems rely on different types of cables for field applications, and installation, maintenance and cost become the major obstacles to their wider applications [113]. Providentially, there have been significant developments in wireless data communication technologies that can be used to transfer data instead of using communication cables.

Currently, wireless technologies are widely used and have gained great attention in industry for collecting and transferring data used for machinery condition monitoring due to their inherent advantages: for example, they are low cost, suitable for isolated environments, offer convenient installation and are easy to upgrade [14], [113], [114]. In remote condition monitoring systems, a number of requirements should be considered in order to decide which wireless technology is most suitable for data transmission. Bandwidth, power consumption, bit error rate, length of data transmission, transmission speed, and security are some of these requirements [115].

In general, wireless network standards can be divided, based on signal range, into four categories; 1) regional area network (RAN); 2) wide area network (WAN); 3) metropolitan area network (MAN); 4) local area network (LAN); and 5) personal area network (PAN), as presented in Figure 3-4 [14, 113].

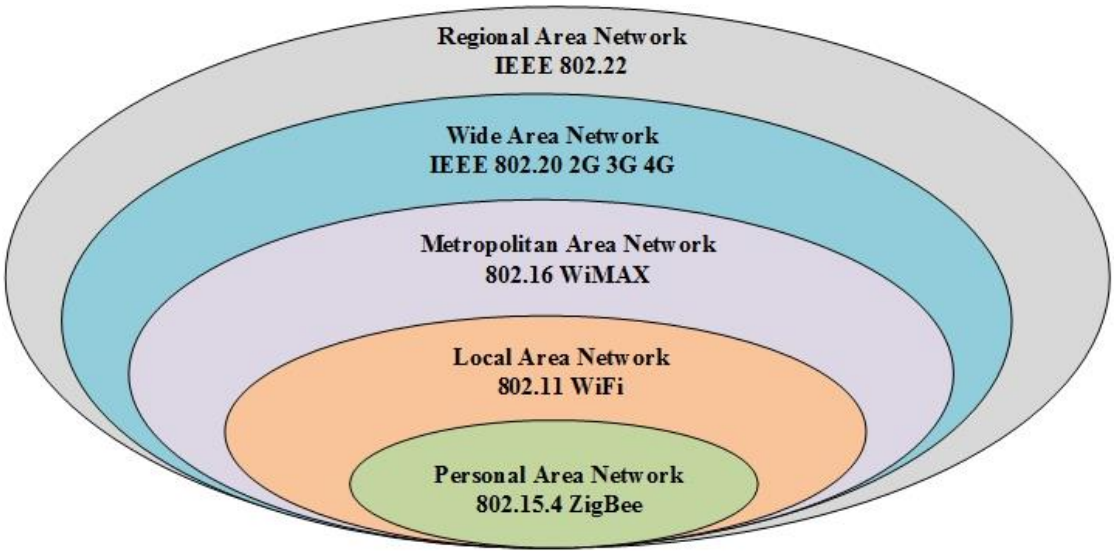

Figure 3-4 Types of wireless networks [116]

Networking standards deal with the physical layer and the lower part of the data link layer, called the MAC (medium access controller) sub-layer. The physical layer tackles modulation, frequency, and transmission, whereas the MAC sub-layer relates to access points maintaining signal flow order thereby avoids signal collision and cancellation [117, 118].

3.3.1 Wireless Protocols for WSN

Different standards have been designed for wireless communications to meet various application area requirements. The most widely-known protocols that have been employed in the WSN are Wi-Fi, ZigBee and Bluetooth, which correspond to the 802.11a/b/g, IEEE 802.15.4 and 802.15.1, standards, respectively [119], [120].

3.3.1.1 WiFi over IEEE 802.11

All 802.11(a/b/g/n) [56, 57] communications utilise the Industrial, Scientific and Medical (ISM) frequency bandwidths, which do not require a license. However, the exact radio portions of the ISM bands used by these devices may vary in different countries. The bandwidth sets by the European Telecommunications Standards Institute (ETSI) are 2.4-2.5 and 5.47-5.725 GHz. Rates of data transmission also vary and are affected by the IEEE 802.11 version. Thus, 802.11b, which utilises Direct Sequence Spread Spectrum (DSSS), provides a maximum of 11Mbps using a 2.4GHz band, while 802.11a, which uses Orthogonal Frequency Division Multiplexing (OFDM), provides as much as 54 Mbps using a 5GHz band [121].

Although the data transmission rate for the Wi-Fi network is very high compared with the other wireless networks, the critical issue of its significant power consumption makes Wi-Fi a poor candidate for battery-powered wireless sensor node applications.

For wireless condition monitoring and fault diagnosis, very few researchers have used this standard to send data to the base station. Hashemian et al. (2011) used an 802.11g to send vibration signals acquired at the motor and fans, which are part of the reactor building ventilation system. To confirm the performance of the wireless system, a wired data acquisition system was used and compared with the wireless one and the results displayed good agreement between wired and wireless systems [122].

3.3.1.2 ZigBee over IEEE 802.15.4

The standard IEEE 802.15.4 gives a definition for protocols and interconnecting devices using radio communications across personal area networks (PANs). The standard is active within ISM bands, in Europe at 868 MHz, in the US at 915 MHz and at 2.4 GHz globally. This offers data rates of 250kbps, 40 kbps and 20kbps at bands of 2.4GHz, 915MHz and 868MHz respectively [123]. The standard aims to cover wireless connection between low-cost devices which is simple and inexpensive with low data rates and minimal energy use. It is possible to use ZigBee technologies across different industrial applications in medical equipment, intruder

sensors, embedded sensor equipment, smoke alarms and automated features for buildings, among other applications. ZigBee networks offer extremely low energy consumption, meaning that a device could possible function for over a year on just one alkaline battery.

Considering these characteristics of the IEEE 802.15.4/ZigBee, this technological solution is well-suited to condition monitoring and fault detection for industrial machinery using a wireless sensor network. The network layer of ZigBee can support mesh, tree and star type topology [124]. Wireless devices complying with ZigBee have an expected transmission distance of between 10 and 75 meters, based on the RF setting and the application's particular energy output requirements [123].

In wireless sensor network based fault diagnosis systems, many studies have used ZigBee as a wireless standard to send different measured parameters such as vibrations [125], current [126] and temperature [30] remotely to a host computer, to be used for condition monitoring/ detecting faults. One of the successful applications of ZigBee as a wireless protocol used for data transmission can be found in fault detection and diagnosis based on induction motor stator current and vibration signals in which stator open phase faults and one and two bearing imbalance faults were successfully identified [126].

3.3.1.3 Bluetooth Classic and Bluetooth Low Energy over IEEE 802.15.1

Bluetooth is also a candidate to substitute for implementing WSN, but this protocol has paid less attention based in Bluetooth's complex nature and power parameters which are insufficient for sensor applications [127].

Bluetooth-Low-Energy (BLE) is a new version of the traditional Bluetooth developed by the Bluetooth Special Interest Group (SIG) [118]. The specification for BLE is included within that for Bluetooth, with its extremely low power requirements making it suitable for use in devices with minimal battery power. With BLE, Bluetooth becomes capable of a top data rate of 1 Mb/s at 2.4 GHz across between 5 and 10 meters [128]. BLE was designed to overcome some of Bluetooth's disadvantages, which are outlined below [129]:

- The power consumption of transceiver chips is very high.
- Suboptimal timing behaviour: for example, a long time duration is needed for the connection setup time.
- Its protocol stack is very complex, resulting in the need for a large memory.
- Large data packets with huge overheads during wireless transmissions.

- Data transmission rate is relatively slow.

In this work, BLE has been chosen as the wireless transmission media to send on-rotor acceleration data to a remote computer for further signal analysis. This wireless protocol has many features and advantages that make it different from the other standards. For instance, Bluetooth devices are widely available, their cost is quite cheap and they offer low power consumption [115]. Dementyev (2013) found that among different wireless standards, BLE achieved the lowest power consumption, followed by ZigBee [130]. These benefits make BLE a suitable wireless technology for many wireless condition monitoring systems and maintenance applications, including that achieved in this research.
Some features of the mentioned standards are abridged in Table 3-1.

Table 3-1 Features for wireless standards [131], [132], [133].

	Bluetooth	BLE	ZigBee	Wi-Fi
IEEE spec.	802.15.1	802.15.1	802.15.4	802.11a/b/g
Frequency band	2.4 GHz	2.4 GHz	868/915 MHz; 2.4 GHz	2.4 GHz; 5 GHz
Max signal rate	3Mb/s	1Mb/s	250 Kb/s	54 Mb/s
Nominal range	10 m	50 m	10 - 100 m	100 m
Channel bandwidth	1 MHz	2 MHz	0.3/0.6 MHz; 2 MHz	22 MHz
Modulation type	GFSK	GFSK	BPSK (+ ASK), O-QPSK	BPSK, QPSK COFDM, CCK, M-QAM
Spreading technique	FHSS	FHSS	DSSS	DSSS, CCK, OFDM
Current consumption	< 30 mA	< 15 mA	19 mA Rx, 35 mA Tx	60 mA Rx, 200 mA Tx

3.4 Challenges of Remote Condition Monitoring

Recently, wireless condition monitoring has been successfully applied in different commercial areas: for instance, environmental sensing, automation, structured health monitoring etc. Nevertheless, there are several challenges to phased wireless condition monitoring, including sensor battery operation lifetime, interference, high rates of data transmission, high rates for sampling, reliability and security.

- Battery operation:

In most wireless sensor nodes, rechargeable batteries are used to power the sensor. The battery lifespan may be different from one application to another and this is affected by many factors, such as its physical size, sampling rate, time required for data acquisition, how often the wireless sensor needs to sense the signals, and the transmission protocol used to send the measured data. As the battery energy is limited, thus its lifespan is a major issue and one which should be considered for wireless condition monitoring systems. Battery recharging or replacement costs are certainly not negligible and this also could be a time consuming process. In some applications, it may not be easy to replace the sensor node battery, and due to this, a renewable power supply source might be used instead of a battery, and this is dependent on the machine's constriction, its function and the environment where the machine is located [134]. Many studies have investigated the use of environmentally-sourced energies such as solar [135], wind [136], water flow [136], vibration [137] and thermal [138] energy, to power the wireless sensor node.

Another challenge associated with wireless sensor node batteries is the ability to report a reliable and accurate estimation of remaining battery lifetime. Therefore, a plan for battery performance monitoring to estimate the remaining battery lifetime, without affecting the WSN tasks, is required [139].

- *Reliability:*

Providing accurate and real-time information is another challenge in industrial wireless condition monitoring, and especially in harsh environments under extreme vibration or high noise conditions, in which the measured parameters usually face data loss issues during the transmission stage. Therefore, more reliable communication is required.

- *High data transmission rates:*

In some applications, the dynamic signals needed to be measured at a high sampling rate, producing a huge chunk of data which needs to be sent at a high data transmission rate, while this rate may be restricted or limited by wireless bandwidth.

- *Security requirements:*

Security for many industrial applications has recently become a significant issue associated with wireless condition monitoring. As some of these industrial applications require high

security communications, special attention has been paid to providing the level of security required for each application [128].

- *Interference*

In industry, the coverage area for wireless devices may suffer from noise, co-channel interference, multipath propagation, and other sources of interference. For instance, the signal strength may be harshly affected by electromagnetic signals produced by heavy machines located near the transmitter or receiver, multipath propagation or interference from other wireless devices that use ISM bands [140]. The impact of interference between the wireless sensor and other signals in the plant is another concern that should be considered when a wireless condition monitoring system is designed [128].

3.5 Wireless Technologies and MEMS Accelerometers for Condition Minoring

The recent growth of automation in the industry ensures the need of more reliable and intelligent machine systems that can minimize the cost of sudden failures when they are under operation. An effective intelligent condition monitoring technique is required which can provide the necessary information about the machine health time to time minimizing the cost of machine downtime. Usually condition monitoring technique measures the dynamic responses like IAS, current and vibration signal to monitor the machine performance [141].

Vibration signals collected from the rotating machines such as pumps, compressors, motors, gearboxes and generators have traditionally been used for fault detection and diagnosis as they can carry a valuable dynamic information related to the machine conditions. Many techniques including time domain analysis [17, 142, 143], frequency domain analysis [144] and time frequency domain analysis [145, 146] have been developed to process the vibration signal. However, the useful information from a vibration signal often get contaminated with the structure borne noise. Beside this, signal strength also depends on the location of the sensor [147]. Thus, sometimes it has a low signal-to-noise ratio (SNR). In the way to achieve an improved SNR value for a signal, nowadays the researchers are using IAS signal for the detection of faults in rotating machineries [147]. The reason of using the IAS signal is that any faults in a rotating machine has its influence on the angular speed the present of faults in a rotating machine always affects the angular speed of the output shaft. Thus, the faults can be

effectively identified in a rotating machine by analyzing the IAS signal. Recently, many studies [13, 90, 148] have reported the use of IAS signal in the diagnosis of machine faults. The most common and accurate way to measure the IAS signal is by installing an optical encoder which involves lower cost than the conventional accelerometers and can provide better resolution than the other IAS measuring devices. On the other hand traditional encoders have been used for a long time in the industry to monitor machines' performance and its' fault detection. However, these sensors are still expensive and are not suitable for isolated environments with difficulty in installation.

In machinery condition monitoring, the selection of the proper transducers is very essential so that it can provide an accurate measurement in both time and frequency domains. The conventional large transducers used for machinery condition monitoring require a wired connection to transfer the measured vibration data to the computer node and have a narrow frequency bandwidth, which in term reduce their accuracy, versatility and applicability to the smaller machineries.

In recent years, many researchers have studied the feasibility of using MEMS accelerometers and wireless transmission technologies for machine condition monitoring. Raj et al. (2013) studied and demonstrated the importance of using vibration signals measured using a MEMS accelerometer in fault detection of a three-phase induction motor. Their experimental results show that misalignment and loose mounting produces additional amplitude and frequency modulations, providing an easy and cheap way to detect and characterize both mechanical and electrical faults in the induction motor [149]. Kumar et al. (2016) investigated and evaluated the usage of a wireless sensor inside an induction motor and sent data through IEEE 802.15.4 wireless radio communication [150]. Their findings show that the quality of the wireless link is relatively good and the effect of magnetic fields on wireless link quality is not noticeable.

Besides, Sarkimaki et al. (2005) concentrated on the capability of different wireless technologies to collect and transfer data used for condition monitoring, and the requirements to be considered when choosing a suitable transmission protocol were discussed [115]. Medina et al. (2017) implemented a low cost, low power and highly reliable remote condition monitoring system for a three-phase squirrel cage motor. The wireless sensors measured various parameters, including vibrations, temperature and current consumption, providing an

effective way for mechanical fault detection. The data was sent to a remote PC through a wireless sensor network based on the IEEE 802.15.4 standard for further signal analysis [151].

Moreover, several studies have investigated the MEMS accelerometer when it is directly mounted on a machine to monitor condition. Albarbar et al. (2008) studied the suitability of using a MEMS accelerometer in condition monitoring, and the performance of three different types of MEMS accelerometer was investigated. Their paper concluded that MEMS sensors could be used instead of standard sensors especially for wireless implementation [98]. Arebi et al. [99] developed a WMA that was attached directly on a rotating shaft and the results demonstrated that different degrees of misalignments could be successfully monitored using a MEMS accelerometer. Moreover, an analysis of the data collected via a WMA and a shaft encoder was achieved in [152] to compare their responses under different degrees of shaft misalignment. According to their results, the wireless MEMS accelerometer performance was better than the shaft encoder at detecting small shaft misalignment.

3.6 On-Rotor MEMS Accelerometer Measurements

Here the output from a MEMS accelerometer that is attached to a rotor is analysed. For this purpose, we define two separate Cartesian coordinate systems (as shown in Figure 3-5). The first coordinate system has a stationary frame of reference (represented by XO-YO-ZO) and is helpful in providing the reference for any rotating bodies that includes the rotor and the MEMS sensor on it. The other coordinate system is attached to a rotating reference frame (represented by X-Y-Z) and rotates at rotor speed. The three positive outputs from the on-rotor MEMS accelerometer is aligned to each of the coordinates, respectively. The Y-axis of the accelerometer, which stays fixed on the rotor, is directed along the tangent of its rotating track. Furthermore, it is seen from the figure that the MEMS sensor assumes an initial phase of (θ_0) with respect to the stationary coordinate frame. It must be noted that the initial phase of any measurable rotation parameter, say, angular speed (ω), is considered to have a zero value for the sake of ease in analysis. Therefore, it is clear that θ_0 also depicts the phase difference between the initial phase of the rotor motion and sensor and the initial phase of the rotor oscillation [97].

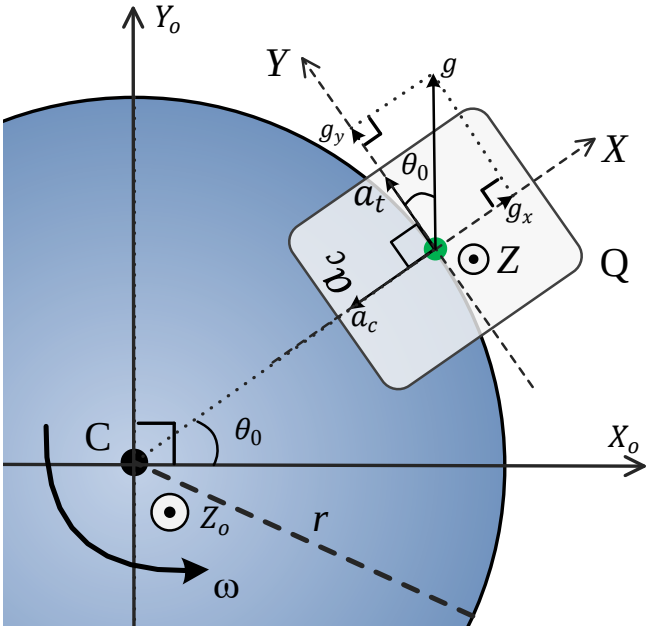

Figure 3-5 Acceleration analysis of a mass Q rotating around point C [97]

As the rotor revolves about the centre C at the speed of ω, both the centripetal acceleration a_c and tangential acceleration a_t at radius r can be measured by the MEMS sensor in the both X-axes and Y-axes, respectively. Simultaneously, the MEMS accelerometer also senses the gravitational acceleration, whose projections on the X- and Y- axis change with the rotating process respectively. Thus, the overall outputs of the sensor are:

$$a_x = -a_c + g_x \tag{3-5}$$

$$a_y = a_t + g_y \tag{3-6}$$

where g_x and g_y indicate the gravitational acceleration projected on the X- and Y-axis individually. It is apparent that the estimated signals comprises of both parts; the rotatory motions implying rotor dynamics and the innate acceleration due to gravity that interacts with the rotatory dynamics. Undesirable gravitational accelerations have to be eliminated or at least minimized from the output measurements so as to precisely characterize the rotor dynamics [97].

3.6.1 Centripetal and Tangential Acceleration

The rotor motion is associated with an unsteady speed, ω which relates to the angular acceleration as $\alpha = d\omega/dt$, then the two relevant acceleration components, namely, the centripetal (a_c) and the tangential (a_t) reads:

$$a_c = \omega^2 r \tag{3-7}$$

$$a_t = \alpha\ r \tag{3-8}$$

It is assumed that the angular speed to be measured is $\omega = \omega_0 + \tilde{\omega}$, where ω_0 is the steady angular speed and $\tilde{\omega}$ denotes the dynamic angular speed, which means its amplitude varies with time. Therefore, centripetal acceleration a_c and tangential acceleration a_t can be expressed as [97]:

$$a_c = \left(\omega_0 + \tilde{\omega}\right)^2 r = r\omega_0^2 + 2r\omega_0\tilde{\omega} + r\tilde{\omega}^2 \tag{3-9}$$

$$a_t = r\frac{d\tilde{\omega}}{dt} \tag{3-10}$$

According to the National Electrical Manufacturers Association (NEMA) [12], most AC squirrel-cage induction motors have a maximum slip ratio of 5%. This means the speed of induction motor drives fluctuates within around 5% of their rated speeds, making it acceptable that $\tilde{\omega}/\omega_0 \ll 1$. Thus, the quadratic term $r\tilde{\omega}^2$ can be ignored. Moreover, the steady term $r\omega_0^2$ is not interesting for dynamic investigation. Therefore, the dynamic centripetal acceleration $\tilde{a}_c$ can be approximated as:

$$\tilde{a}_c \approx 2r\omega_0\tilde{\omega} \tag{3-11}$$

In addition, the dynamic angular speed is implemented as a periodical signal expressed as:

$$\tilde{\omega} = \sum_{n=1}^{\infty} A_n \sin\left(n\omega_p t + \varphi_n\right) \tag{3-12}$$

where A_n and φ_n denote the amplitude and phase of the n^{th} harmonic component of $\tilde{\omega}$ individually, and ω_p is the fundamental frequency of the periodical signal. For numerous rotating processes, ω_p can equal the steady angular speed ω_0 then, the dynamic angular speed $\tilde{\omega}$ can be given as [97]:

$$\tilde{\omega} = \sum_{n=1}^{\infty} A_n \sin\left(n\omega_0 t + \varphi_n\right) \tag{3-13}$$

Therefore, the centripetal ($\tilde{a}_c$) and the tangential ($\tilde{a}_t$) components of the acceleration vector recast in terms of the fundamental harmonic frequency and their combinations as [97]:

$$\tilde{a}_c \approx \sum_{n=1}^{\infty} 2r\omega_0 A_n \sin\left(n\omega_0 t + \varphi_n\right) \tag{3-14}$$

$$\tilde{a}_t \approx \sum_{n=1}^{\infty} nr\omega_0 A_n \cos\left(n\omega_0 t + \varphi_n\right) \tag{3-15}$$

3.6.2 Gravitational Acceleration Projection Signal

As shown in Figure 3-5, there is an acceleration component upward with an amplitude of $1.0g$ and opposite to the real gravitational acceleration. This component implements the gravitational acceleration sensed by a MEMS accelerometer on both X-axis g_x and Y-axis g_y in which these projected signals can be written as:

$$g_x = g\sin\theta \tag{3-16}$$

$$g_y = g\cos\theta \tag{3-17}$$

where θ denotes the angular displacement of the on-rotor MEMS accelerometer at time t and can be obtained according to the angular speed ω as

$$\theta = \theta_0 + \int_0^t \omega dt \tag{3-18}$$

Assuming the angular speed is consisting of the steady component ω_0 and dynamic component $\tilde{\omega}$; therefore, the angular displacement of the MEMS sensor can be expressed as [97]:

$$\theta = \theta_0 + \int_0^t \left(\omega_0 + \tilde{\omega}\right) dt \tag{3-19}$$

$$\theta = \theta_0 + \omega_0 t + \int_0^t \tilde{\omega} dt \tag{3-20}$$

Equation (3-20) displays that the total angular displacement consists of three components, which are the initial phase θ_0, linear progression displacement due to steady speed ω_0 and displacement oscillation due to dynamic angular speed $\tilde{\omega}$. Displacement oscillation can be expressed as:

$$\varphi(t) = \int_0^t \tilde{\omega} dt = \frac{1}{\omega_0} \sum_{n=1}^{\infty} \frac{A_n}{n} \left[-\cos\left(n\omega_0 t + \varphi_n\right) + \cos\varphi_n \right] \tag{3-21}$$

As a result of the oscillation of the angular displacement, the projections in Equations (3-16) and (3-17) exhibit angle modulation, which means they might have numerous components of higher orders. On the other hand, and compared to the steady operation of conventional machines, the amplitude of $\phi(t)$ is typically small. Therefore, the linear term $\phi(t)$ is the only one that will be considered in derivation of the projections, so

$$g_x = g \sin\left[\theta_0 + \omega_0 t + \varphi(t)\right] \tag{3-22}$$

$$g_x \approx g \sin\left(\theta_0 + \omega_0 t\right) + g\varphi(t)\cos\left(\theta_0 + \omega_0 t\right) \tag{3-23}$$

$$g_y = g \cos\left[\theta_0 + \omega_0 t + \varphi(t)\right] \tag{3-24}$$

$$g_y \approx g \cos\left(\theta_0 + \omega_0 t\right) - g\varphi(t)\sin\left(\theta_0 + \omega_0 t\right) \tag{3-25}$$

Equations (3-23) and (3-25) demonstrate the contents of both the projected gravity signals. The gravity signal comprises not only of a primary carrier signal having frequency ω_0 and amplitude g but also a series of small auxiliary sidebands having $\pi/2$ phase difference with

the former counterpart. From Equations (3-21) one may estimate the sideband amplitudes and by replacing (3-21) into (3-23) and (3-25) one may calculate the respective projections on the X- and Y-coordinates [97].

$$g_x \approx g\sin\left(\theta_0+\omega_0 t\right)+\frac{g}{\omega_0}\sum_{n=1}^{\infty}\frac{A_n}{n}\left\{\begin{array}{l}-\frac{1}{2}\cos\left[\left(n+1\right)\omega_0 t+\theta_0+\varphi_n\right]-\\ \frac{1}{2}\cos\left[\left(1-n\right)\omega_0 t+\theta_0-\varphi_n\right]+\cos\varphi_n\cos\left(\theta+\omega_0 t\right)\end{array}\right\} \tag{3-26}$$

$$g_y \approx g\cos\left(\theta_0+\omega_0 t\right)+\frac{g}{\omega_0}\sum_{n=1}^{\infty}\frac{A_n}{n}\left\{\begin{array}{l}\frac{1}{2}\sin\left[\left(n+1\right)\omega_0 t+\theta_0+\varphi_n\right]+\\ \frac{1}{2}\sin\left[\left(1-n\right)\omega_0 t+\theta_0-\varphi_n\right]-\cos\varphi_n\sin\left(\theta_0+\omega_0 t\right)\end{array}\right\} \tag{3-27}$$

Using Equations (3-15) and (3-27), both gravity projected on the Y-axis and tangential acceleration signals may be presented in the time domain and frequency domain.

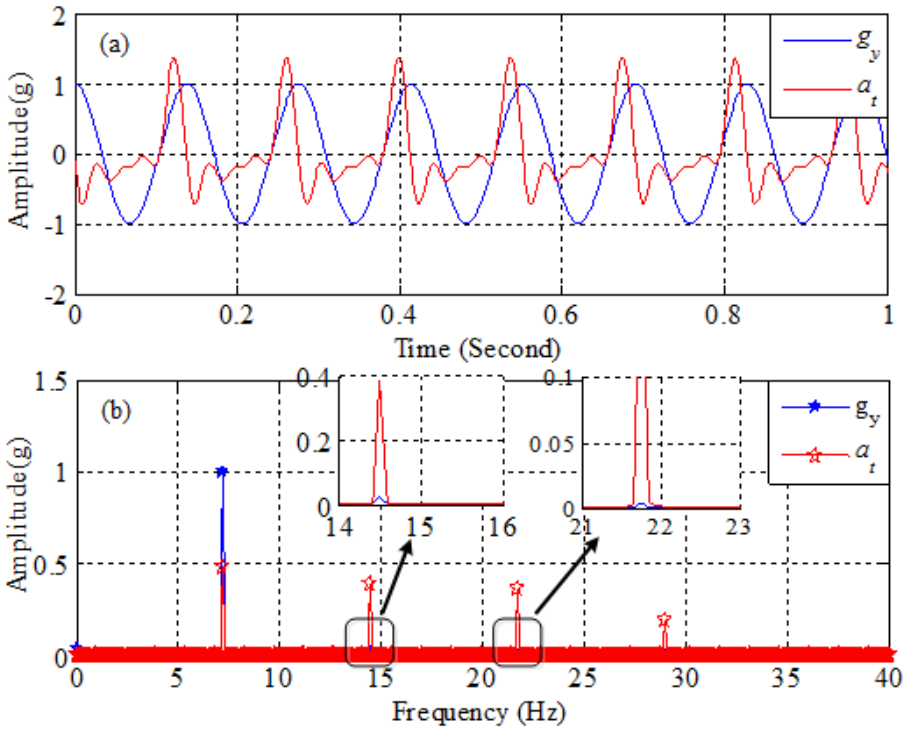

Figure 3-6 Accelerations measurements (a) tangential acceleration and gravity signal projected on Y-axis g_y in time domain (b) frequency components

From Figure 3-6, it is noted that both gravitational acceleration and tangential acceleration changes with time have similar frequency components, which means it is difficult to separate them and obtain the tangential acceleration using a low pass filter [153]. Here one needs to eliminate the acceleration due to gravity in order to put the dynamic information of the rotor into use in regards to condition monitoring. The next sections introduce a new method used to eliminate gravitational acceleration using the two outputs of one MEMS accelerometer.

3.7 Tangential Acceleration Reconstruction

The approximated outputs of the X- and Y- axis can be obtained by substituting Equations (3-14), (3-15), (3-26) and (3-27) into Equations (3-5) and (3-6) respectively.

$$\tilde{a}_x = -\tilde{a}_c + g_x \approx -\sum_{n=1}^{\infty} 2r\omega_0 A_n \sin\left(n\omega_0 t + \varphi_n\right) + g_x \tag{3-28}$$

$$\tilde{a}_y = \tilde{a}_t + g_y \approx \sum_{n=1}^{\infty} nr\omega_0 A_n \cos\left(n\omega_0 t + \varphi_n\right) + g_y \tag{3-29}$$

Equations (3-26) and (3-27) show that g_x and g_y enjoys similar amplitude but have a $\pi/2$ phase difference for all frequency components.

To remove the effect of gravitational acceleration, the sensor outputs are processed via the following four stages [97]:

1- Apply low-pass filters to $\tilde{a}_x$ and $\tilde{a}_y$ so that high frequency noise is removed.

2- Apply Hilbert transform (HT) to produce a $\pi/2$ phase shift in $\tilde{a}_x$ as the filtered signal.

3- The phase-shifted and filtered $\tilde{a}_y$ signals are added together to produce a signal without gravitational acceleration components and therefore which only contains tangential components:

$$a_{tx} = \sum_{n=1}^{4} \left(n+2\right) r\omega_0 A_n \cos\left(n\omega_0 t + \varphi_n\right) \tag{3-30}$$

Comparing (43-30) with $\tilde{a}_t$ in (3-15), the frequency phases and components of both signals show similarity. However, the amplitude of n[th] harmonic is $(n+2)/n$ multiple of the true one. Obviously, it is simple to rectify this constant difference, which is done in step 4.

4- Multiply the amplitude of n[th] harmonic component of a_{tx} by $n/(n+2)$ to get the pure tangential acceleration signal a_t as expressed in Equation (3-31).

$$a_{tx} = \sum_{n=1}^{4} nr\omega_0 A_n \cos(n\omega_0 t + \varphi_n) \tag{3-31}$$

Thus, Equation 3-31 clearly expresses the fact that the orthogonal results derived from on-rotor accelerometer (MEMS) is useful to eliminate the effect of acceleration due to gravity that is projected on the X-coordinate, which enables one to accurately exemplify the investigated rotor dynamics.

3.7.1 Performance Analysis

To estimate the performing capacity of one MEMS technique presented in this chapter and used to eliminate gravitational signals, simulation of the rotating system of a two-stage reciprocating compressor is performed and the equations explained in Sections 3-6, 3-6-1 and 3-6-2 are used to obtain the associated acceleration signals.

A 3-phase induction motor (KX-C184 with a power rating of 2.5kW) drives the compressor wherein the power transfer to the flywheel of the compressor takes place via a pulley belt arrangement that has a 3.2:1 transmission ratio. The rated motor speed, which is about 1420 revolutions per minute (rpm), implies that the flywheel speed is approximately 440 rpm. Figure (3-7) shows the waveform and spectrum of the angular speed of the crankshaft and by taking this signal as the input, tangential accelerations $\tilde{a}_t$, the dynamic centripetal acceleration $\tilde{a}_c$, gravitational acceleration projections g_x and g_y are calculated according to the models given in this chapter and presented in Figure (3-8). Because of the reciprocating movement of the piston, it is assumed that the speed will be fluctuated with a ratio of 5% [45], [154]. This means that the dynamic angular speed amplitude should be no more than $440 \times 5\% = 22$ rpm.

Previous work measuring instantaneous speed [45], uses as many as 3 higher orders of harmonics in order to include the impacts of nonlinear torque caused by the movement of the piston and compression of air in the representation. In particular, simulation of the crank shaft's angular speed may be achieved as follows:

$$\omega = \frac{2\pi}{60}\left[\begin{array}{l} 440 + 20\sin\left(2\pi\frac{440}{60}t + \frac{\pi}{3}\right) + 8\sin\left(4\pi\frac{440}{60}t + \frac{\pi}{2}\right) + \\ 5\sin\left(6\pi\frac{440}{60}t + \frac{2\pi}{3}\right) + 2\sin\left(8\pi\frac{440}{60}t + \frac{3\pi}{4}\right) \end{array}\right] \tag{3-32}$$

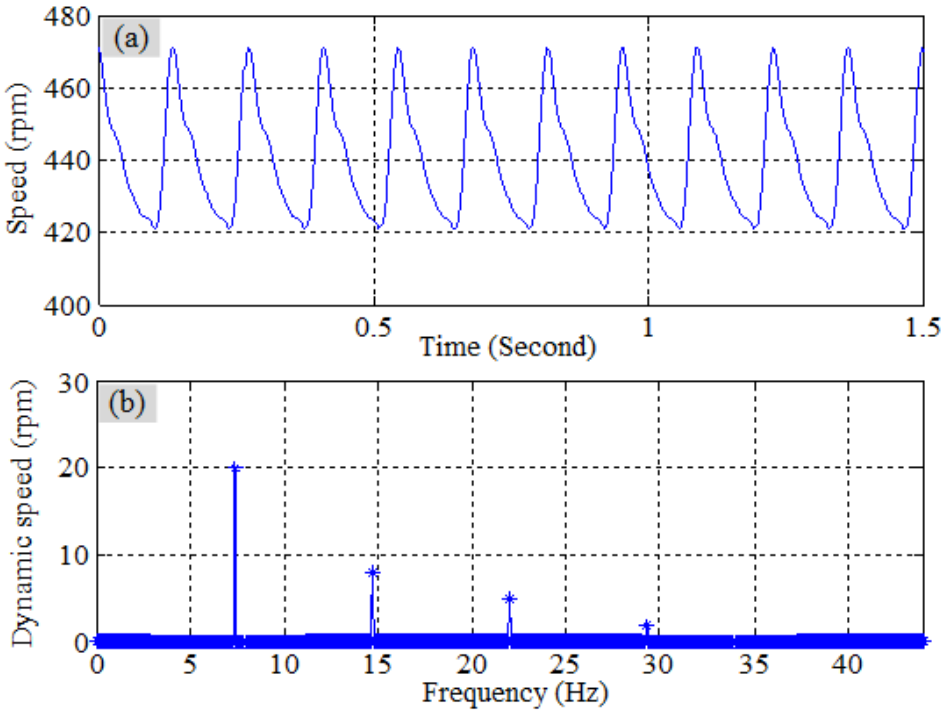

Figure 3-7 Angular speed (a) time domain waveform and (b) its representation frequency domain

Figure (3-8) shows the gravity signal projected g_x and g_y as controlled by the fundamental frequency components, and the angle modulated sidebands of g_x and g_y are hardly noticeable. This means that g_x and g_y given in Equations (3-26) and (3-27) can be approximated by merely accounting the linear term $\varphi(t)$ of significance. On the other hand, clear higher order

harmonics can be observed in the frequency spectrum of both dynamic centripetal acceleration $\tilde{a}_c$ and tangential acceleration $\tilde{a}_t$.

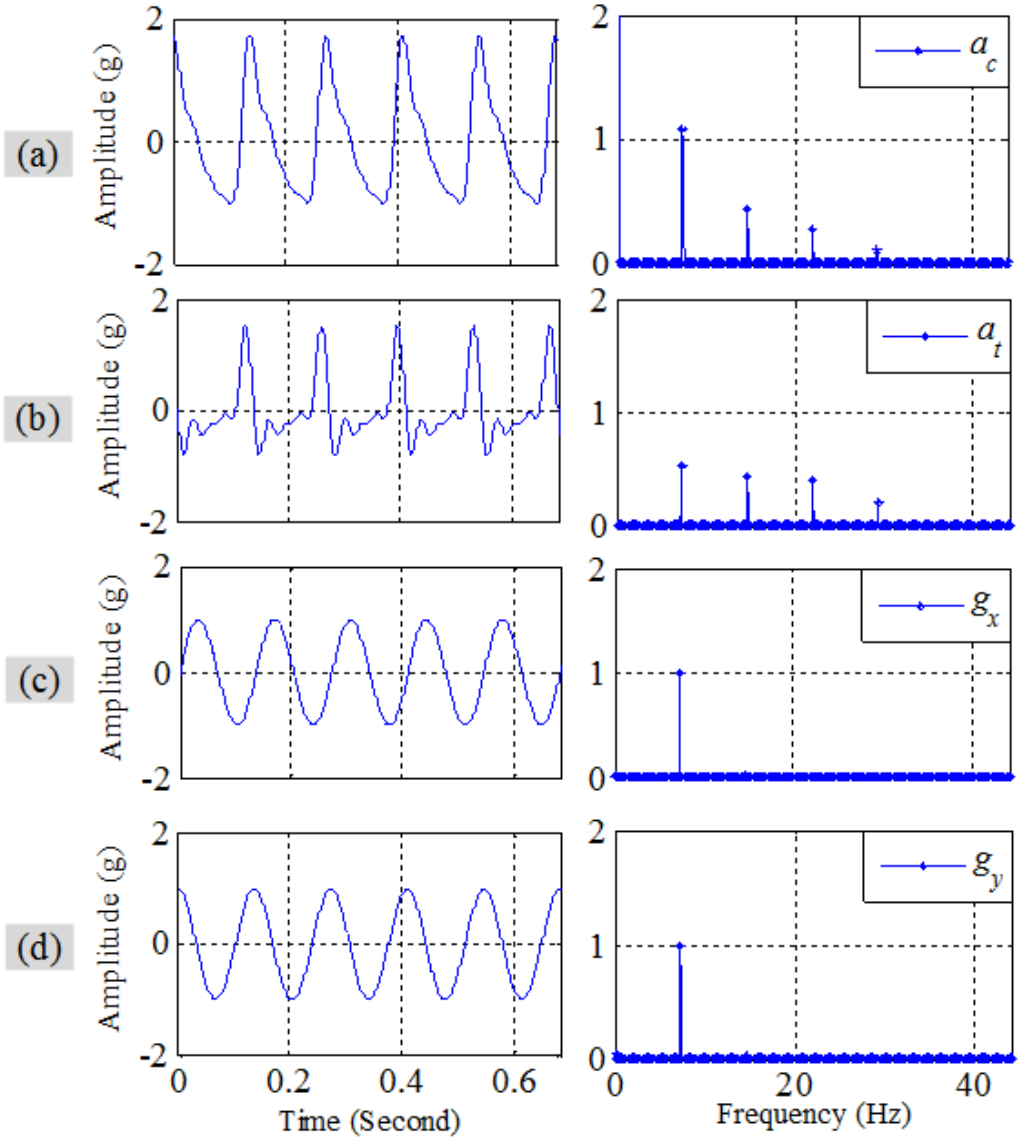

Figure 3-8 True accelerations and their spectrum (a) centripetal acceleration $\tilde{a}_c$, (b) tangential acceleration $\tilde{a}_t$, (c) gravity signal projected on X-axis g_x and (d) gravity signal projected on Y-axis g_y.

Figure (3-9) (a) and (b) shows the sensor outputs on the X- and Y-axis, which are calculated by replacing accelerations signals $\tilde{a}_c$, $\tilde{a}_t$, g_x and g_y into Equations (3-5) and (3-6) respectively. Next, these output signals are processed according to the tangential acceleration reconstruction method explained in Section 3.7.

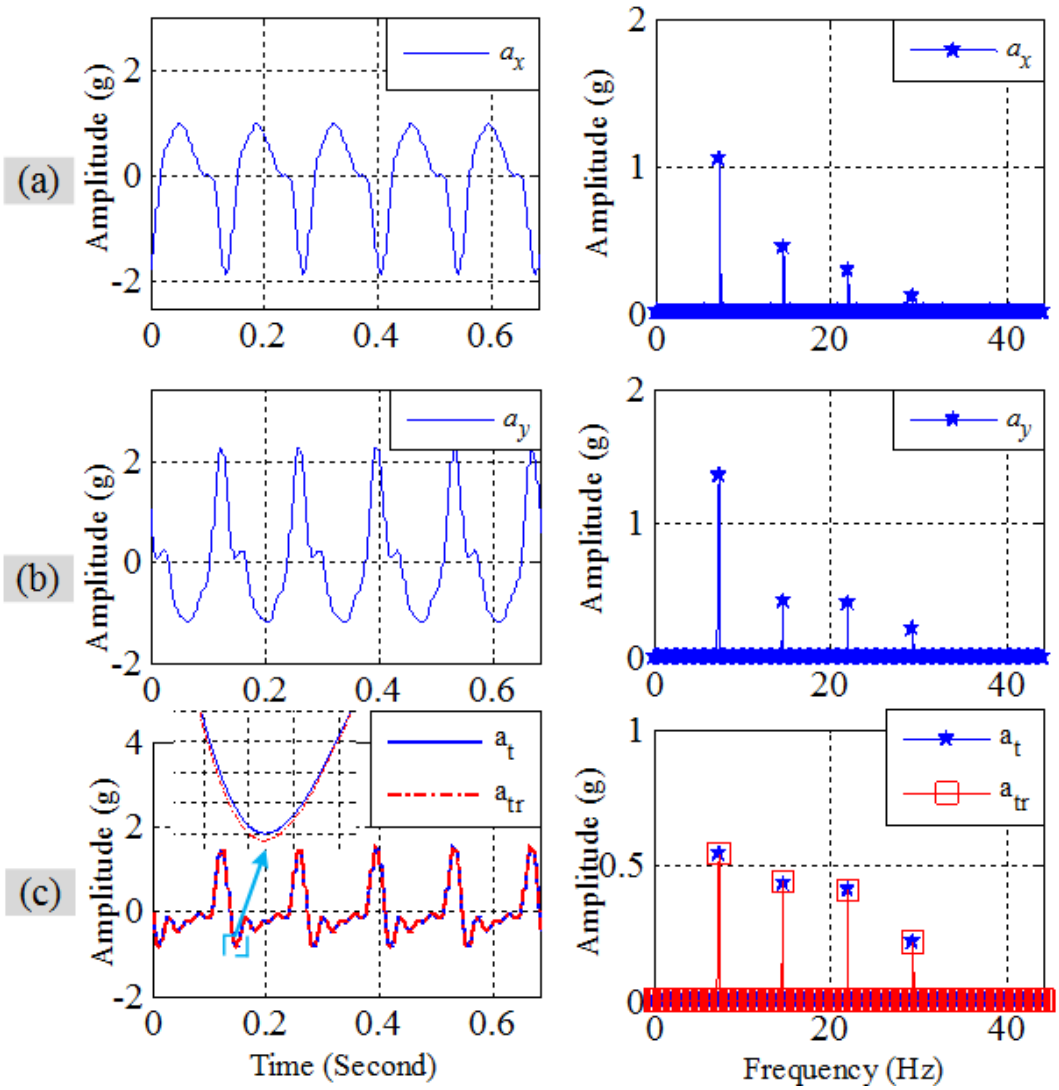

Figure 3-9 Processed signals and their spectrum (a) signal in X-axis $\tilde{a}_x$, (b) signal in Y-axis $\tilde{a}_y$ and (c) true tangential signal $\tilde{a}_t$ and the reconstructed signal $\tilde{a}_{tr}$

A contrast in the reconstructed tangential signal $\tilde{a}_{tr}$ and the real tangential acceleration $\tilde{a}_t$ are given in Figure (3-9c). It is clear that the two signals are almost identical and displays excellent equivalence in regards to the amplitude, waveform shape and frequency factors, which means that this method is reliable and can be used to eliminate gravitational acceleration, giving a pure tangential acceleration.

3.7.2 Error Analysis

The absolute error of the harmonics signals was calculated to estimate the performing capacity of one MEMS method used to remove the gravity signal projected on both X- and Y-axis,

providing true tangential accelerations. Table 3-2 compares the amplitudes of the true tangential accelerations $\tilde{a}_t$ and the reconstructed tangential accelerations $\tilde{a}_{tr}$ and also shows the absolute error of the first fourth harmonics [97].

Table 3-2 Absolute error of harmonics for one MEMS sensor method

	1st harmonic	2nd harmonic	3rd harmonic	4th harmonic
Amplitude of $\tilde{a}_t$ (g)	0.4918	0.3934	0.3687	0.1966
Amplitude of $\tilde{a}_{tr}$ (g)	0.4939	0.3974	0.3725	0.2002
Error (g)	-0.0020	-0.0040	-0.0037	-0.0037

The table shows very small the absolute errors among all harmonics of the reconstructed acceleration signals, at less than 4%. This level of absolute error can be acceptable, and they are close to the sensor resolution used in this research (for the detailed specification of the MEMS sensor see Chapter Four). In addition, the error distribution of one MEMS method is studied deeply under different rotor dynamic characteristics by performing a Monte-Carlo test based on the angular speed given in Equation (3-32). In this test, the harmonics amplitudes of $\tilde{\omega}$ are chosen as random values (ranges given in Table 3-3). However, they are restricted by an approximate relationship where $A_1 > A_2 > A_3 > A_4$. Additionally, the initial phase $\varphi_n \left(n = 1, 2, 3, 4\right)$ and the initial angular displacement θ_0 are made to be random values between 0 and 2π [97].

Table 3-3 Parameter ranges for the Monte-Carlo simulation.

Parameters	A_1	A_2	A_3	A_4	$\theta_0, \varphi_1, \varphi_2, \varphi_3, \varphi_4$
Uniform range	[10,20] rpm	[6,12] rpm	[3,8] rpm	[1,4] rpm	$\left[0 \sim 2\pi\right]$

The essence of such random inputs is that it is conducive to the generation of speed fluctuations thereby allowing the computation of corresponding errors. Table 3-4 shows the errors for the first four harmonics after 10,000 iterations. From these results, it is clear that even under severe situations, construction errors are very low in magnitude, suggesting that the construction method is a reliable one and can be used to obtain the tangential accelerations used for rotating machine condition monitoring [97].

Table 3-4 Error results of the Monte-Carlo test for one MEMS sensor method

	1st harmonic	2nd harmonic	3rd harmonic	4th harmonic
Lower error bound(g)	-0.0108	-0.0133	-0.0096	-0.0081
Upper error bound(g)	0.0082	0.0114	0.0102	0.0080
Error range(g)	0.0190	0.0247	0.0198	0.0161

3.8 Summary

Clearly, different technologies offer different benefits and present different drawbacks, as well as suiting different tasks when managing an asset, with no single technological solution currently available for all applications. Considering WSN applications, the most applicable standards are IEEE802.15.1 and IEEE802.15.4. Meanwhile, industrial machinery presents a harsh environment for WSNs, and the difficulties involved in this environment need to be taken into account when selecting the best data transmission approach.

One can efficiently reconstruct the tangential acceleration employing the orthogonal outputs obtained from the MEMS accelerometer. These signals depict favourable matching between the simulation results and that in the original tangential acceleration. Besides, from the error analysis, the proposed method presented in this chapter has a maximum error of 0.025, which is a very small value, making this method reliable and efficient.

CHAPTER 4 TEST RIG FACILITIES AND EXPERIMENTAL WORK

This chapter introduces the test rig used to carry out the investigation of using tangential responses of on-rotor MEMS. It begins with a brief description of the reciprocating compressor used in this research. Then, it explains the operation of the transducers and its measured parameters, as well as giving a description of the data acquisition system. Next, it presents the fault types and implementation.

4.1 Test Rig Description

As mentioned in Chapter Two, there are many types of compressor with different working principles and conditions. Among compressor types, the reciprocating compressor is one of the most common machines used in industry to compress and process gas for different applications. In this research, a two-stage, single-acting Broom Wade reciprocating compressor (Model TS9) was selected to be used for experimental work. Figure 4-1 shows the test rig, including the Broom Wade reciprocating compressor, sensors and data acquisition. The compressor basically includes three main components; an induction motor, a compressor unit and a high pressure receiver used for storing compressed air.

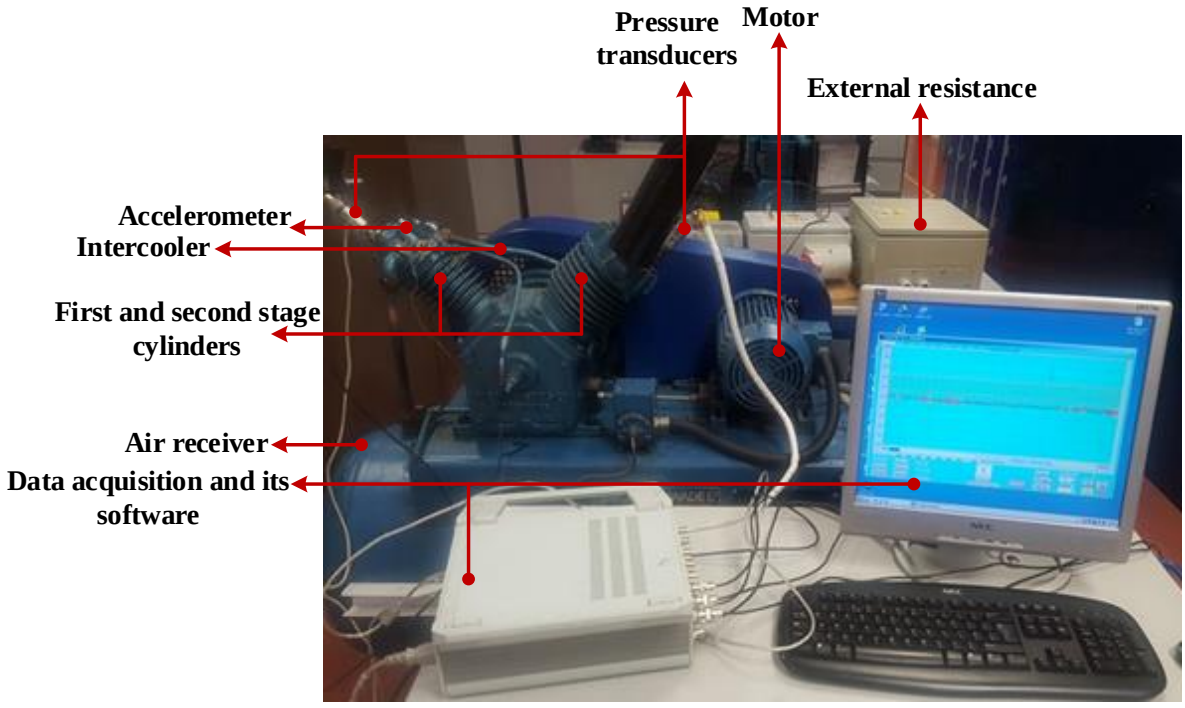

Figure 4-1 Broom-Wade TS9 RC

A 3-phase induction motor (KX-C184) with a power capacity and full speed rating of 2.5kW and 1420 rpm, respectively, drives the reciprocating compressor. A belt-pulley arrangement, having transmission ratio 3.2:1, is employed to transfer power from the motor to the flywheel. With the above motor ratings, the flywheel attains a speed rating of approximately 440 rpm through a corresponding motor speed reduction by a factor of 1/3.2. Figure 4-2 shows a

schematic diagram of the used two-stage reciprocating compressor and Table 4-1 lists the technical specifications of the induction motor and the compressor.

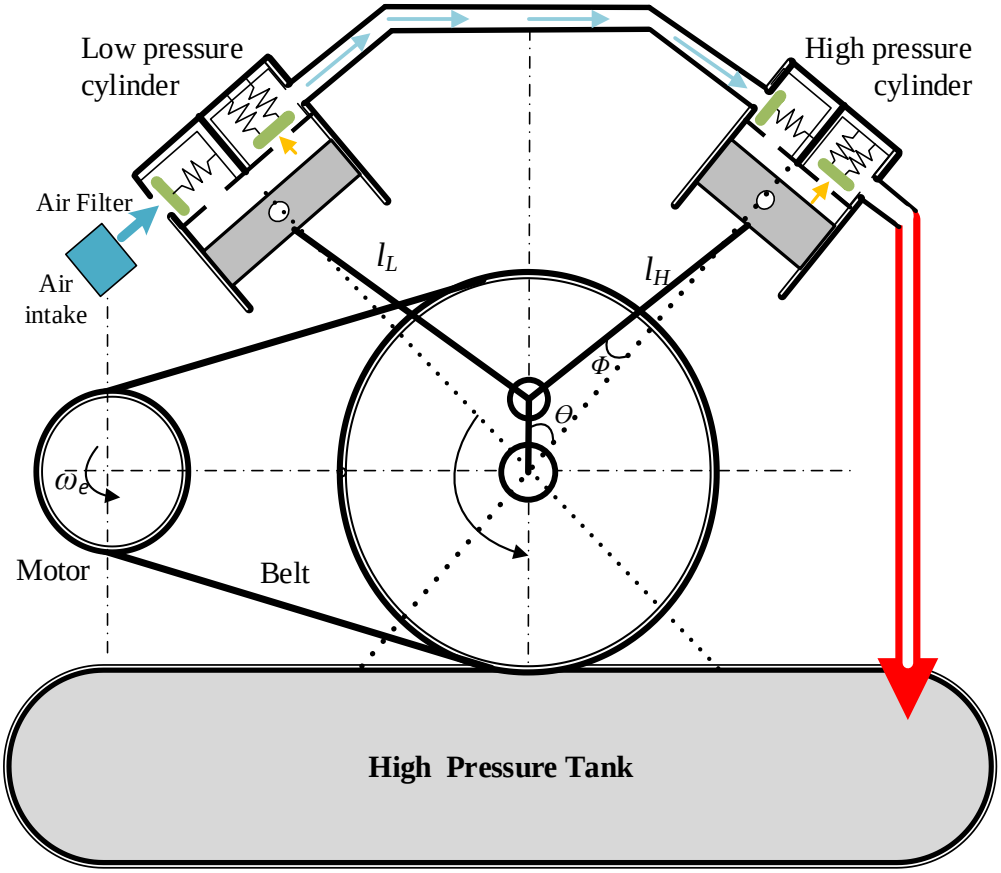

Figure 4-2 Schematic diagram of a two-stage reciprocating compressor [45]

To obtain high-pressure air, intake air is filtered to make sure that it is sufficiently smooth and dry, and only enters the compressor after this. The compressor first of all compresses the air in the first pressure cylinder (low stage) and then this air passes into the intercooler before going through the second pressure cylinder (high stage). Thereafter, the compressed air is ejected from the second cylinder to the storage tank, which has a safety valve fitted to prevent the air pressure exceeding a specific pressure value. The compressor is designed to deliver air at pressures between 0.55 MPa (around 80 psi) and 0.83 MPa (around 120psi) to the air storage unit that has a maximum limit of working pressure at around 1.38MPa (200 psi).

Table 4-1 Specifications of the motor and the Broom Wade TS9 reciprocating compressor.

Motor specifications	
Motor power	2.5/3 HP
Current	4.1/4.8 A
Voltage	380/420 V
Motor Speed	1420 rpm
Broom Wade TS9 Compressor Model specifications	
Number of cylinders	2 (90° opposed)
Piston Diameter [Low Pressure Cylinder]	93.6 mm
Piston Diameter [High Pressure Cylinder]	55.6 mm
Piston stroke	76 mm
Max working pressure	1.38 MPa
Speed	440 rpm

4.2 Measurement Transducers

The test rig used in this study has been used for many condition monitoring research projects conducted by the Centre of Efficiency and Performance Engineering (CEPE) group. Thus, a number of transducers have been already installed, including accelerometers, an instantaneous angular speed (IAS) encoder, static and dynamic pressure sensors and thermocouples. Each of these transducers is linked to a data acquisition system (DAQ) by coaxial BNC cables for reducing signal noise. Besides these, two different MEMS accelerometers have been added in this work. Below is a description of these transducers.

4.2.1 Encoder

A typical and precise way of measuring IAS is through installing an optical encoder at one end of the rotor by determining the angular position of the shaft. As shown in Figure 4-3, an incremental shaft encoder RI32 was installed on the flywheel end to measure the IAS with an accuracy of 1^{o}, allowing any small changes in shaft speed to be measured and recorded. The encoder provides two outputs: the first on is 100 electrical pulse trains for every revolution and the other signal is one pulse for each revolution, known as the index signal. It is connected directly to the DAQ.

Figure 4-3 RI32 encoder sensor

Figure 4-4 shows the online raw data, the electrical pulse trains and the index signal, measured by the encoder and presented through data acquisition software.

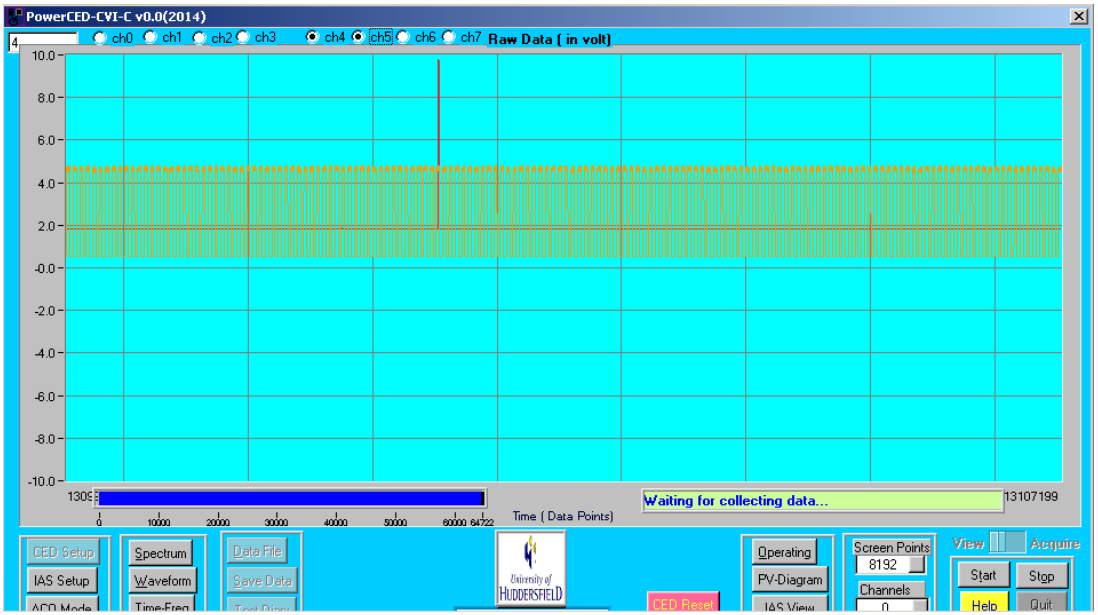

Figure 4-4 Optical encoder raw data

4.2.2 Dynamic Pressure Sensor

Two analogue pressure transducers are placed on the head of low and high pressure cylinders to measure dynamic pressure change. As shown in Figure 4-5, both GEMS type 2200 strain gauge pressure transducers were fixed via a small hole drilled into the head of each cylinder.

These sensors can measure the pressure with a range of up to approximately 4MPa (600psi), and the upper frequency limit of round 4 kHz. Figure 4-6 shows a typical set of online raw data sensed by the dynamic pressure sensors at both low and high stage cylinders.

Figure 4-5 Dynamic pressure sensor on cylinder head

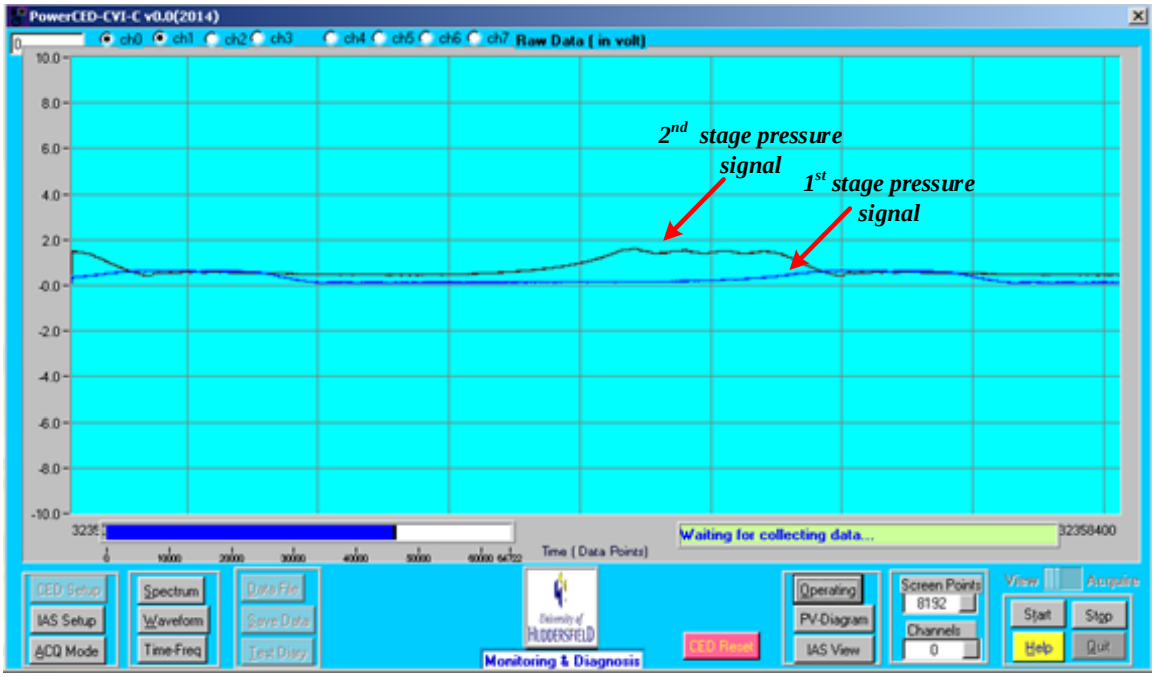

Figure 4-6 Online pressure sensors raw data

4.2.3 Static Pressure Sensor

Figure 4-7 shows a Gem type PS20000 static sensor pressure, which has an operating range of 0 to 1.35MP, installed on the storage tank to monitor its pressure as well as to trigger data collection when the pressure reaches the specified values. The maximum output of the sensor

is about 100mV, the supply voltage is 15V (10V), the operating pressure range is between 0 and 1.35MPa and the operating temperature range is quite wide, ranging from -20°C to + 105°C. Figure 4-8 displays the online raw data of the pressure at the tank sensed by the static pressure sensor.

Figure 4-7 Static pressure sensor on air storage tank

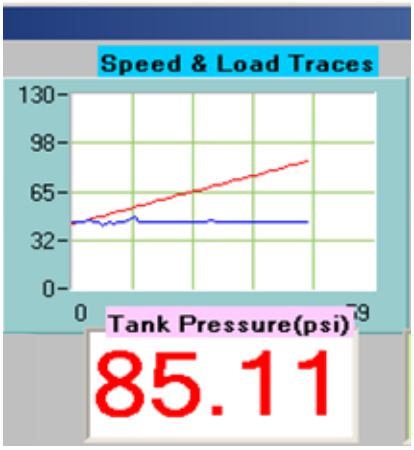

Figure 4-8 Tank pressure sensor output

4.2.4 Temperature Measurement

To measure the air temperature inside both low and high pressure cylinders, K-type thermocouples with a linear response from -20°C to 220°C were inserted into the inside of the cylinders through holes created in each stage. Figure 4-9 shows the temperature sensor installation, while the online thermocouples' sensor outputs were presented in Figure 4-10. The cylinder temperature measurement is very important not only to protect the other sensors from high temperatures, but also to ensure the safe operating conditions of the reciprocating compressor.

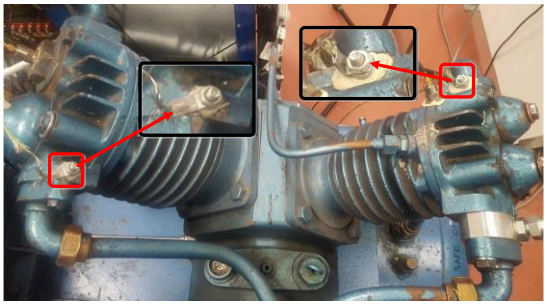

Figure 4-9 Temperature sensor installation

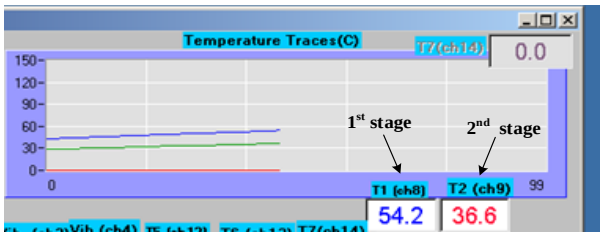

Figure 4-10 Online thermocouple digital output

4.2.5 AX3 Data Logger

Figure 4-11 presents an image of a three axial MEMS acceleration data logger, AX3, constructed based on ADXL345 and manufactured by Axivity [155].

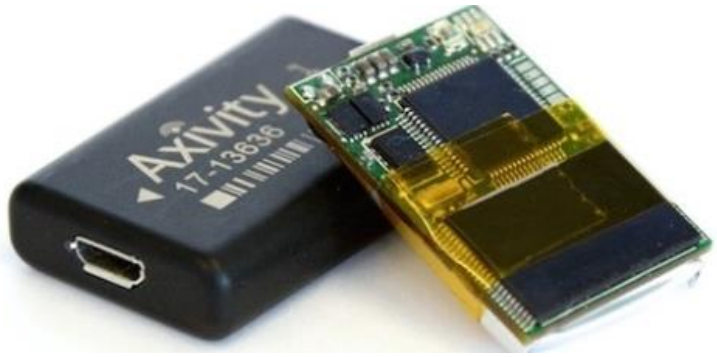

Figure 4-11 AX3 accelerometer

As shown in Figure 4-12, the AX3 is attached to be closer to the flywheel centre to acquire the on-rotor acceleration signals. The AX3 sensor is located with an offset of 5 cm from the flywheel centre allowing the data logger dynamic range to capture the full waveform of the acceleration signals. The specifications for the AX3 data logger are listed in Table 4-2. Before using the AX3, it was set for operation within a ±16g dynamic range at a 1600 Hz sampling rate. The collected information is stored in the memory integrated with AX3 during the machine run-time and then transferred to a computer for post-processing of the results after the shutting down of the machine.

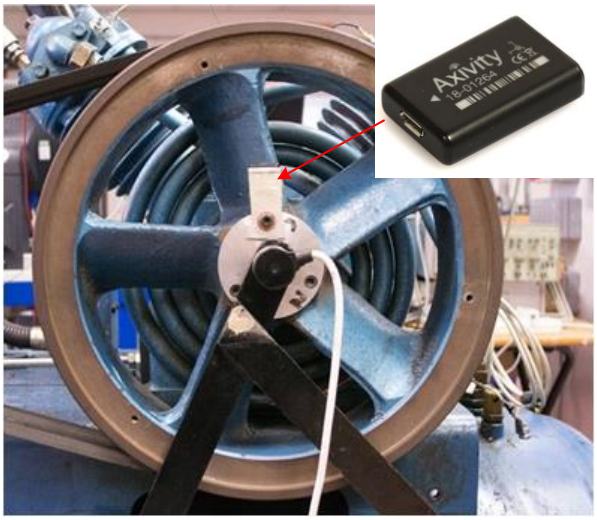

Figure 4-12 Picture of AX3 installation on the compressor wheel

Table 4-2 AX3 features

Parameters	**AX3**
Cost	£99
Sensor Type	MEMS
Axis	3-axis accelerometer
Range	±2/4/8/16g (Configurable)
Size & weight	23x32.5x7.6 mm, 11g
Resolution	Configurable up to 13 bit (0.0039g/LSB)
Logging Frequencies	Configurable 12.5Hz - 3200Hz
Maximum Logging Periods	30 days at 12.5 Hz or 14 days at 100Hz
Battery Type	Rechargeable
Connectivity	Micro USB
Data collection method	Data logger device (512MB NAND flash memory)
Another sensors build in	Temperature and Light sensors

A typical set of AX3 raw data that presents the rotating acceleration is shown in Figure 4-13. AX3 data was presented and downloaded though OM software that provides a GUI interface. More details about AX3 configuration, data collection downloading and data format converting can be found in Appendix A.

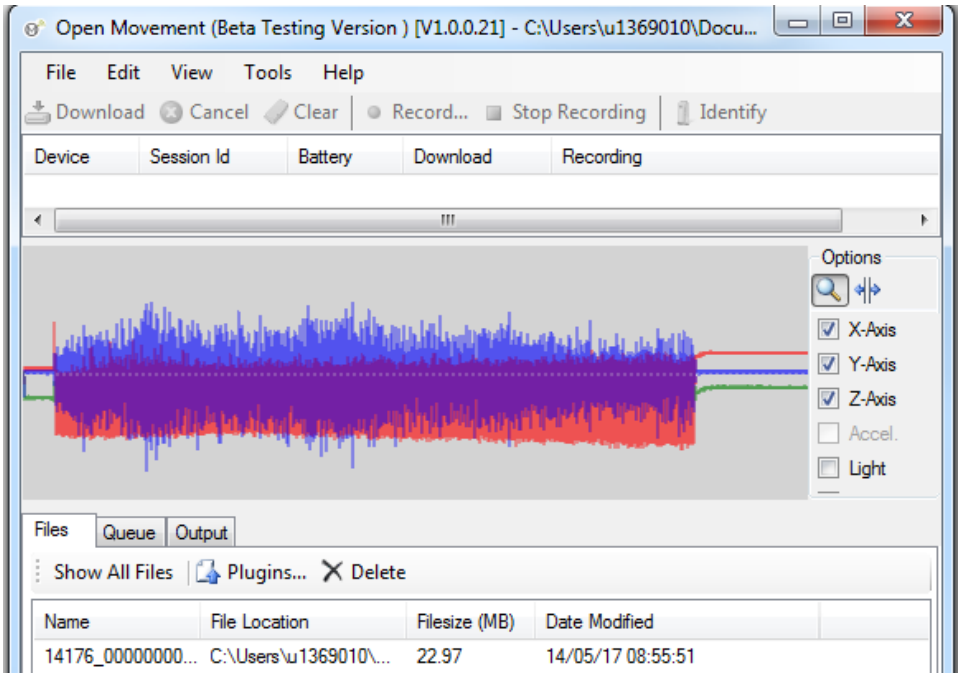

Figure 4-13 Ax3 raw data

4.2.6 Wireless Sensor Node

Figure 4-14 depicts the wireless sensor node adhered directly to the flywheel to measure the on-rotor acceleration. The Analogue Device ADXL345 3-axis accelerometer has been used in this research. It is widely used in industrial instrumentation, personal navigation devices and medical instrumentation [156]. The ADXL345 MEMS sensor has a high resolution, of up to 13-bit $(3.9mg / LSB)$ and it is also able to measure both static acceleration of gravity and dynamic acceleration caused by motion at up to $\pm 16g$. a DC supply voltage range is needed to power the sensor between 2V and 3.6V. Table 4-3 shows the specification of the ADXL345 accelerometer.

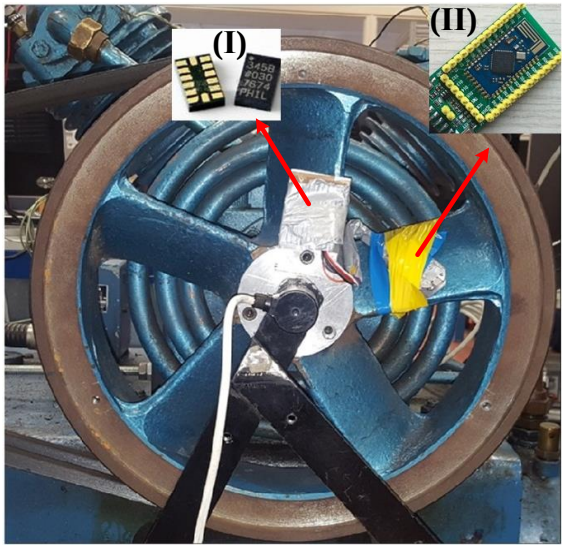

Figure 4-14 Installation of (I) MEMS accelerometer and (II) microcontroller board

Table 4-3 specification of the ADXL345

Parameters	**ADXL345**
Cost	Around £10
Sensor Type	MEMS
Axis	3-axis accelerometer
Range	±2/4/8/16g (Configurable)
Size & weight	3x5x1 mm, 30mg
Resolution	Configurable up to 13 bit (0.0039g/LSB)
Digital interfaces	SPI and I^2C
Temperature range	-40^oC to $+85^oC$

4.3 Data Acquisition System

Figure 4-15 shows a high-performance CED 1401 Plus data acquisition system from Cambridge Electronic Design which was used to acquire the data from all sensors installed on the reciprocating compressor except for the Ax3 data logger and wireless MEMS accelerometer. During experiments, this electronic device collects, analyzes and converts the sensor analogue signals to a digital data in which a further analysis can be achieved via Matlab Program. For all experimental tests, the data was acquired from all sensors regardless of whether it would be used or not, as this did not change the file data, making processing easier. In each test and for the transducers connected to CED 1401 Plus, two data files implemented in binary format were collected at every specific load used for post analysis. Simultaneously, the data recorded by the AX3 sensor is saved in the memory for the period of machine running-time in csv format and then transferred for post-processing, while the data measured by wireless sensor was sent instantly to a remote computer that received the data in mat format through BLE. Different acquired data was used as inputs for further processing and was been analyzed through programming using Matlab software.

Figure 4-15 CED 1401 Plus data acquisition system

The main features of the CED 1401 Plus data acquisition device are listed below:

- It has 16 channels (only seven channels are used in this study).
- It has one G byte memory, expandable to two G bytes.
- It can record waveform data and marker information at 400 kHz and 16 bit resolution.
- It is a multi-tasking experimental system.
- It can generate waveform and digital outputs simultaneously in real-time.

As listed in Table 4-4, only seven channels are used in this experimental research to collect different data using the transducers described earlier.

Table 4-4 CED 1401 Plus channel

Channel number	Data type
Channel one	Collects the data from low pressure transducer
Channel two	Collects the data from the high pressure transducer
Channel three	Collects the data from the low vibration accelerometer
Channel four	Collects the data from high vibration accelerometers
Channel five	Collects the data from shaft encoder
Channel six	Collects the data to measure angular position mark for position TDC piston
Channel Seven	Collects motor current signals

4.4 Measurement Practice, Data Management and Software for Data Processing

A schematic diagram of the compressor test rig system including the various measurement positions, transducers, and data acquisition system used in this study is presented in Figure 4-16.

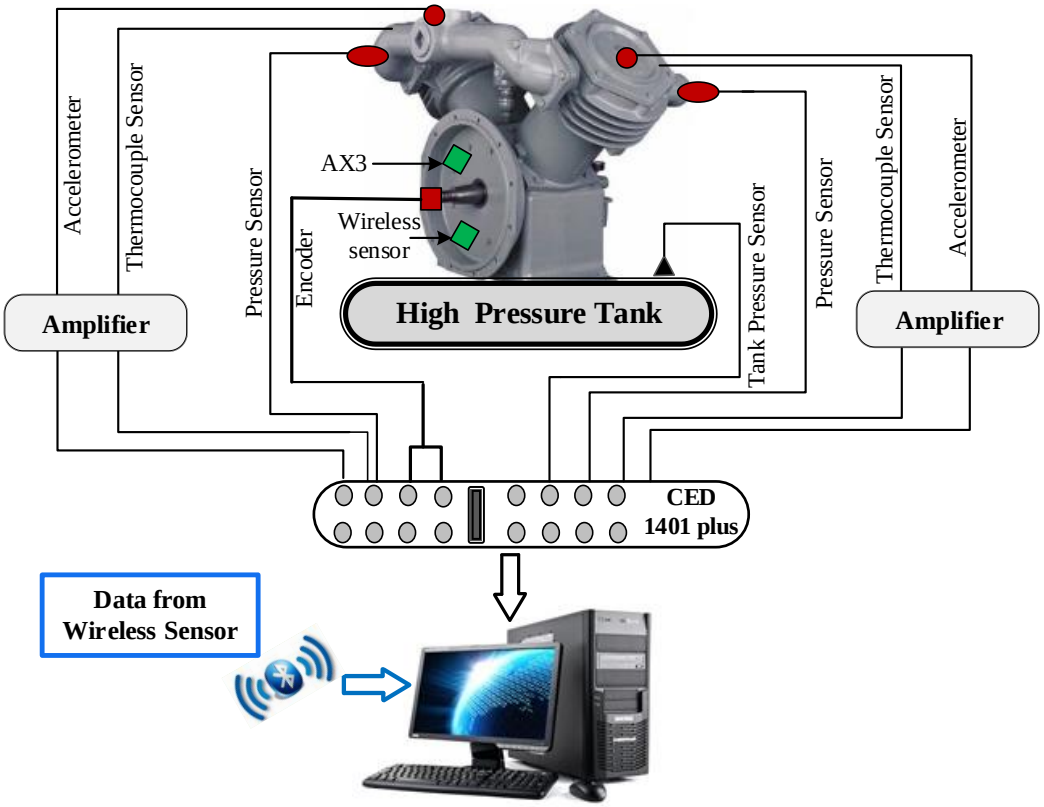

Figure 4-16 Schematic diagram of the compressor test system

The software for data acquisition was written using LabWindows/CVI, which is a software development environment for C programmers. The software is pre-installed with numerous facilities like exhaustive run-time libraries that manages controlling of instruments, efficient data acquisition capacity, functional analysis as well as an easy GUI (Graphical User Interface) (GUI) compiler having an added engineering UI (User Interface) functionality. This programme finds extensive use in creating high performing and stable applications that is utilised by diverse field of professions such as in military, manufacturing and aerospace industry, telecommunication services, automotive facilities, to name a few. It enables the static and dynamic parameters of data such as vibration, pressure, IAS, acceleration, and temperature to be measured and recorded regularly and simultaneously at different rates and data lengths.

The software also has a set-up window allowing users to modify some parameters, such as the sampling rate and data length. As shown in Figure 4-17, the sampling frequency and data length were set to 39.68 KHz and 64722 points respectively. Therefore, the time duration of data points was 1.631 sec.

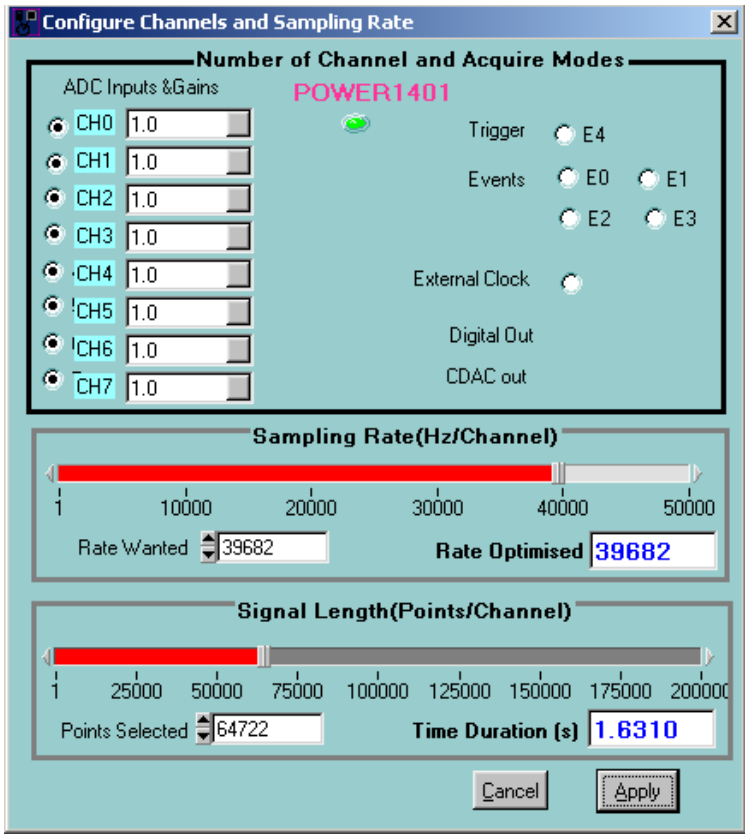

Figure 4-17 Set up window of data acquisition software

Parameters such as the reciprocating compressor temperature, vibration levels on the low and high pressure cylinders, current signal and rotor speed have been observed and their data is recorded in regular intervals from the experimental setup of reciprocating system. The raw data that is acquired on each run gets displayed on a computer-aided monitor (illustrated in Figure 4-18).

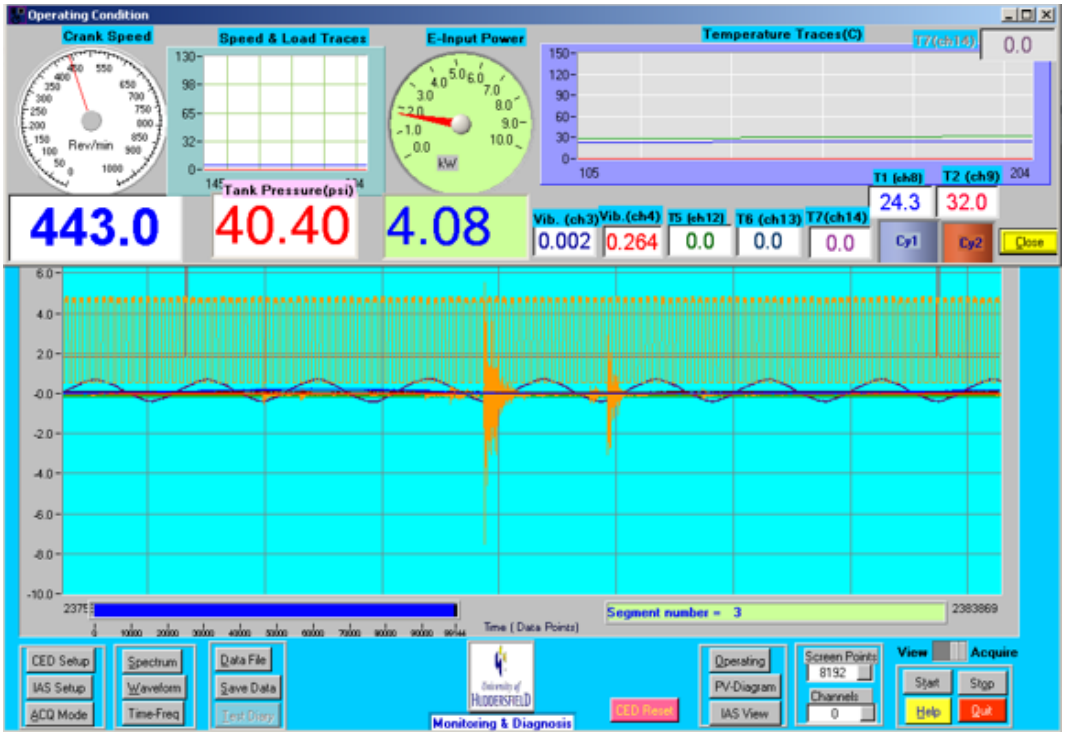

Figure 4-18 Raw data acquired from test rig

4.5 Fault Simulation and Seeding

In this work, many measurements were obtained for different faults, including intercooler leakage (IL), second stage discharge valve leakage on the high pressure cylinder (VL) and asymmetric stator winding of the motor driver (ASW), which were simulated individually on the compressor test rig. Table 4-5 summarizes the experimental tests conducted to monitor the performance of the compressor with only one individual, isolated fault present as well as combined faults.

Table 4-5 Test cases description

Test case	Description
BL	Healthy data
DVL	Data with a leaky discharge valve on the high pressure cylinder
ICL	Intercooler leakage
ICL+DVL	Large intercooler leakage + a leaky discharge valve on the high pressure cylinder
DVL+ASW	a leakage in2nd stage discharge valve + asymmetric stator winding of the motor
ICL+ ASW	Intercooler leakage + asymmetric stator winding of the motor

4.5.1 Leaky Valve Simulation

Among various pivotal components necessary for a reciprocating compressor, valves hold a significant centre-stage. Reciprocating compressors can be designed with different types of valves, including poppet valves, ring valves and plate valves [157], which are used in the reciprocating compressor used in this work. As shown in Figure 4-19, plate valves were constructed from a seat, valve plate, springs, and guard. It is recommended for use when the required discharge pressure is up to 40 MPa. This kind of valve is capable of handling high pressures around 20 MPa, differential pressures up to 40 MPa, speeds up to 1800 rpm, and temperatures to 500°F.

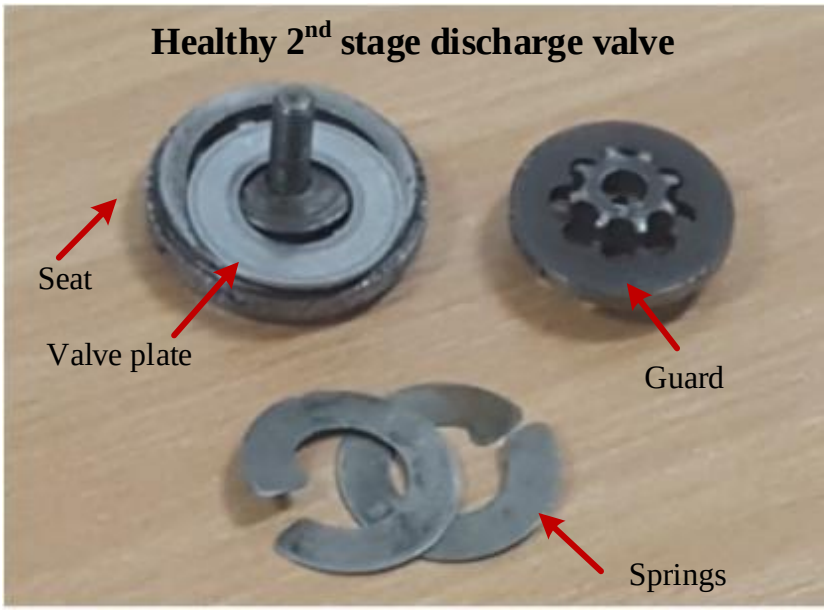

Figure 4-19 2nd stage discharge valve parts

Valve leakages can be considered one of the most common failures in reciprocating compressors. As illustrated in Figure 4-20, this fault was produced by producing a hole of 2 mm in diameter on the discharge valve plate, taking up around 2% of the flow cross-section.

Figure 4-20 Leak in 2nd stage discharge valve plate

4.5.2 Leak in Intercooler

Another common leak of the reciprocating compressor appears in the joints in the piping used to carry the processed air from low to high stage pressure. In this work and as shown in Figure 4-21, intercooler leakages are implemented by loosening the intercooler with two kinds of severities. A small intercooler leakage was produced by turning the nut through one turn, whereas loss of a larger amount of air was created to implement a large intercooler leakage.

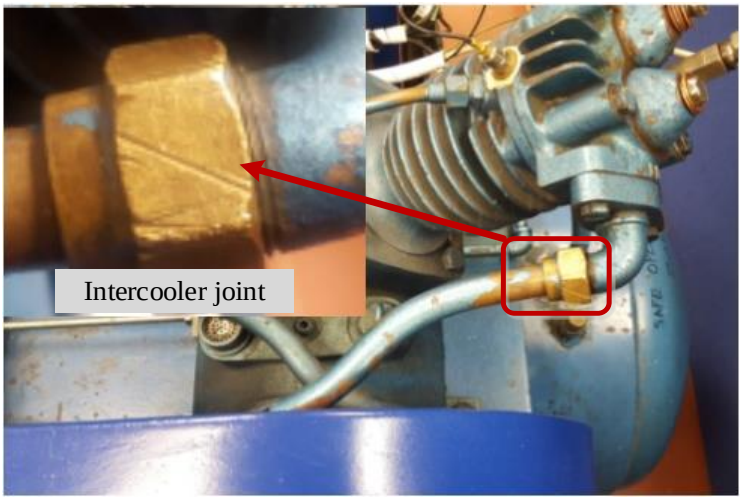

Figure 4-21 Leak in the intercooler

4.5.3 Stator Asymmetries Faults

A 2.5 kW, 445 rpm 3-phase induction motor with a phase resistance of 10 Ω was used to drive the compressor. Generally, three phase induction motors may have different faults due to poor connections, overloading and overheating. Turn to turn faults, phase to phase short faults, phase to earth short faults and open circuit coil faults [17] are the most common faults appearing in the induction motor.

Figure 4-22 presents the external resistor bank connected to only one phase resistance of the induction motor to simulate motor stator resistance imbalance, whereas the electric scheme is shown in Figure 4-23. Any small change in the phase resistance value will cause a variation of the current flowing in the three phases as well as reducing the magnetic flux exuded by one of the stator windings, leading to degradation of system performance. Besides, any small amount of induction motor imbalance resistance will significantly increase the temperature of the stator winding, leading to degradation in motor performance.

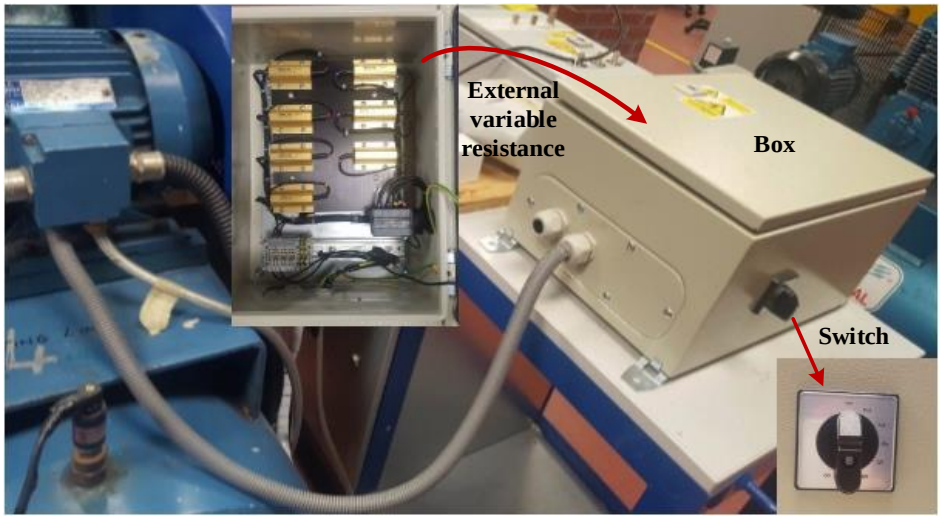

Figure 4-22 External resistor bank

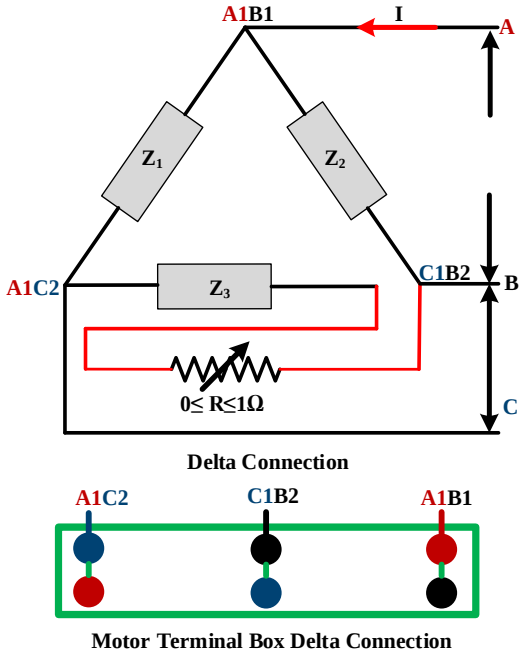

Figure 4-23 Schematic diagram of extrenal resistance connection

All faults and leakages explained in this section can degrade the compressor efficiency. As shown in Figure 4-24, reciprocating compressor performance is implemented by compression time, which can be defined as the time required for the pressure in the tank to reach 0.816MPa (120psi).

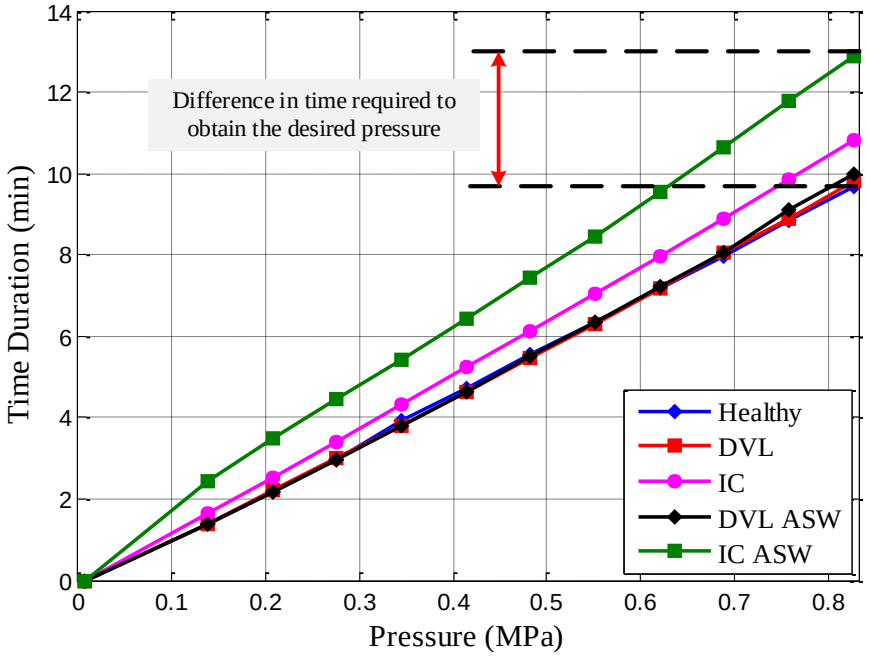

Figure 4-24 The effect of different fault conditions on compressor performance

From this figure, it is clear that the compression time is longer when there is a fault compared with the healthy condition case, which means the compressor takes more time to reach a specific pressure value, resulting in consuming more power.

4.6 Summary

In this chapter, a detailed description of the test facility was provided, and relevant instrumentations used to acquire different parameters such as vibration, IAS, pressure, and temperature were included. Besides this, the data collection using the test rig was explained, to be analysed using MATLAB code to monitor the reciprocating compressor health and indicate common faults.

CHAPTER 5 MONITORING RC USING THE ACCELERATION RESPONSES IN TANGENTIAL DIRECTION OF THE ON-ROTOR SENSOR

In this chapter, data acquired by AX3 installed on the reciprocating compressor (RC) flywheel is analyzed to classify faulty signals. Experimental findings prove that tangential accelerations measured at the RC crankshaft can well reflect RC health and common faults to be differentiated for online condition monitoring.

5.1 Introduction

The observations in Chapter Three showed that the actual tangential acceleration can be obtained by combining two orthogonal outputs coming from the accelerometer, which measure the centripetal acceleration and tangential acceleration combined with gravitational acceleration projected on both X-coordinate and Y- coordinate. Therefore, the rotor dynamics of a rotor can be characterized precisely using reconstructed tangential acceleration, providing accurate information for condition monitoring.

In order to estimate performance of use of the reconstructed signals for rotating machines condition monitoring, experiments was carried out based on the two-stage reciprocating compressor mentioned in Chapter Four.

5.2 Test Procedure

For the testing period, AX3 was set for operation within a ±16g dynamic range at a 1600 Hz sampling rate. This enabled the characteristics of the dynamic rotor to be inspected adequately. As discussed in the previous chapter, the mounting of the AX3 occurs directly onto the flywheel, at 50 mm offset from the centre. Measurements were also taken for tank pressure, and data for this was collected using a CED 1401 system at a 49019 Hz sampling rate. Overall 4 datasets were taken across a range of conditions for the compressor, using healthy state as the baseline and investigating 4 conditions of fault. These faults were produced when the reciprocating compressor was induced with different common compressor faults. The measurements were taken for a small intercooler leakage, a large intercooler leakage, a valve leakage towards the high-pressure cylinder and a combined fault simulated by creating a discharge valve leakage fault and intercooler leakage at the same time.

5.3 Results and Discussion

Figure 5-1 displays the rotating acceleration signals in three axes (X, Y, Z), which were measured by AX3 sensor at 100 psi (around 0.689 MPa). As explained in Chapter Three, the true tangential acceleration can be reconstructed using both signals measured at the X-axis and Y-axis of MEMS accelerometer, and so attention will be given to these outputs.

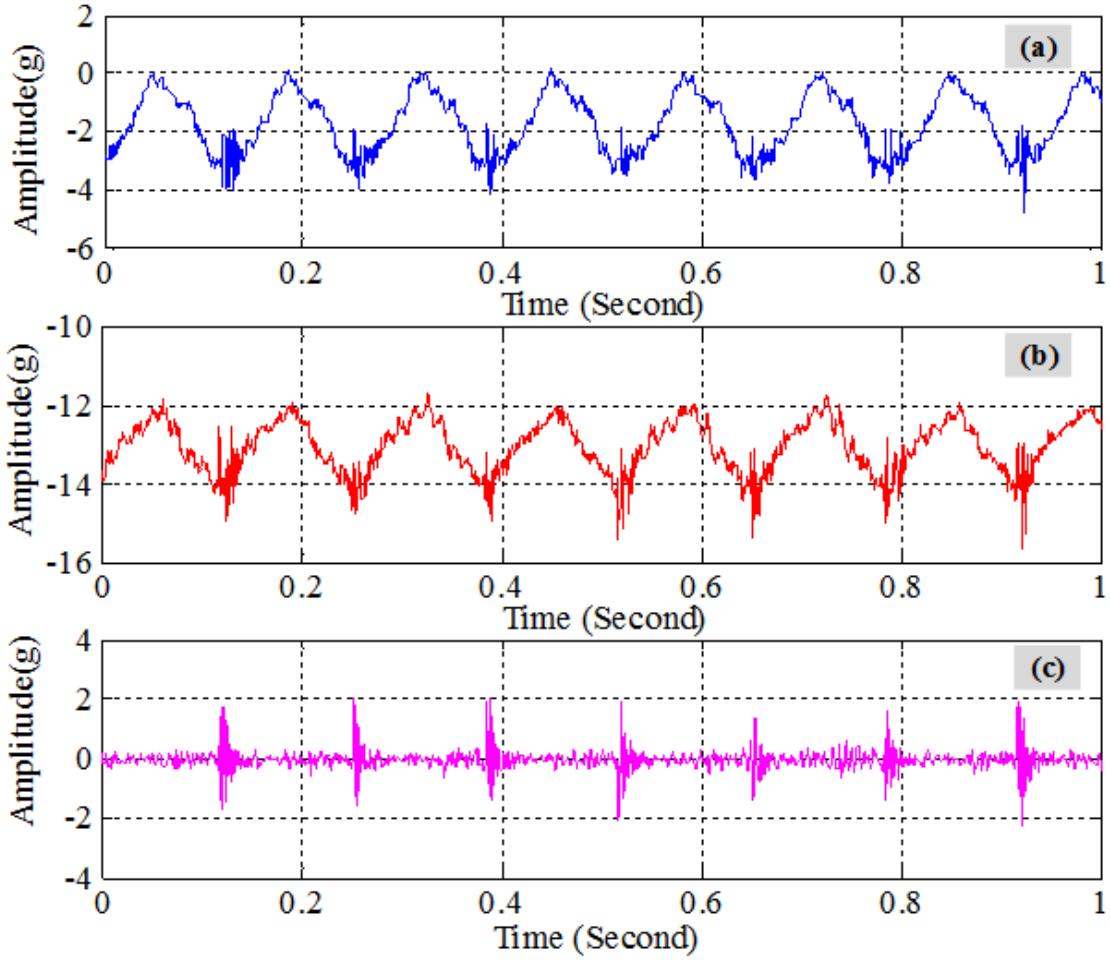

Figure 5-1 Acceleration signal at 100 psi pressure (a) *X* axial (b) *Y* axial (c) *Z* axes

It depicts that the acceleration signals on the X-coordinate and Y-coordinate shows periodic oscillations based on the working frequency, showing the basic dynamics of the compressor operation process. Nevertheless, due to centripetal acceleration a unique negative offset that is observed in Y-axis. Moreover, there was some negative offset observed on the X-axis, but this was not significant, and represented a projection from centripetal acceleration because of the lack of precise alignment between the sensor and the rotating track's tangential direction. However, such DC offsets are not essential for dynamic analysis due to there being no time varying information that can be used for condition monitoring.

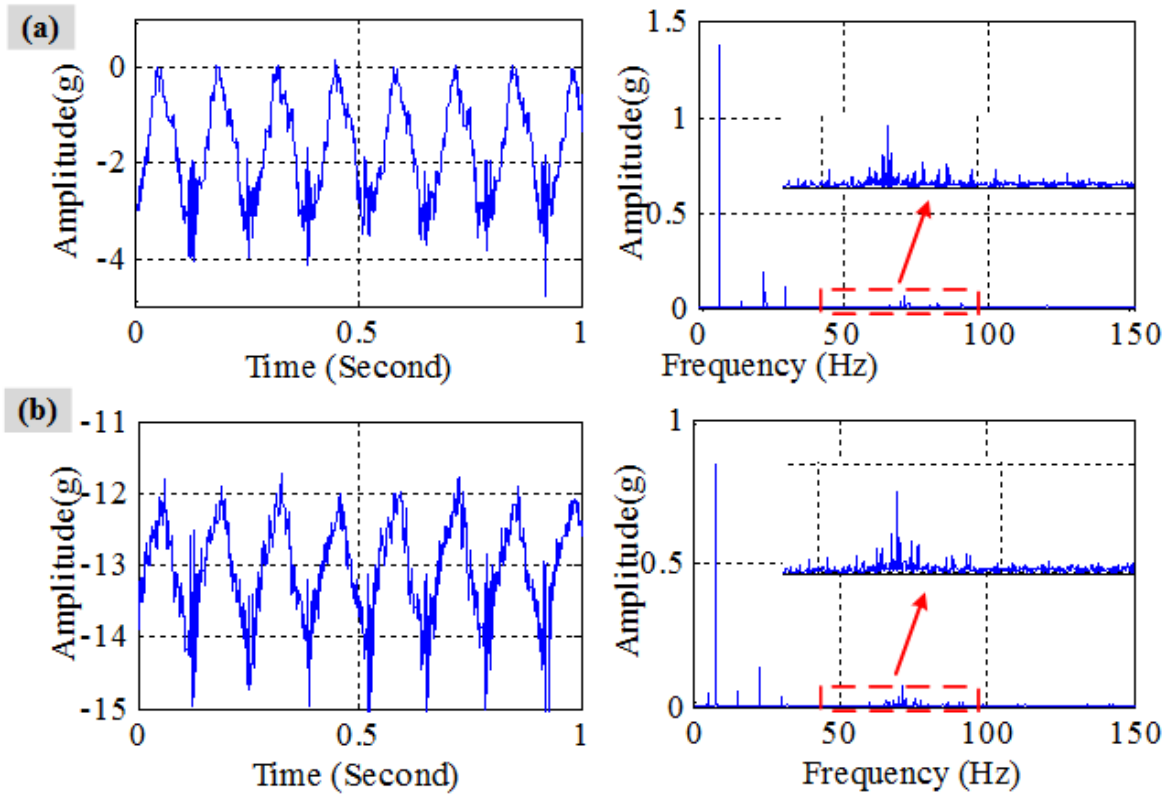

Figure 5-2 Acceleration signal and its spectra with pressure at 0.689MPa (100 psi) (a) X-axis and (b) Y-axis

In the meantime, the spectra in Figure 5-2 evidently depicts that for both signals the largest frequency component is at 7.54 Hz which is the steady angular speed for the crankshaft and is considered the fundamental frequency aforementioned. Besides this, at least four higher harmonics exist that are significant in showing more detail in compressor dynamics. Also, some higher frequency contents can be observed above 50Hz, which are from structural vibrations and not essential for analysis. After removing these components with a low pass filter, the tangential acceleration is reconstructed using the proposed methodology introduced in Chapter Three. Figure 5-3 presents the tangential acceleration signals, which are mainly constructed of the fundamental frequency and its first three harmonic components. By comparing the amplitudes of these components, it can be seen that the fundamental frequency has the largest amplitude and that the 3rd harmonic is larger than the 2nd and 4th components.

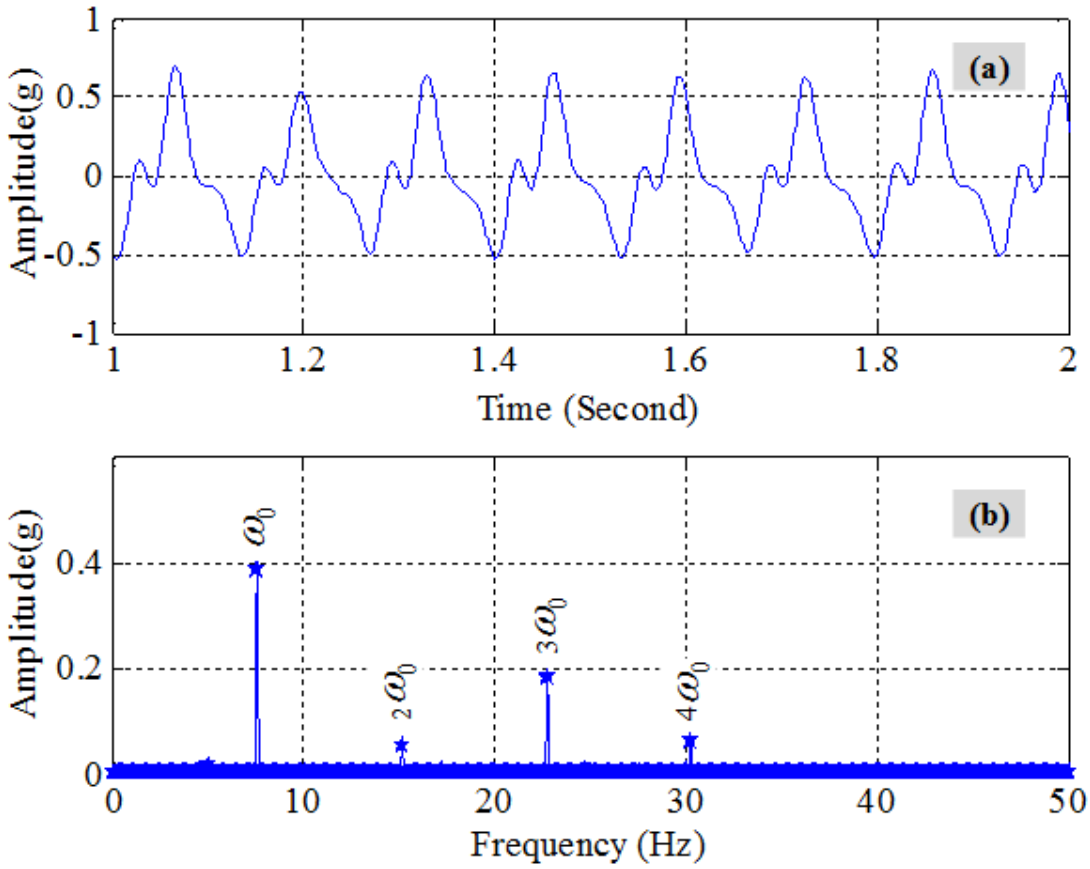

Figure 5-3 Reconstructed signals having 0.689MPa or 80 psi as tank pressure. (a) Temporal domain and (b) frequency domain

Moreover, the reconstructed signals for different tank pressures shown in Figure 5-4 is plotted to obtain the general features of reciprocating compressor dynamics. It is noticeable that the fundamental frequency, the 3rd and 4th harmonics components demonstrate linear relationships with the pressures for the whole pressure range, representing the effect of pressure-induced torque. On the other hand, the 2nd harmonic displays a non-linear connection with the pressure reflecting more on the impact of the torque caused by the inertia of reciprocating mass. Furthermore, the fundamental frequency and the 3rd harmonic exhibit comparatively higher amplitudes and can differentiate each successive pressure. These mean that they have a good signal to noise ratio (S/N) and sufficient accuracy to show the variation in pressure. Therefore, they are reliable for reflecting the dynamics of the compressors.

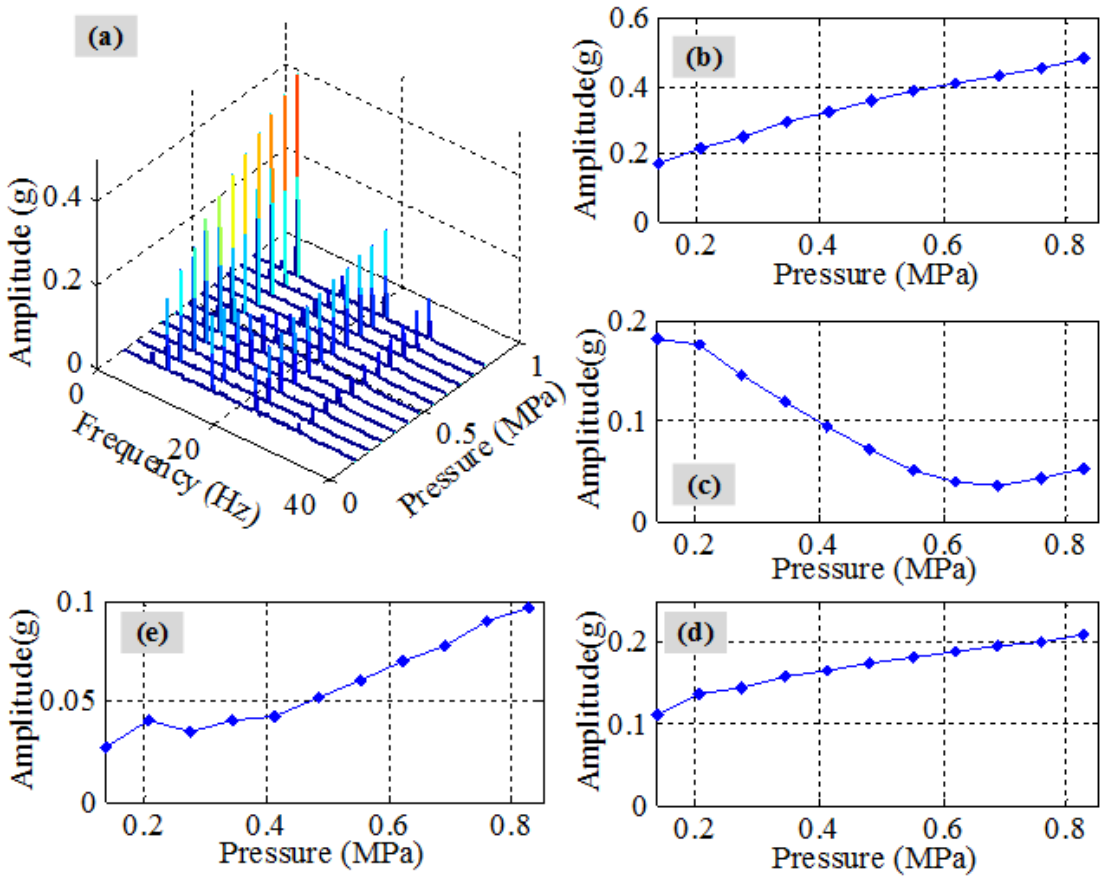

Figure 5-4 Tangential acceleration at conditions of tank pressure in spectral feature modes (a) as a waterfall-plot; amplitude of (b) fundamental component, (c) 2nd harmonic, (d) 3rd harmonic and (e) 4th harmonic.

For further evaluation of the usage of the reconstructed signal based on the method proposed in Chapter Three, more data were acquired when the reciprocating compressor was induced with different common compressor faults. These measurements were for small intercooler leakage, large intercooler leakage, valve leakage on the high-pressure cylinder and a combined fault simulated by creating a discharge valve leakage and intercooler leakage fault at the same time. The simulation methods for all these faults was explained in Chapter Four. The amplitude of harmonics of all acquired signals changing with compressor tank pressure is shown in Figure 5-5.

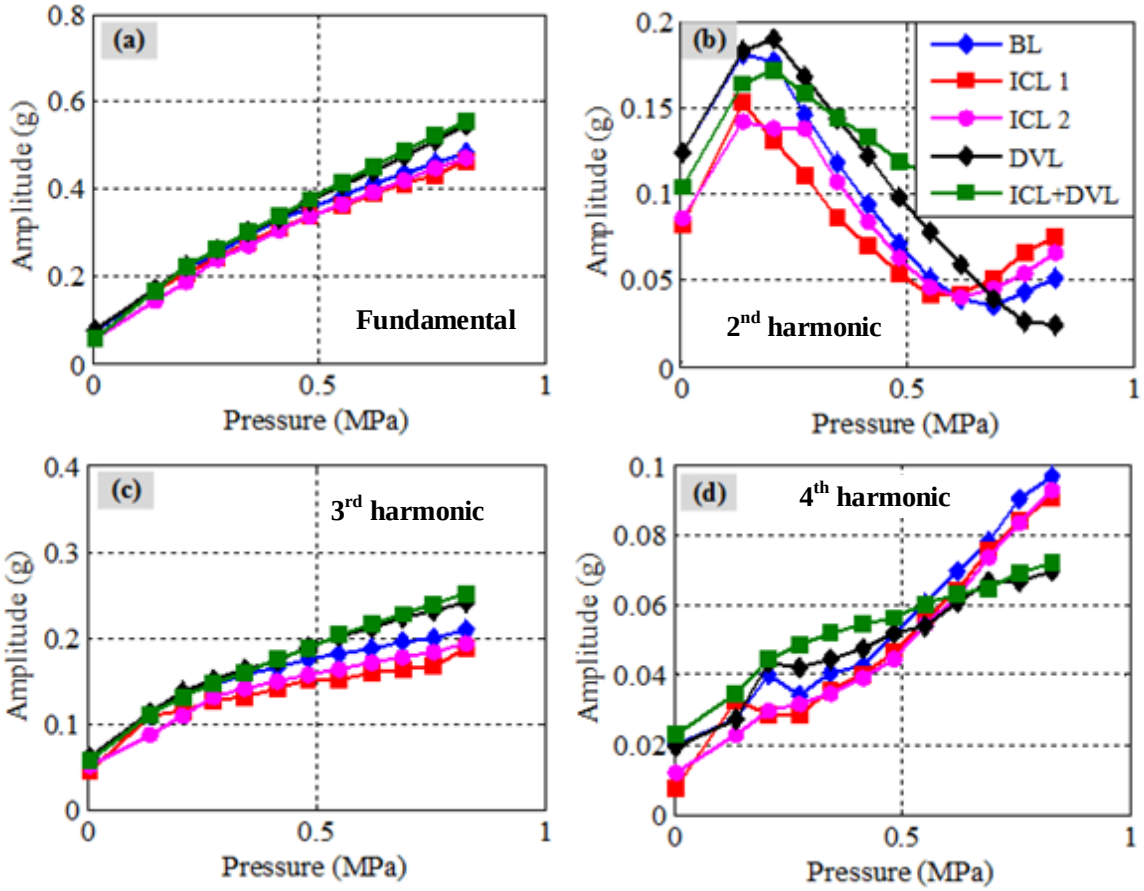

Figure 5-5 Amplitude corresponding to (a) fundamental frequency; (b) 2nd harmonic; (c) 3rd harmonic and (d) 4th harmonic of the reconstructed acceleration signal plotted against the tank pressure

Figure 5-6 illustrates the relation between the 3rd harmonic and the fundamental frequency with tank pressure across a range between 0.41 MPa and 0.83 MPa (60 psi to 120 psi). Based on the fundamental and the 3rd harmonic, the fault signals are classified in Figure 5-7. It is clear that the small intercooler fault (ICL1), the large intercooler fault (ICL2), the discharge valve leakage fault (DVL) and combined faults (ICL+ DVL) can be clearly separated from the baseline signal (BL). Furthermore, the residual of the DVL related faults, i.e. DVL and the combined fault (ICL+DVL), is positive, whereas that of ICL related faults, i.e. ICL1 and ICL2, is negative. In addition, a particular note can be absorbed in which the residual of the combined fault case (IL2+VL) is closer to the discharge valve leakage fault. This is because the leakage of the discharge valve is more severe than that of the intercooler.

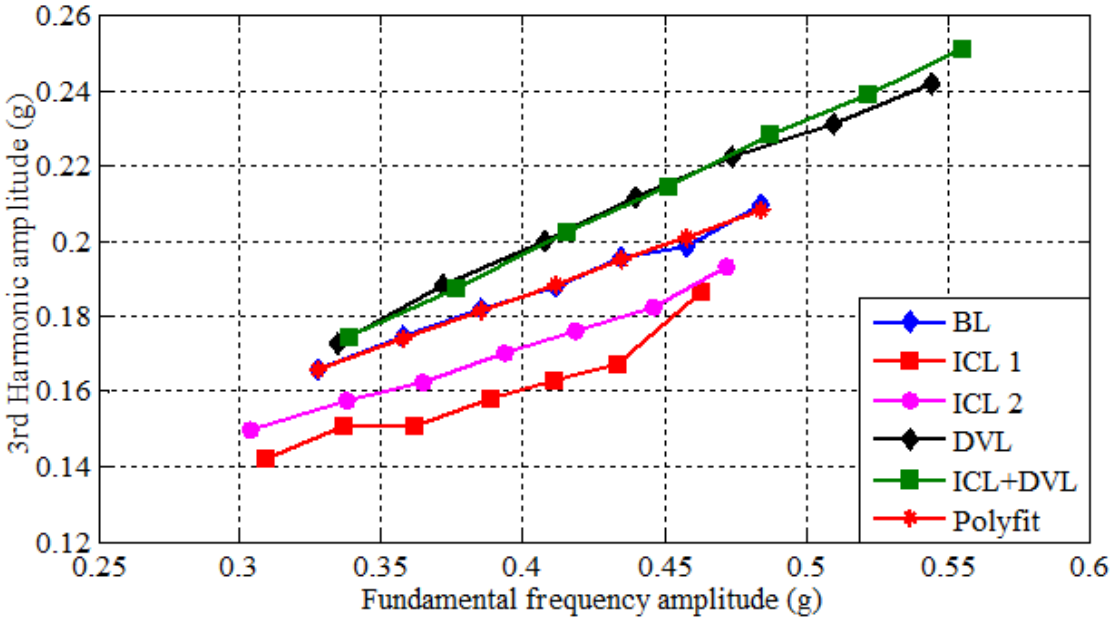

Figure 5-6 3rd harmonic amplitude vs. fundamental frequency amplitude

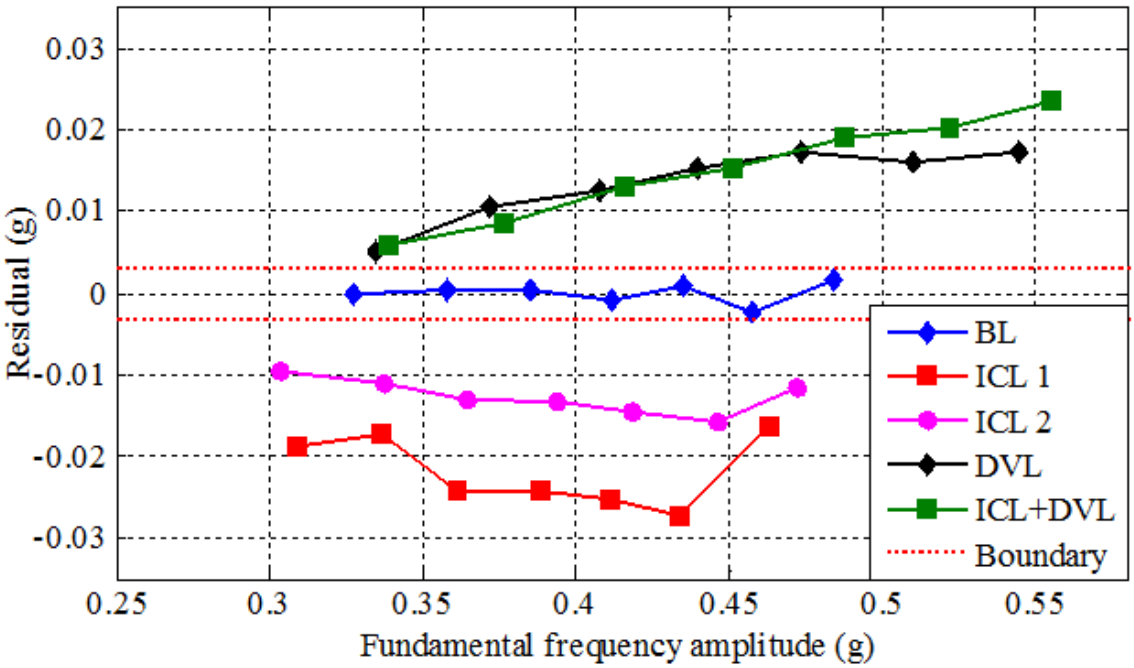

Figure 5-7 Fault signal classification: residual vs. fundamental frequency

5.4 Summary

Based on the findings from the experimental work the reconstruction of tangential acceleration is shown to give enough accuracy to demonstrate the compressor's discharge pressure. Further, using the relation of the 3rd harmonic and fundamental component, it is possible to detect a variety of simulated fault implemented in this work. Thus, using one on-rotor MEMS accelerometer which has two or three axes, it is possible to monitor compressor condition and detect a variety of frequently-occurring faults.

CHAPTER 6 MONITORING RC USING ANGULAR SPEED RESPONSES FROM THE ON ROTOR SENSOR

In this chapter, data acquired by wireless MEMS accelerometer installed on the compressor flywheel will be analyzed to classify faulty signals. The outcome delineate that tangential signal component of crankshaft's acceleration signal from a reciprocating compressor as obtained via one MEMS method presented in Chapter Four can effectively reflect different discharge pressures and allow common leakage faults to be differentiated for wireless online condition monitoring. Furthermore, the reconstructed tangential acceleration signal is compared with the IAS signal from an optical encoder mounted onto the end of the shaft.

6.1 Introduction

The measurement of angular speed is a common issue in a variety of applications in the area of rotating machines condition monitoring [148]. The idea behind the usage of the IAS signal as a tool for fault detection and diagnosis is that any fault occurring in the rotating machinery has a direct influence on the angular speed of the rotating shaft. It commonly provides a valuable quantity of information which reflects the physical condition of the machine [158].
Many researchers have evaluated the condition of rotating machines using IAS measurement-based condition monitoring. A study achieved in [90] investigated IAS-based planetary gearbox fault diagnostics in which the IAS signatures were obtained by demodulating the frequency modulated pulse trains. These trains were produced by two encoder wheels installed at the low-speed input and the high-speed output of the planetary gearbox. The authors concluded that the proposed IAS-based planetary gearbox condition monitoring can be effective to detect faults that might occur in the system. Besides, Renaudin et al. have proposed IAS measurements as an alternative method to conventional vibration measurement for bearing condition monitoring. According to their large experimental investigation on two different applications, including a gearbox and an automotive vehicle wheel, localized faults such as pitting in bearings produce small fluctuations in angular speed measurable by both optical and magnetic encoders, meaning that abnormal conditions can be diagnosed [159]. Moreover, in [158], the IAS was used for fault detection and diagnosis of a multistage gearbox in which a new extraction method was created by combining Empirical Mode Decomposition (EMD) and Autocorrelation Local Cepstrum (ALC). The outcomes show that the proposed approach can indicate gear faults efficiently.

Many other researchers have employed an optical encoder to obtain IAS: however, cost and installation difficulties are issues that make it important to find an alternative to measure IAS. As mentioned in previous chapters, due to the recent development in wireless transmission techniques and Micro Electro Mechanical Systems (MEMS) technology, it becomes feasible to measure the on-rotor accelerations of rotating machines at low cost for condition monitoring. As the transducer is directly attached to a rotor, it will be able to capture dynamic characteristics of the rotating part with high accuracy [97], making wireless MEMS accelerometers a good alternative to expensive optical encoders.

The work achieved in Chapter Five has been developed by improving on the data collection method, through bringing in the wireless data transmission technique, which enables online condition monitoring. Additionally, to confirm the suitability of the wireless accelerometer as a measurement device for reciprocating compressor condition monitoring, the IAS is calculated using the reconstructed tangential acceleration signal, which is obtained based on the method presented in Chapter Three and compared with the IAS signal from an optical encoder.

6.2 IAS Measurement Based on Encoder

IAS measurement is widely used in the area of fault detection and diagnosis, monitoring health condition and control of rotating machines. By studying IAS variations, a sizeable quantity of information regarding the health of the machine can be obtained [148].

A range of approaches are applicable to measuring angular speed, with newer strategies for processing encoder signals being developed in an attempt to enhance performance. These strategies may follow two fundamental approaches: measurement of the duration of one encoder signal cycle; or counting how many pulses occur within a set time period [148].

6.2.1 Measurement Principle

In general, average angular speed may be defined as:

$$\omega = \frac{\Delta\theta}{\Delta t}\left(rad/\sec\right) \tag{6-1}$$

Where $\Delta\theta$ is the angular displacement and Δt is the time taken to complete the displacement.

It is necessary to identify variance in speed within a revolution to diagnose faults and monitor condition. Therefore, these applications require devices which can produce more than one pulse for each revolution: for example, optical encoders and magnetic pick-ups are suitable, among other possible approaches

In this work, the IAS are measured using an optical encoder which is placed on the rotor end. The encoder's working principles are presented in Figure 6-1 (a). It uses a single Light Emitting Diode (LED) mounted on a slotted wheel and photo detector pair that generates pulses with the turning of the wheel; and the speed of an object can be calculated by measuring

the pulse duration Δ_{ti} (i.e. elapsed time or time span for a pulse *i*) between successive pulses [148].

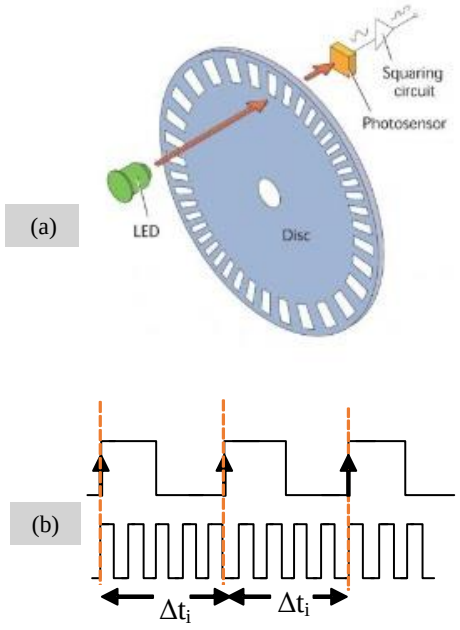

Figure 6-1 (a) Encoder principle and (b) operations of measuring elapsed time

Assuming that, *M* is the encoder pulses in one revolution, t_s (in seconds) be the clock cycle duration, N_c be the value of clock cycles in one speed pulse is given by and one unit of angular distance is $2\pi/M\,(rad)$, then the IAS in $rad/\sec$ can be calculated as [160]:

$$IAS = \frac{2\pi}{\Delta t_i M}(rad/\sec) \tag{6-2}$$

Where Δt_i is the time interval of the given speed pulse and it is equal to $N_c t_s$

Also, Suppose the clock frequency is f_c, the IAS then recasts in revolutions per minute (rev/min) as [148]:

$$IAS = \frac{60\, f_c}{N_c M}(rev/\min) \tag{6-3}$$

Traditional encoders have been used for a long time in industrial settings to monitor machine performance and for fault detection. However, these sensors are usually expensive, not suitable for isolated environments and their installation is difficult. Therefore, many researchers have

tried to use MEMS sensors, which are low-cost, small in size and easy to install, as an alternative to encoders [161].

6.2.2 Selection of Sensor

The signal from angular speed sensor represents the connection between angular displacement and time. A wide range of rotary sensors (rotary encoders) is commercially obtainable to achieve such function. The choice of a suitable encoder for a specific application is generally made according to the following factors; encoder resolution, accuracy, environmental suitability (temperature, humidity and magnetic effect), cost and sensor installation convenience [148]. Rotary encoders are classified by sensing technology used to convert the rotary position information of the rotating machine into a corresponding electrical signal. On the basis of sensing technology, commonly-used sensors are optical encoders, magnetic encoders and Hall effect sensors[162].

Considering the design principles of the rotary encoder is essential to ensure that a suitable encoder is chosen for each application [163]. For applications where a higher resolution and accuracy are required, the basic design principles of optical encoders are the best amongst all design principles. However, magnetic encoders can be used in a broad variety of conditions with regard to temperature and installation tolerance. These are not sensitive to dust and can provide excellent performance in harsh environments [148].

It is possible to install non-contact or contact sensor equipment based on the approach used. However, contact sensor equipment must be carefully installed to avoid sensors being misaligned or eccentrically positioned. In comparison, non-contact sensors achieve extremely reliable measurements, have a longer mechanical lifespan, can tolerate axial movement well and are appropriate for applications with electrical isolation [148].

6.3 IAS Measurement Based on the On-rotor MEMS Accelerometer

As explained in Chapter Three, the measured signal using 3-axis on-rotor MEMS accelerometers contains the required rotor dynamic information and projected gravitational accelerations, which can be successfully removed using the method proposed in Chapter Three. The pure tangential acceleration signal can be calculated as:

$$a_t = \sum_{n=1}^{\infty} nr\omega_O A_n \cos\left(n\omega_O t + \phi_n\right) \quad (6\text{- }4)$$

The IAS can then be computed by finding the integration of tangential acceleration signal a_t :

$$IAS = \frac{60}{2\pi r}\int a_t \, dt \tag{6-5}$$

where r denotes the distance between the accelerometer and the centre of the wheel.

6.3.1 Wireless Sensor Node

As mentioned in Chapter Four and illustrated in Figure 6-2, a wireless sensor node is mounted on the compressor flywheel to measure on-rotor acceleration. It is constructed basically with an ADXL345 MEMS accelerometer to measure the on-rotor acceleration signals, a low power microcontroller (MCU) to read the data and a BLE module used to send the measured data wirelessly to a remote computer for post signal processing. A 270 mAh lithium battery is used to power the sensor node [14].

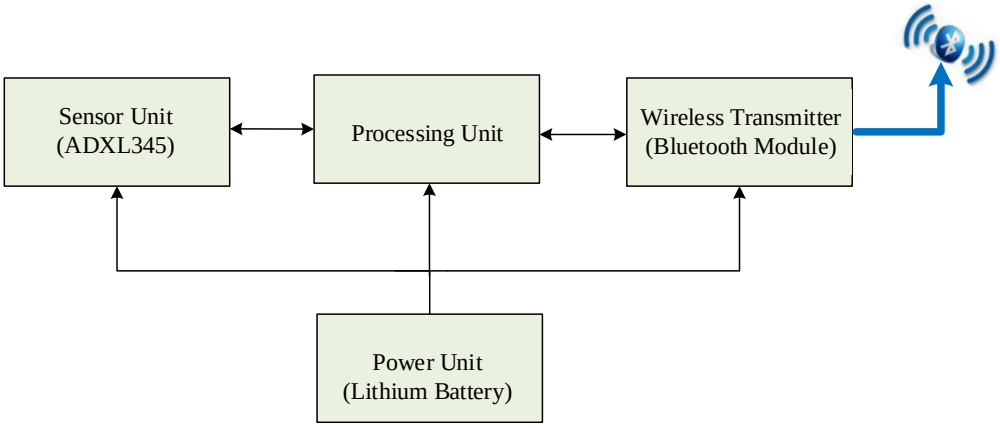

Figure 6-2 Transmitter circuit schematic

6.4 Comparison Study of IAS from Encoder and Wireless Accelerometer

The signals obtained from both an optical encoder and wireless MEMS accelerometer are processed as explained in Sections 6-2-1 and 6-3 to extract IAS signals in the time domain. Figure 6-3 illustrates the procedures used to extract IAS signals. This chapter benchmarked and confirmed the wireless accelerometer signals for future fault detection and diagnosis.

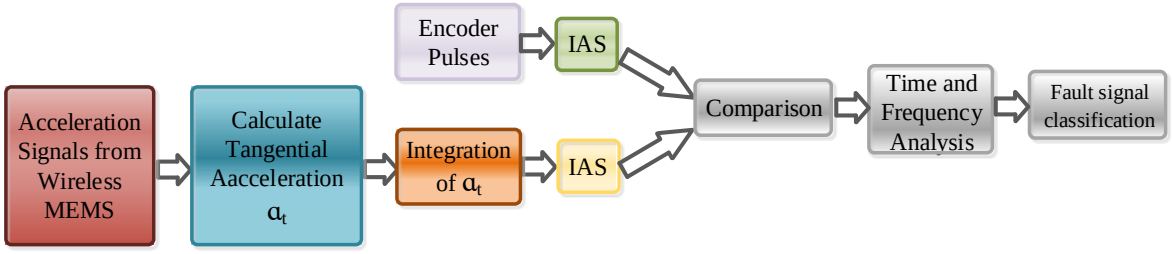

Figure 6-3 IAS extraction block diagram

6.4.1 Test Rig Setup

To confirm the performance of the wireless accelerometer sensor, a compression experimental study with incremental encoder was performed on a two-stage, single acting Broom Wade (Model TS9) reciprocating compressor, which is driven by a three phase 2.5 kW induction motor KX-C184. As shown in Figure 6-4, an incremental shaft encoder, RI32, is installed on the end of the flywheel to measure the IAS. As explained in Chapter Four, the encoder provides two outputs: 100 electrical pulse trains per revolution; and one pulse per revolution, known as the index signal. Besides, a MEMS accelerometer, ADXL345, is attached directly to the flywheel to measure the on-rotor acceleration.

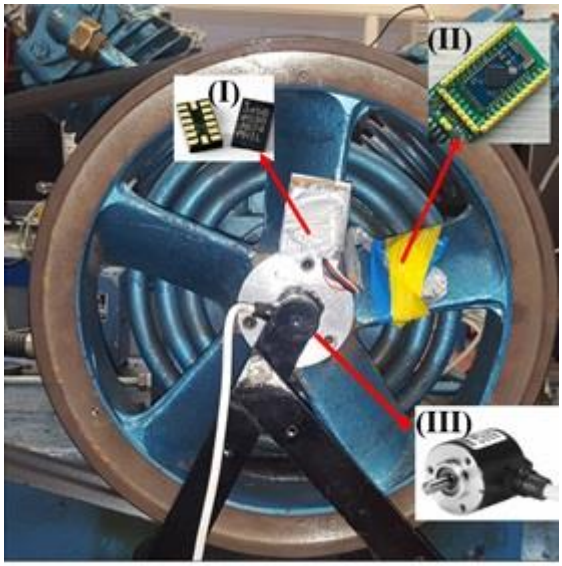

Figure 6-4 Schematic of a 2-stage reciprocating compressor along with the installation of (I) MEMS accelerometer, (II) microcontroller board and (III) optical encoder

6.4.2 Test Procedure

For the testing period, ADXL345 is set for operation within a ±16g dynamic range at a 200 Hz sampling rate. This enabled the characteristics of the dynamic rotor to be measured sufficiently. The collected data then transmitted remotely to a host computer using BLE protocol. Measurements were also taken for encoder and tank pressure, and data for this was acquired using a CED 1401 system at a 49019 Hz sampling rate.

Overall five data sets were taken across a range of conditions for the compressor, including healthy state as the baseline and investigating four conditions of fault. These faults were produced when the reciprocating compressor was made with different common compressor faults. The measurements were taken for intercooler leakage (IC), second stage discharge valve leakage (DVL), discharge valve leakage on the high pressure cylinder combined with asymmetric stator winding of the motor (DVL+ASW), and intercooler leakage combined with asymmetric stator winding of the motor (IC+ASW).

6.5 Results and Discussion

Figure 6-5 displays the periodic wireless sensor outputs in both X- and Y- axes as well as their frequency spectrums when the tank pressure reads around 80 psi. From these frequency spectrums, it can be seen that the peak value is at about 7.4 Hz, which is actually the compressor speed as explained in Chapter Five. By combining the accelerations signals measured by wireless MEMS sensor in X-axis and Y-axis using the method proposed in chapter Three, the pure tangential acceleration signals can be reconstructed as shown in Figure 6-6.

It is clear that the main components are the fundamental frequency and next three consecutive harmonics that composes the tangential acceleration. The amplitude corresponding to the fundamental frequency component is the largest when compared with the other harmonics, wherein the third harmonic component shows a higher values in contrast to its second and fourth counterparts. This reflects general description of the crankshaft dynamics caused by contributions from reciprocating inertia and air pressure perturbations within the reciprocating compressing system.

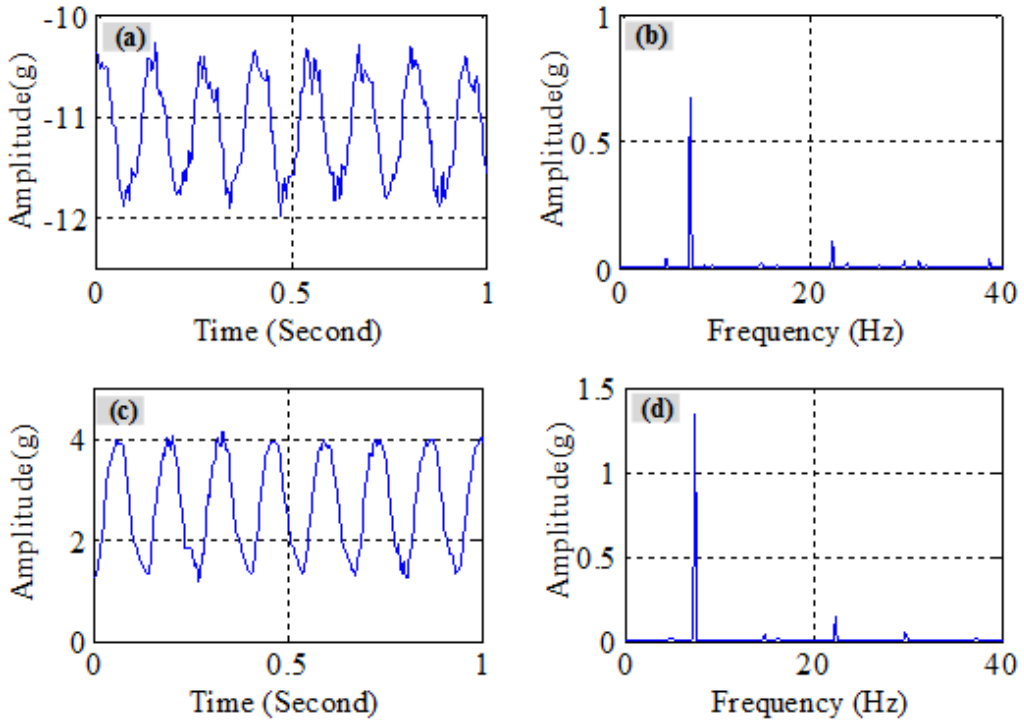

Figure 6-5 Acceleration signals at pressure of 0.55 MPa (80 psi) (a) X-axis, (b) its spectra, (c) Y-axis and (d) spectra

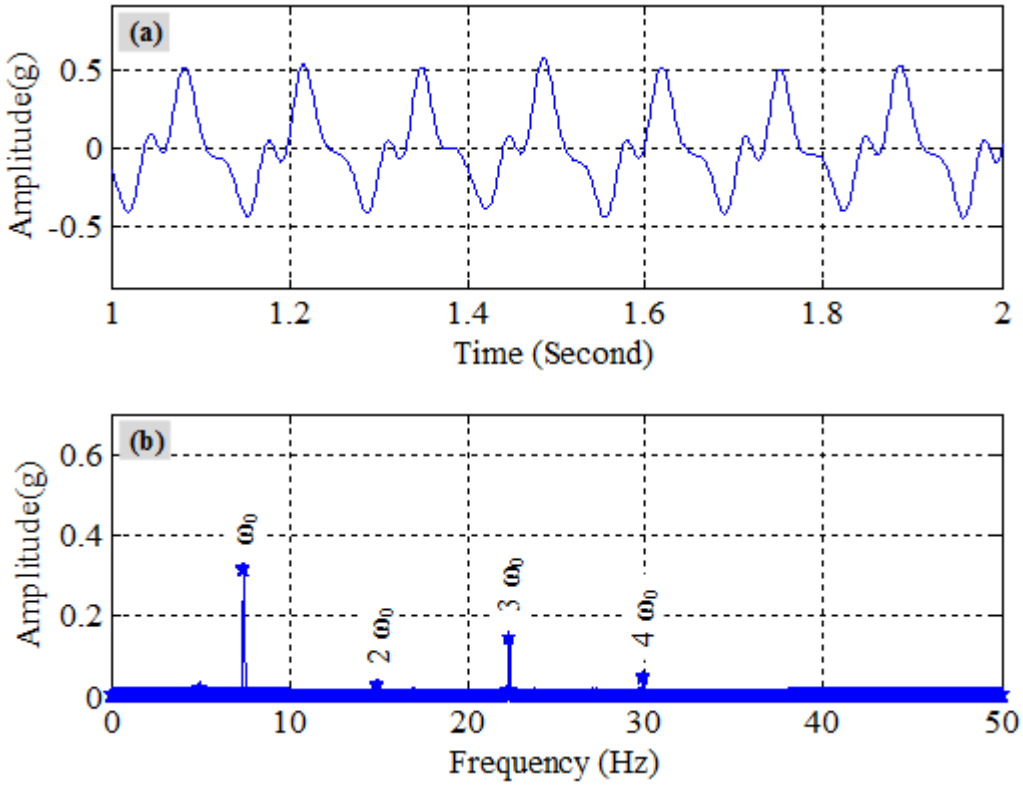

Figure 6-6 Tangential acceleration at conditions of tank pressure at 0.55 MPa or 80 psi; (a) temporal domain and (b) frequency domain.

To establish whether the presented features generally implement the dynamic characteristics, Figure 6-7 shows reconstructed signals for various tank pressure levels. From this, linear correlations are observed for fundamental frequency, third and fourth harmonics with pressure over the entire of its range. This is a result of the torque induced by pressure. Meanwhile, the second harmonic correlates in a non-linear mode with pressure, demonstrating torque impact because of the inertia of the reciprocating mass. Further, the amplitudes of the fundamental and third harmonic are comparatively high, allowing sequential pressure alterations to be distinguished.

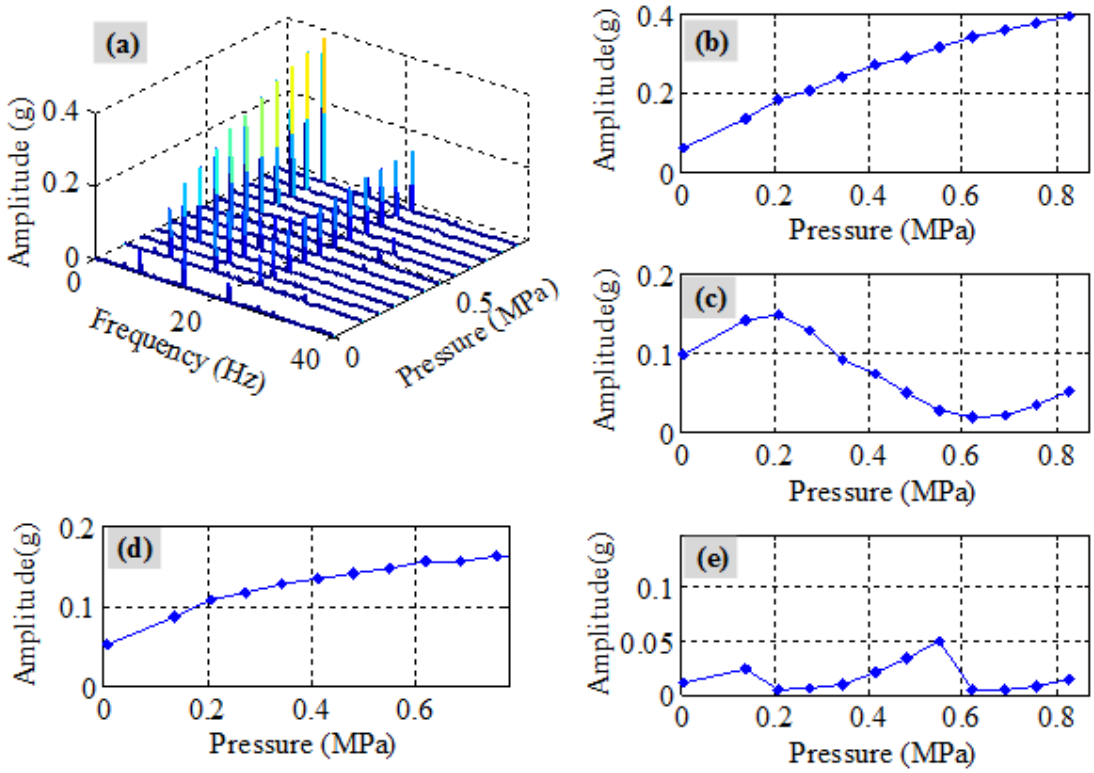

Figure 6-7 Spectral mode representation of tangential acceleration under tank pressures condition ranging from 0.14 MPa or 20 psi to 0.83 MPa or 120 psi, (a) as a waterfall plot; amplitude of (b) fundamental frequency; (c) 2nd harmonic; (d) 3rd harmonic and (e) 4th harmonic

To verify the reconstructed signal, the multiple pulse signal from the encoder is also computed using the method explained in Section 6.2.1 and then the IAS of the compressor flywheel is obtained and presented in Figure 6-8.

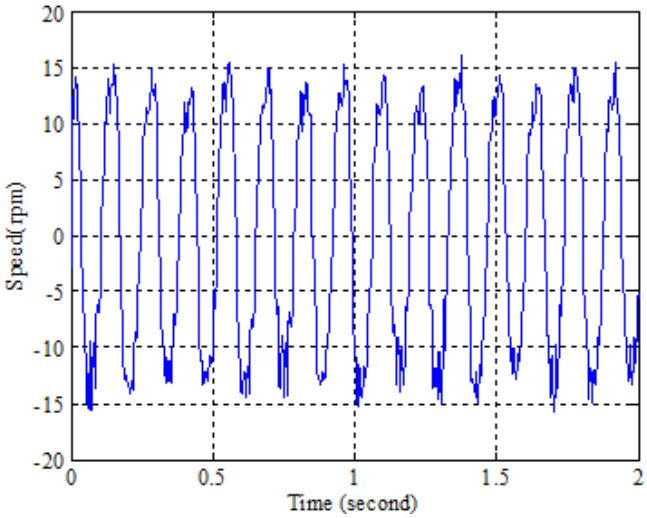

Figure 6-8 IAS signal (in time domain) calculated using optical encoder

Besides, an integration operation is performed on the obtained tangential acceleration by the wireless MEMS accelerometer so as to get the alternating IAS signal. The both computed IAS signals are compared and presented in Figure 6-9 in both time domain and frequency domain. It can be seen that the IAS signals from these two sensors have good match in amplitude and waveform shape besides having very similar frequency components.

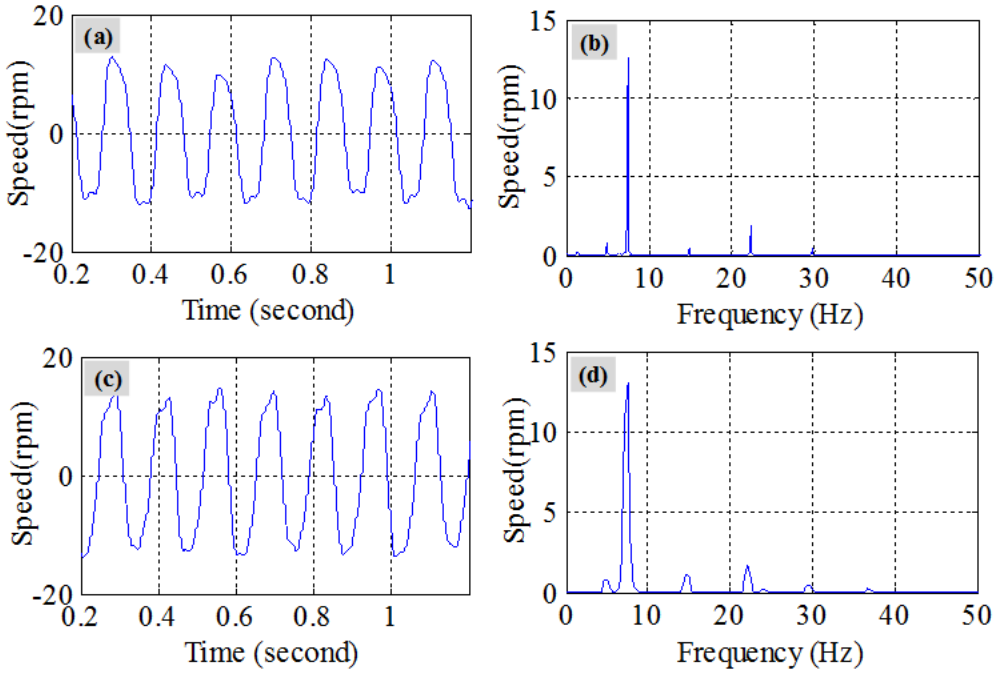

Figure 6-9 Comparison from the wireless sensor and encoder. (a) wireless sensor time domain, (b) wireless sensor frequency domain, (c) encoder signal time domain, (d) encoder signal frequency domain

Moreover, the IAS obtained using the encoder is used to calculate the tangential acceleration by differentiate the IAS and a compression between this signal and the reconstructed one is shown in Figure 6-10. This verifies the accuracy of the reconstructed signal obtained from wireless accelerometer.

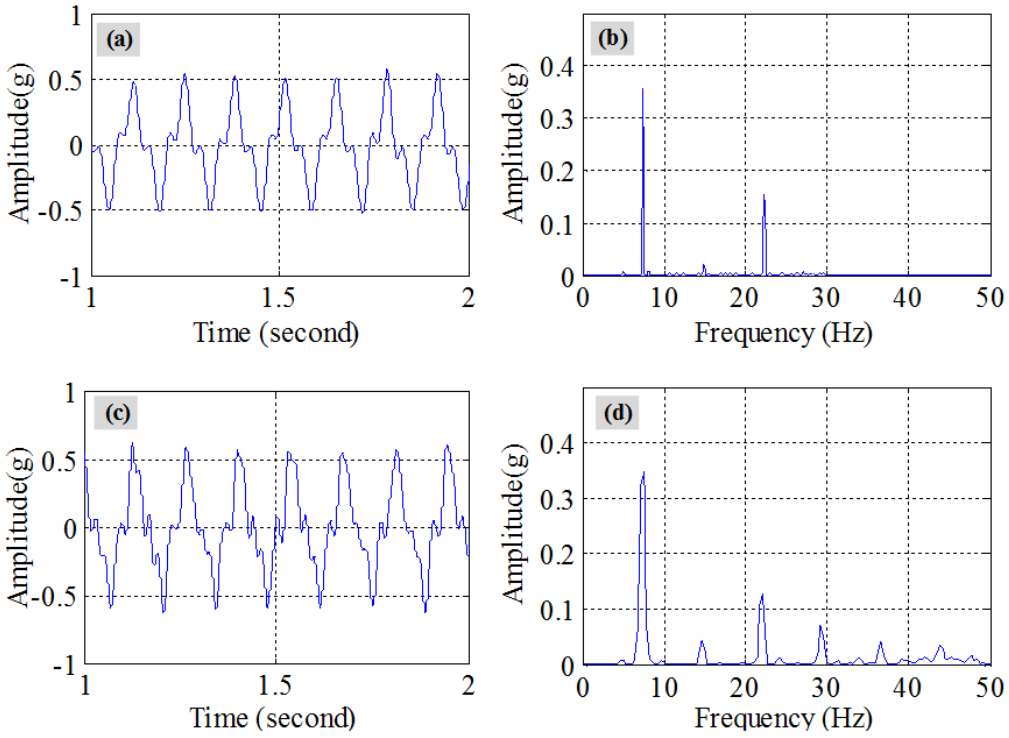

Figure 6-10 Tangential acceleration comparison from the wireless sensor and encoder. (a) wireless sensor temporal domain, (b) wireless sensor frequency domain, (c) encoder signal temporal domain, (d) encoder signal frequency domain

To classify the compressor condition using the reconstructed tangential acceleration, the harmonics changes with discharge pressure for all test conditions are presented in Figure 6-11. It is evident that the amplitude from fundamental and 3rd harmonic frequency components show a linearly increasing tendency with the tank pressure from 0 to 0.82 MPa (120 psi). Therefore, these two components may further be used in condition classification.

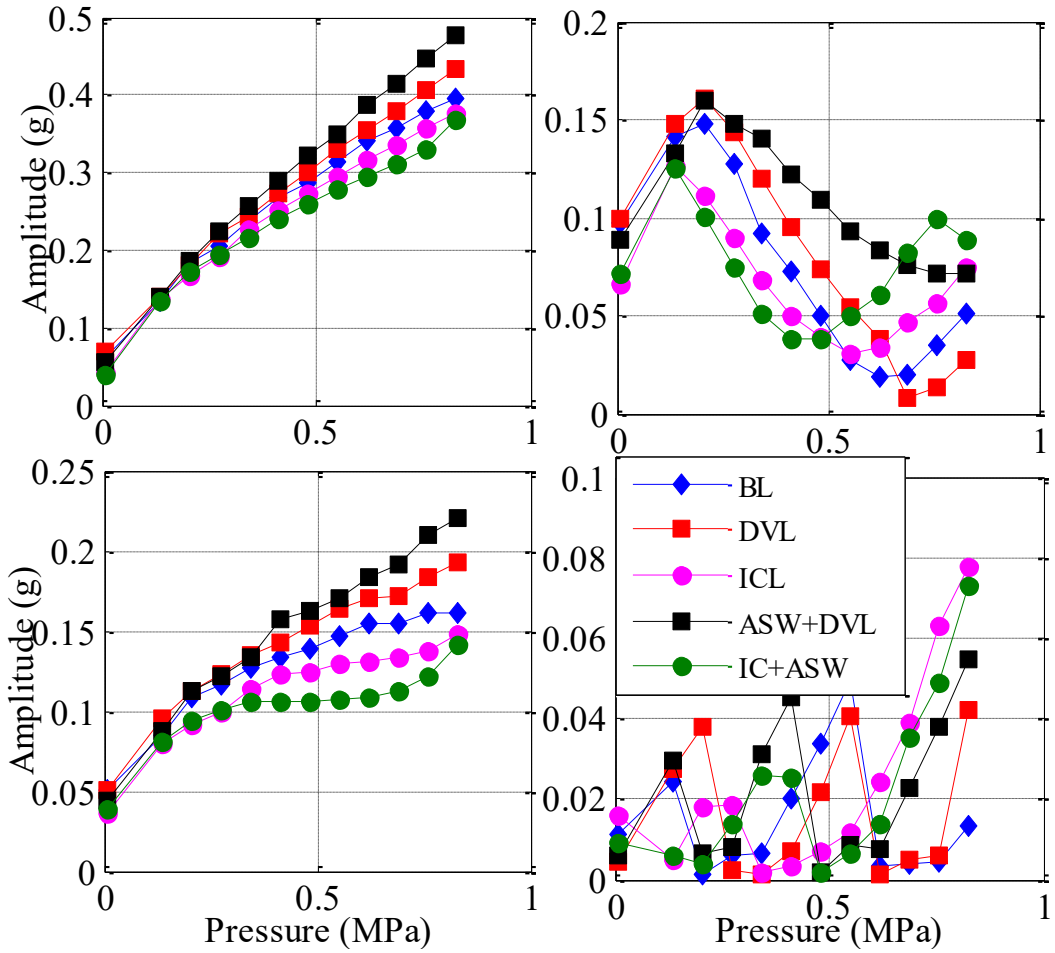

Figure 6-11 Amplitude corresponding to (a) fundamental frequency; (b) 2nd harmonic; (c) 3rd harmonic and (d) 4th harmonic of the reconstructed acceleration signal plotted against the tank pressure

Figure 6-12 (a) presents the relationship of the 3rd harmonic with the fundamental frequency component for pressure reading of tank varying between 60 psi and 120 psi (from 0.41 MPa to 0.83 MPa). Thereafter, the faulty conditions are classified in Figure 6-12 (b) based on the fundamental frequency and the 3rd harmonic component. It is clear that the intercooler fault (ICL), the discharge valve leakage fault (DVL) and both combined faults (IC+ASW, DVL+ASW) can be successfully isolated from the baseline condition (BL). Furthermore, the residual of DVL related fault, i.e. DVL and combined fault (DVL+ASW), is positive whereas that of ICL related fault, i.e. ICL and combined fault (ICL+ASW), are negative. In addition, it can also be seen that the effect of the combined fault in both cases is clearly evident while the combined fault makes the residual more deviated from the boundaries.

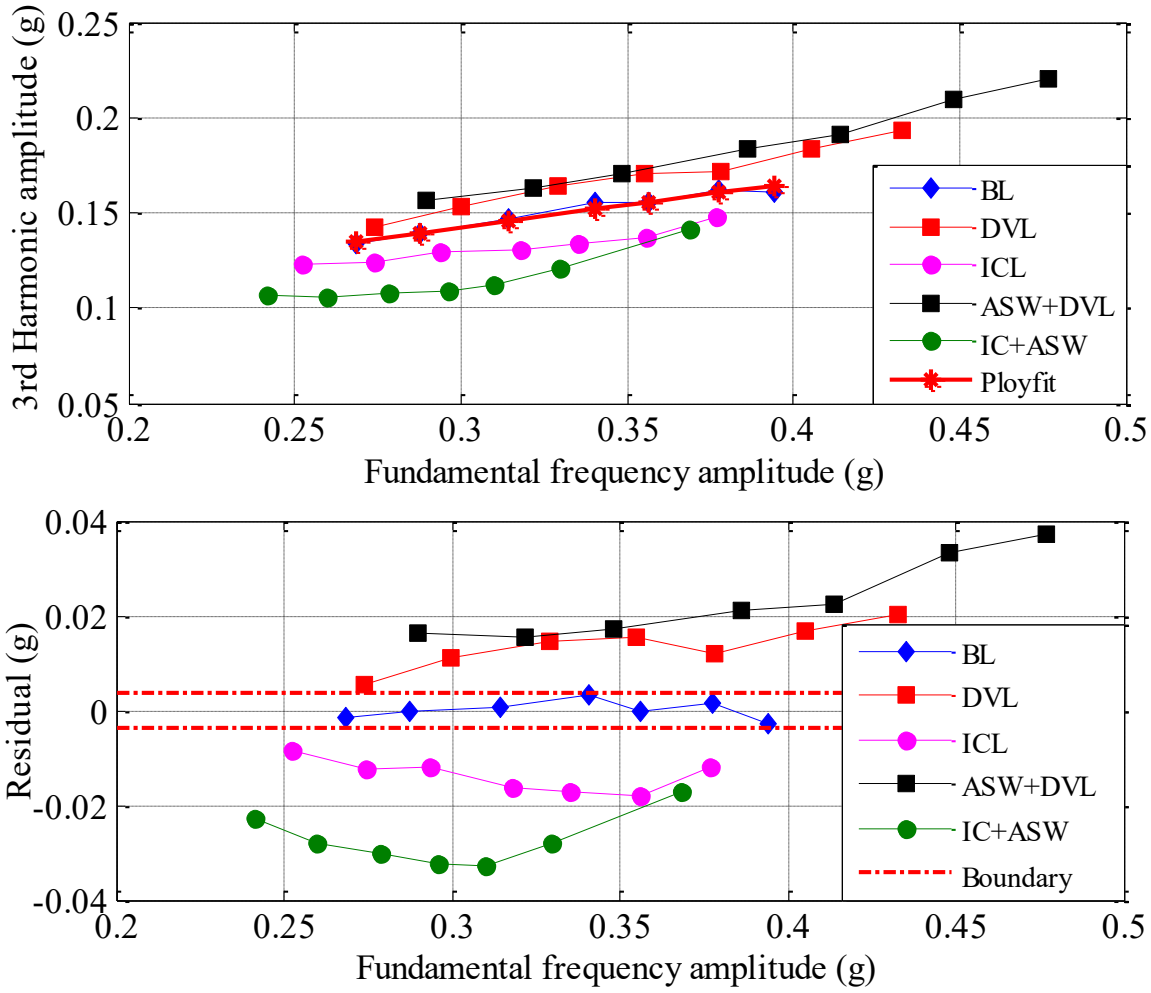

Figure 6-12 Plots of fault signal classification for (a) 3rd harmonic against fundamental frequency (b) residual against fundamental frequency

6.6 Summary

In this chapter, a performance test of a wireless MEMS accelerometer is carried out for different frequent faults appearing in a reciprocating compressor. The measured signals of the wireless sensor are compared with signal obtained from a traditional optical encoder. The experimental results demonstrate that, acceleration signals from the wireless sensor and the encoder are similar and there is a very good matching in both waveform and spectrum, proving that the reconstructed tangential acceleration from on-rotor accelerometer is accurate and reliable. Furthermore, a remote condition monitoring and common fault diagnostic for a reciprocating compressor can be achieved by using only one MEMS accelerometer.

CHAPTER 7 INVESTIGATION OF TWO APPROACHES TO THE CANCELLATION OF GRAVITATIONAL ACCELERATION BASED ON THE MONITORING OF RC CONDITIONS

This chapter presents an experimental comparison results between two varieties of methods which may be utilised to get rid of the gravitational acceleration from the on-rotor accelerometer outputs and to characterize the rotor dynamics precisely. The first method uses one MEMS sensor, in which the true tangential acceleration signals are obtained using both orthogonal outputs of MEMS accelerometer mounted on the reciprocating compressor flywheel, discussed earlier in Chapter 3. In the second one, two MEMS sensors were installed diametrically in opposite direction to each other on the rotating part enabling the projected gravity signal to be eliminated by adding the acceleration outputs from both accelerometers. Experimental results show that both methods can be successfully used to remove the projected gravitational accelerations, and the conditions of reciprocating compressor can be effectively identified using the tangential accelerations.

7.1 Introduction

As MEMS accelerometers measure the dynamic vibration as well as the gravitational acceleration, the rotor dynamic measured by the sensor is influenced by the gravity which increase the output amplitudes by 1g. This undesirable signal should be removed at any cost so that the rotor dynamics characteristics can be precisely calculated. Based on the calculation given in Chapter three, both gravitational acceleration and tangential acceleration, sensed by the Ax3 installed on the compressor flywheel, can be presented in the time and frequency domain and shown in Figure 7-1. From this figure, we note same frequency components for both signals, which indicates that these signals cannot be separated using a low-pass filter [153].

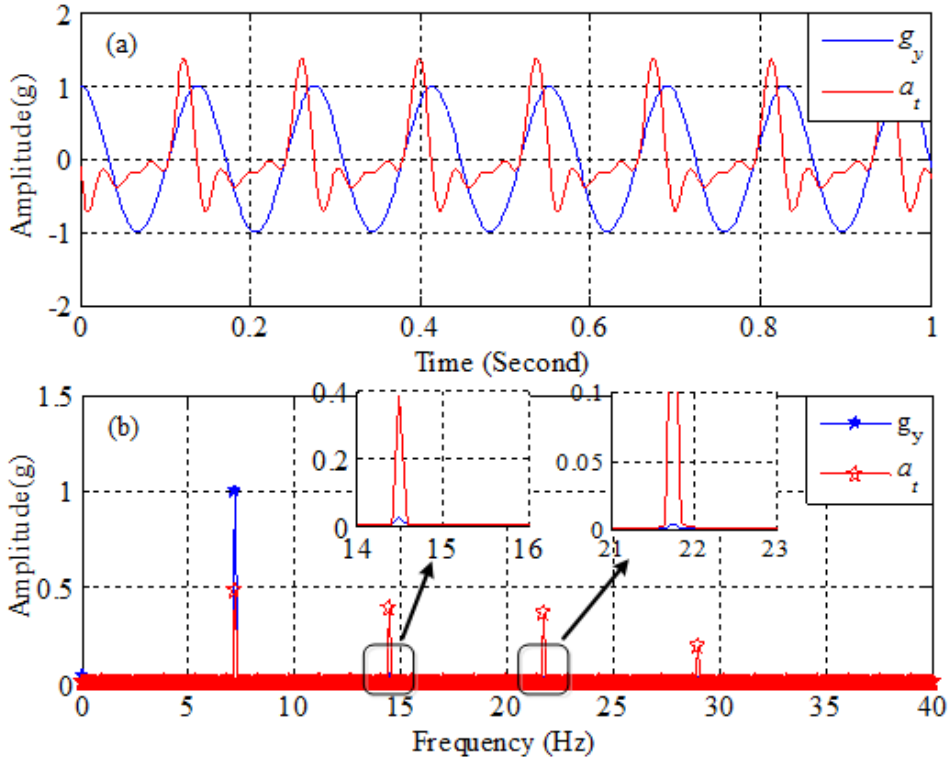

Figure 7-1Accelerations measurements (a) tangential acceleration and gravity signal projected on Y-axis g_y in time domain (b) frequency components

To utilize the dynamic rotor measurements for machinery condition monitoring, the effect of the gravitational acceleration should be removed. This chapter compares between two methods employed to eradicate the gravitational acceleration effect to obtain the accurate information regarding the rotor dynamics.

The first method uses one MEMS sensor in which the tangential accelerations signals are reconstructed using both orthogonal outputs from MEMS accelerometer attached to the flywheel of the reciprocating compressor. In the second method, two MEMS accelerometers were installed at diametrically extreme positions on the flywheel enabling the gravitational acceleration effect to be removed by adding the acceleration signals from the both accelerometers.

7.2 Gravitational acceleration cancellation using two MEMS sensors

The first method was explained in Chapter three, thus this Chapter will explain the second one. As shown in Figure 7-2, this method uses two tiny MEMS sensors to eliminate the projected gravity from on-rotor MEMS accelerometer. The pure tangential acceleration can be obtained after removing the gravitational acceleration by adding the Y-axis signals from both the on-rotor accelerometers [100].

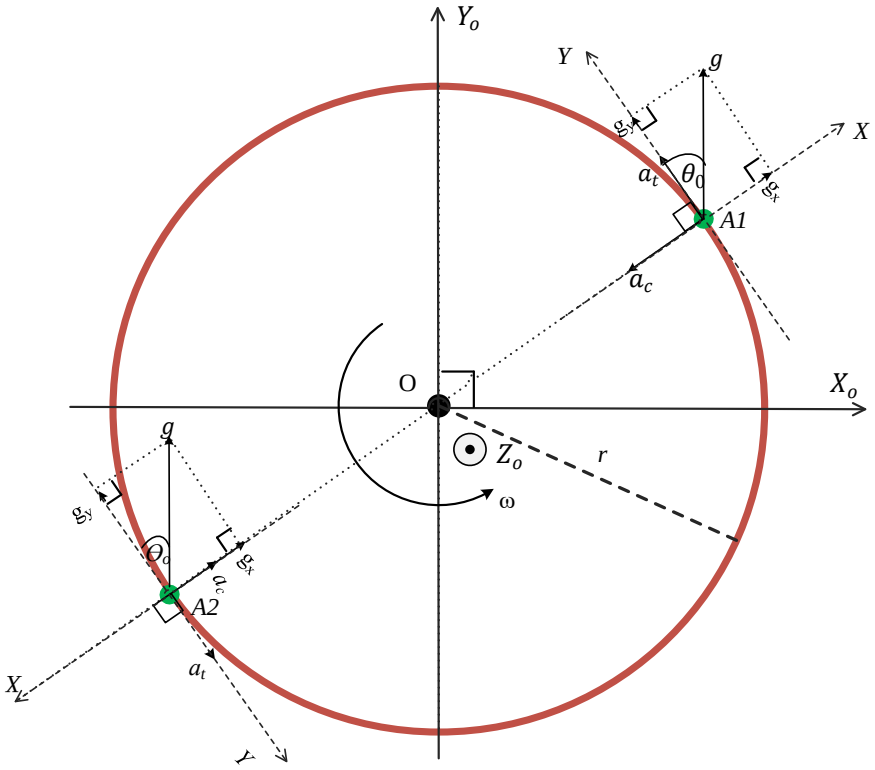

Figure 7-2 Acceleration analysis of two mass (A and B) rotating around point O [153]

From Figure 7-2, the signals measured by sensor $A1$ in the direction of both the X-axis (horizontal) and Y-axis (vertical) can be written as [153]:

$$a_{A1x} = -a_c + g_x = -a_c + g\sin\theta$$
$$a_{A1y} = a_t + g_y = a_t + g\cos\theta \quad (7\text{-}1)$$

Similarly, for sensor $A2$,

$$a_{A2x} = a_c + g_x = a_c + g\sin\theta$$
$$a_{A2y} = a_t - g_y = a_t - g\cos\theta \quad (7\text{-}2)$$

From Equations (7-1) and (7-2), it is clear that gravity effect can be found in both MEMS accelerometers outputs, but these undesirable signals can be simply eliminated by summing a_{A1y} and a_{A2y}, given:

$$a_{A1y} + a_{A2y} = 2a_t \quad (7\text{-}3)$$

Consequently, the pure tangential acceleration can be calculated as:

$$a_t = \frac{a_{A1y} + a_{A2y}}{2} \quad (7\text{-}4)$$

From Equation (7-4), it can be confirmed that the true tangential acceleration can be calculated by adding the two accelerometers outputs signals that measured in the tangential directions. Although this method is very simple, however, it has some disadvantages that should be taken into consideration. Firstly, it is not trivial to mount the MEMS sensors precisely in the required positions; in the second place, this method is more expensive and finally, the sampling rates for the two MEMS accelerometers may be different resulting in necessary post-processing of the signal. For the testing period, both accelerometers were configured for operation within a ±16g dynamic range at a sampling rate of 1600 Hz. However, after collecting the acceleration data and calculating the actual sampling frequencies it was found that neither of the two sensors had a sampling rate at the specified one, 1600Hz. The sampling rates of the two AX3 data logger sensors were found to be closer to 1590 Hz and 1610 Hz, respectively.

To be able to use two MEMS accelerometers method to eliminate the gravity effect, the sampling rate should be corrected using the process shown in Figure 7-3.

Figure 7-3 MEMS sensor sampling rate correction steps

1- Synchronise the data collected by both sensors at the same time;
2- Divide both Ax3 data sets into numerous frames;
3- Finally, resample the accelerometers' data based on the frames [153].

Assuming that the first AX3 sensor and the second one have independent errors ΔA and ΔB correspondingly, then the overall error generated from adding both sensors' data can be expressed as [164]:

$$TE = \sqrt{(\Delta A)^2 + (\Delta B)^2} \tag{7-5}$$

where TE indicates the total error of the method used to obtain the tangential acceleration.

7.3 Test Rig Facility

In this experimental comparison, a reciprocating compressor, shown in previous chapter, was used as a case study to evaluate the effectiveness of two MEMS sensors method in obtaining pure tangential acceleration for machine condition monitoring and compare the findings with that obtained using one sensor.

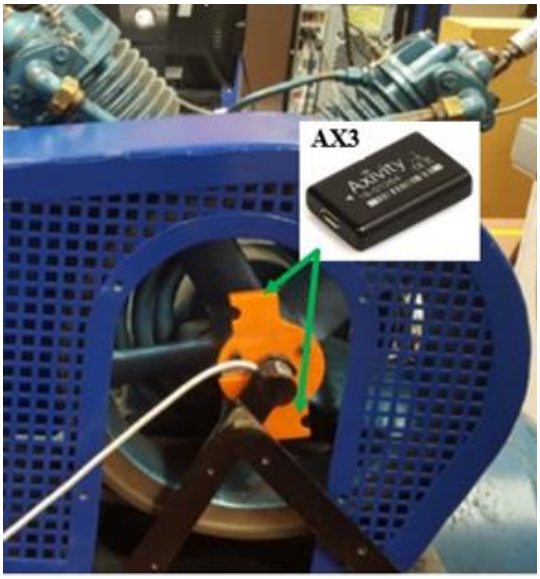

Figure 7-4 MEMS accelerometers installation on the reciprocating compressor flywheel

As shown in Figure 7-4, two AX3 data logger sensors are mounted diametrically in opposite direction on the flywheel of the reciprocating compressor at a distance of 50 mm from the flywheel centre allowing the measured acceleration signals to be within the dynamic range (±16g) of the sensors.

7.4 Test Procedure

For the testing period, both AX3 was set for operation within a ±16g dynamic range at a 1600 Hz sampling rate. This enabled the characteristics of the dynamic rotor to be inspected adequately. Simultaneously, measurements were also taken for tank pressure, and data for this was collected using a CED 1401 system at a 49019 Hz sampling rate. Two different datasets were acquired across a range of conditions for the compressor, to evaluate the performance contrast in both methods. First set of data is healthy (BL), having been collected while the reciprocating compressor was operating normally without any faults. The second data were collected from a leaky system produced in the piping that transports the processing air to high stage from the low stage. In high stage, the fault was simulated by loosening the intercooler by rotating the nut through one revolution.

7.5 Results and Discussion

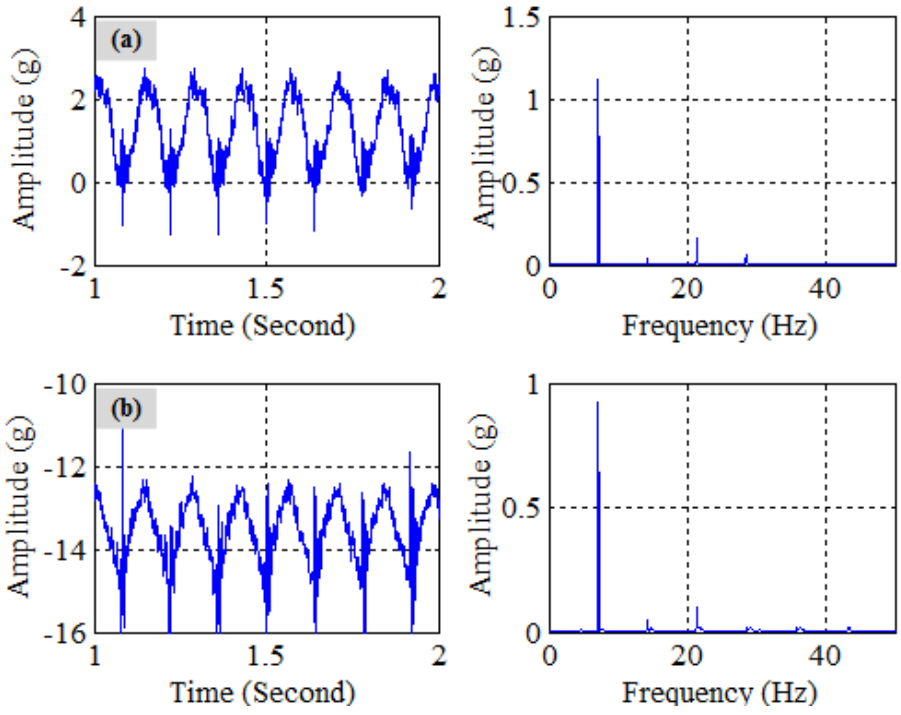

Figure 7-5 The 1st On-rotor MEMS acceleration measurements and their spectra at pressure of 0.55 MPa (around 80 psi): (a) signal measured at X-axis and (b) signal measured at Y-axis

Figure 7-5 displays a representative set of the sensor's outputs for the first sensor in the direction of X- and Y- axes with their spectra when the compressor was operating approximately at 0.55 MP (80 psi), while Figure 7-6 presents the outputs of the second MEMS

accelerometer, measured in the direction of both X and Y axes with their spectra at the same pressure.

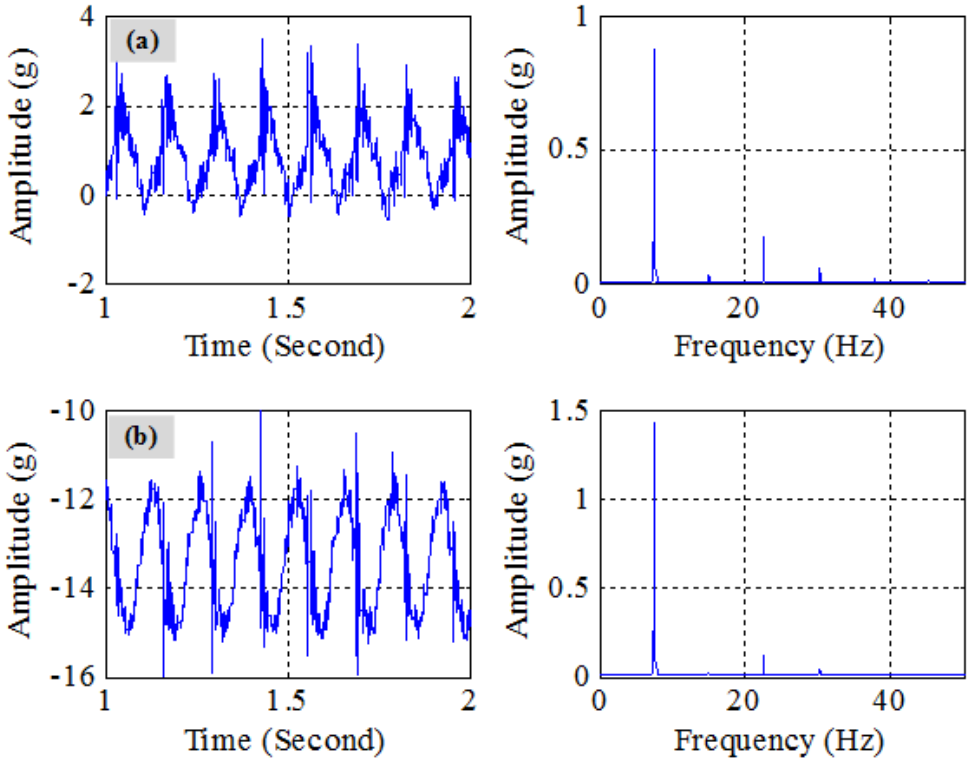

Figure 7-6 The 2nd On-rotor MEMS acceleration measurements and their spectra at pressure of 0.55 MPa (around 80 psi): (a) signal measured at X-axis and (b) signal measured at Y-axis

Figure 7-7 presents the tangential acceleration signals calculated by both methods. From this figure, it is noticeable that both acceleration signals show a good matching in terms of general waveform shape, amplitude values and frequency components, hence verifying the reliability of these two methods.

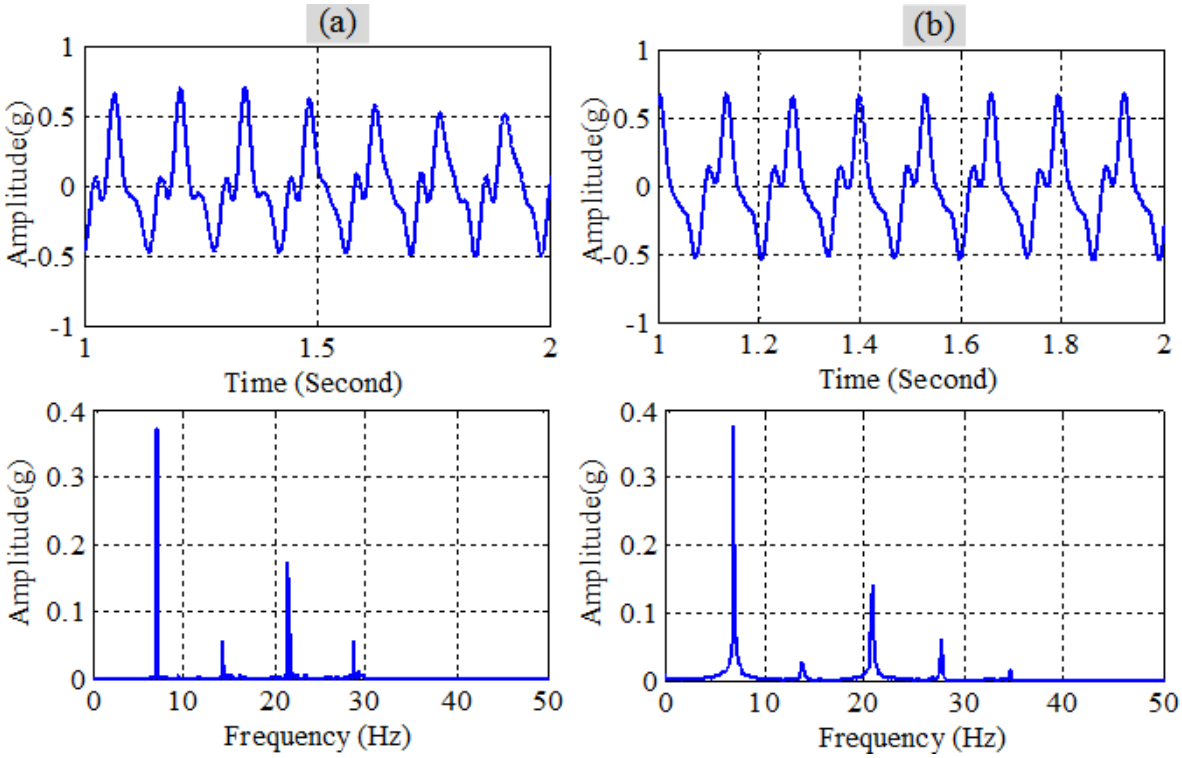

Figure 7-7 True tangential acceleration signals measured at tank pressure of 0.55 MPa (80 psi) and their spectra: (a) One MEMS method (b) Two MEMS method

To illustrate the comparison of the compressor conditions using tangential accelerations measured using the both methods, the changing of harmonics amplitude against the tank pressure for healthy case and intercooler leakage condition is shown in Figure 7-8 and Figure 7-9.

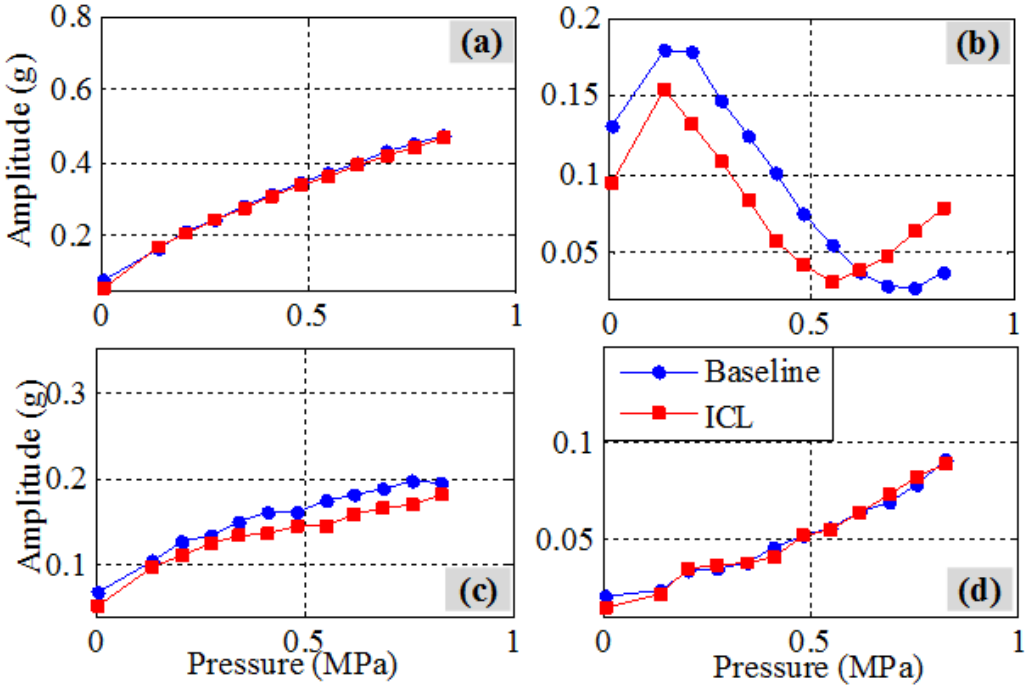

Figure 7-8 The amplitude of the tangential acceleration harmonics against tank pressure: (a) fundamental, (b) second, (c) third and (d) fourth harmonics for one MEMS method

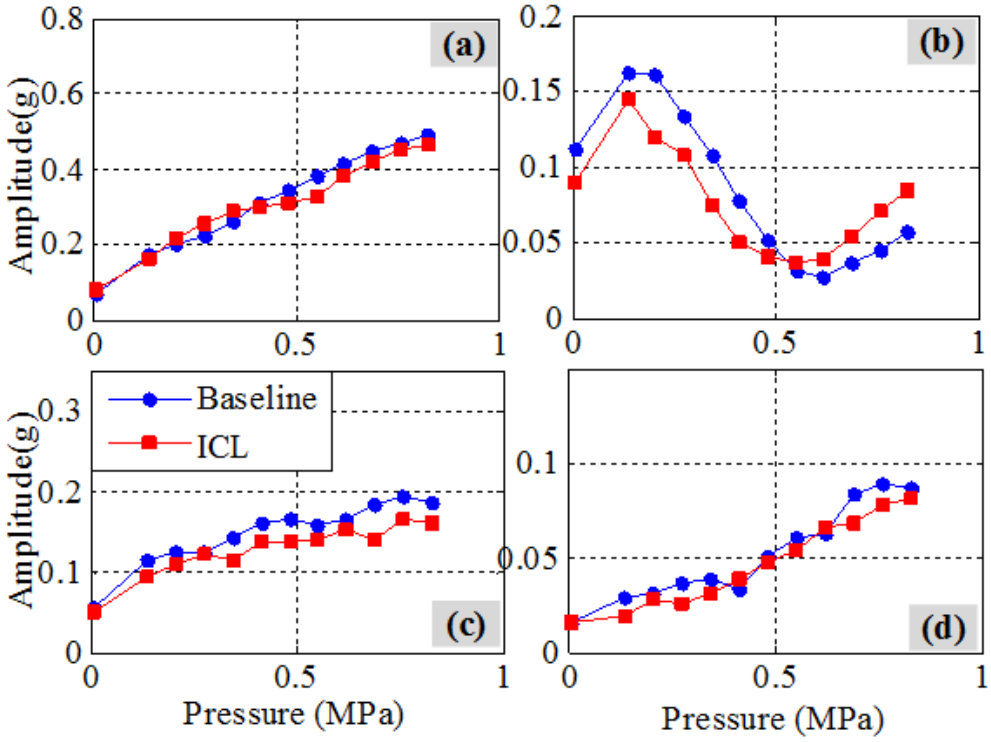

Figure 7-9 The amplitude of the tangential acceleration harmonics against tank pressure: (a) fundamental, (b) second, (c) third and (d) fourth harmonics for two MEMS method

From the above figures, the linear correlations are observed for fundamental frequency, third and fourth harmonics with pressure range from 10 to 120 psi indicating that those components can be useful for further classification of the compressor conditions. Figure 7-10 (a) depicts the relationship between the third harmonic amplitude and the fundamental frequency component for the tank pressure within a broad range of 60 psi-120 psi (from 0.41 MPa to 0.83 MPa). Thereafter, the intercooler leakage fault condition is classified in Figure 7-10 (b) based on the fundamental frequency and the residual. It is clearly shown that the intercooler fault (ICL) can be well isolated from the baseline condition (BL).

7.6 Summary

This chapter compares two different methods used to remove the gravitational acceleration, which is combined with the dynamic information, allowing the pure tangential acceleration to be obtained and used for monitoring the condition of rotating machines. Both the methods depict a favourable match in waveform shape, amplitudes and frequency contents of the tangential acceleration signals obtained from these methods. However, in case of efficiency with lower error range, one MEMS sensor method is found to be more effective over the two sensor method.

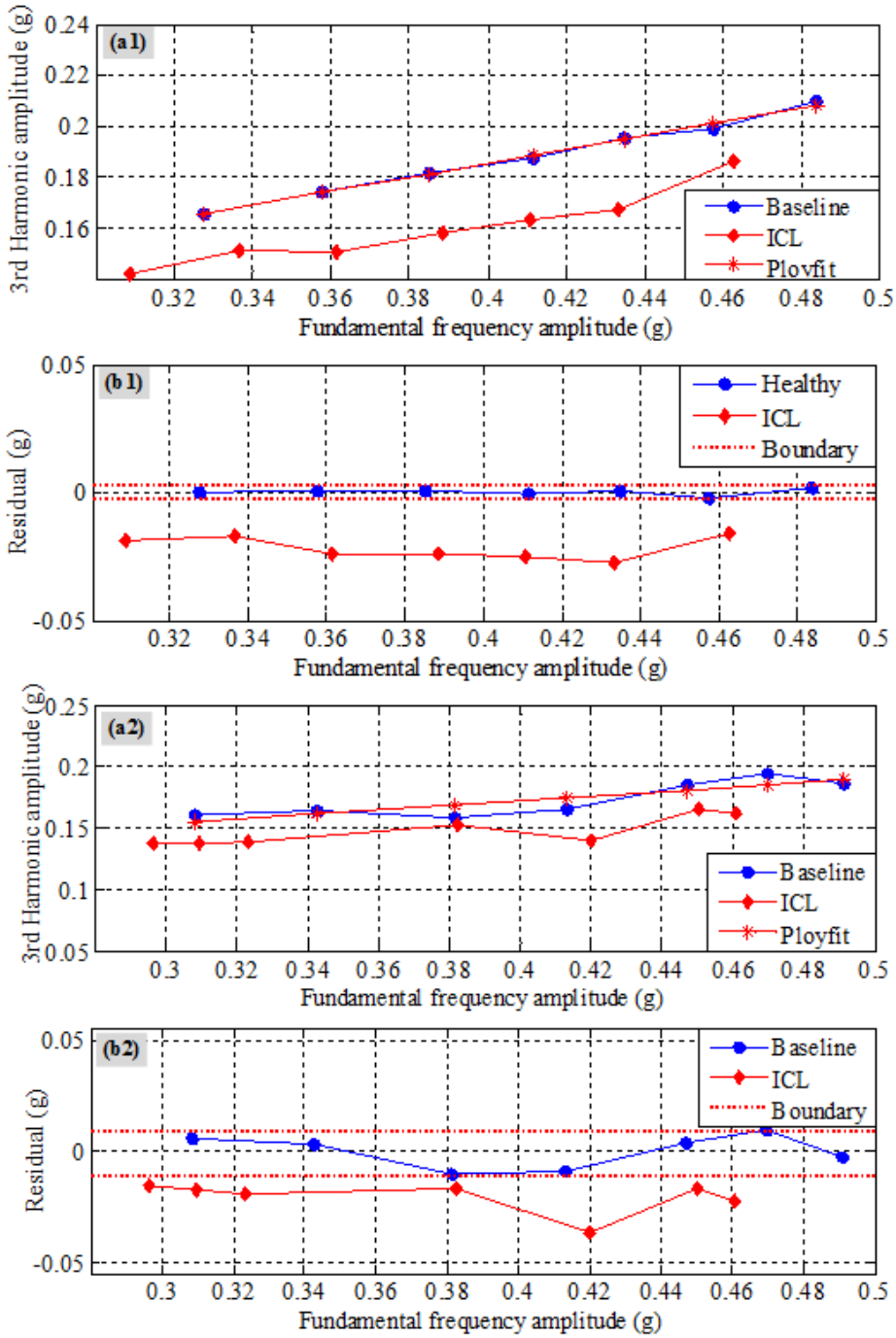

Figure 7-10 Plots showing fault classification: (a1) 3rd harmonic against fundamental; (b1) residual against fundamental frequency [one MEMS method]; (a2) 3rd harmonic against fundamental; (b2) residual against fundamental frequency [two MEMS method]

CHAPTER 8 PLANETARY GEARBOX FAULT DETECTION AND DIAGNOSIS USING AN ON-ROTOR ACCELEROMETER

This chapter studies the usage of an on-rotor MEMS accelerometer for the planetary gearbox condition monitoring. It starts with the introduction and then the brief descriptions of test rig, simulation of faults and test procedures are presented. The experimental results show that acceleration signal in the tangential direction measured on the low-speed input shaft of a planetary gearbox can clearly indicate faults and this method has actually outperformed the vibration signal acquired by a conventional accelerometer, thus providing a reliable and low-cost condition monitoring method for the planetary gearbox.

8.1 Introduction

Planetary gearboxes have strong load-bearing capacity, large transmission ratio and high efficiency of transmission [73, 74]. Due to these certain advantages, they are suitable for use in heavy industrial applications, like drive trains of the helicopter, automotive and wind turbines. But the complex structure of the planetary gearbox and their critical operating conditions can cause failure to its own components which in turn results in major economic losses to the industry. For that reason, to avoid such failures [80, 84], researchers developing an advanced fault diagnosis method to monitor the condition of the planetary gearbox. A review on the methodologies used for condition monitoring of planetary gearbox is presented in [80] and, according to the study, most methods use the vibration signal measured by the fixed type accelerometers mounted on the gearbox housing for the fault diagnosis of planetary gear box. For a planetary gear set, the vibration signal collected by the fixed accelerometer contains information from different sources containing the planet gears, sun gear, and the ring gear.

Lei et. al. showed that vibration signals can follow multiple transmission paths from its source to the accelerometers mounted on the gearbox casing which are time-varying in nature [80] and depends on the revolution of the carrier. These transmission paths may effect the acquired signal from the faulty components through interference and make the vibration signal for a planetary gear set more complicated [165]. Thus, the measured vibration signal sensed by a fixed accelerometer have a complex nature, which makes the conventional vibration-based planetary gearboxes fault detection and diagnostic techniques a challenge [93].

This problem can be solved by installing an accelerometer on the rotating shaft directly instead of installing it on the gearbox housing so that it can provide a good dynamic response from the rotating parts [96, 97] maintaining a constant distance from the accelerometer to the rotating planet gears. The revolutionary developments in MEMS technology, has made it feasible to install a low-cost MEMS accelerometer directly on the rotating shaft to obtain the dynamic response which can be useful for the fault diagnosis of rotating machines [97]. Thus, making it a good alternative to an expensive conventional accelerometer.

This chapter concentrates on a novel method for the planetary gearbox condition monitoring in which a tiny on-rotor MEMS accelerometer has been installed on the input shaft to obtain an accurate measurement of the machine dynamic characteristics.

An analytical model for the on-rotor vibration measurement process is derived. A cross section of a shaft, shown in Figure 8-1, is referred to install the sensor S, and the centre of the shaft is at C.

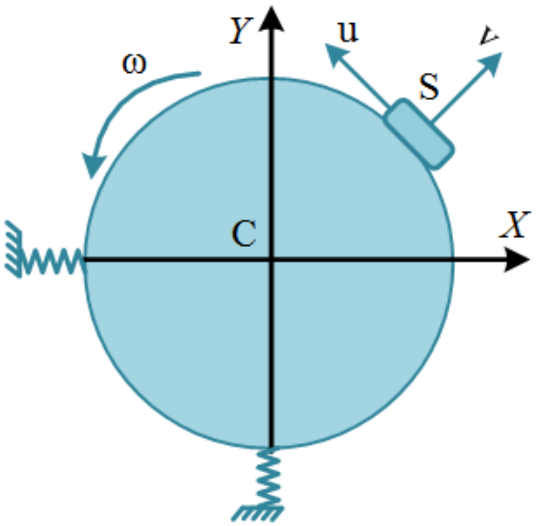

Figure 8-1 On-rotor vibration measurement geometry

The shaft revolves in an inertial frame X-Y with the angular speed of ω and has a translational movements $\ddot{x}$ and $\ddot{y}$ along X and Y axes respectively. A frame u-v that is rotating has the same origin that of inertial one and is aligned along the straight line that connects the shaft centre and the sensor *S*. The radial distance between the centre of the shaft and the sensor is represented as *r*. The outputs of the sensor are as follows:

$$\ddot{u} = -\ddot{x}\sin\theta + \ddot{y}\cos\theta + \dot{\omega}r + g\cos\theta \tag{8-1}$$

$$\ddot{v} = \ddot{x}\cos\theta + \ddot{y}\sin\theta + \omega^2 r + g\sin\theta \tag{8-2}$$

Where $\theta = \omega t = (\omega_c + \tilde{\omega}_c)t$ is the angular displacement of the sensor.

The sensor output is the combined result of the superposition of translational and rotational motions and is very sensitive to the abnormal events. These outputs have the dependency on

the rotating speed and the straight line distance between the rotating shaft and the MEMS accelerometer. The closer the distance is the higher the translational motion will be.

8.2 Experimental validation

8.2.1 Test Rig-Setup

Figure 8-2 and 8-3 show a schematic diagram of the test rig for planetary gearbox used in this experimental study.

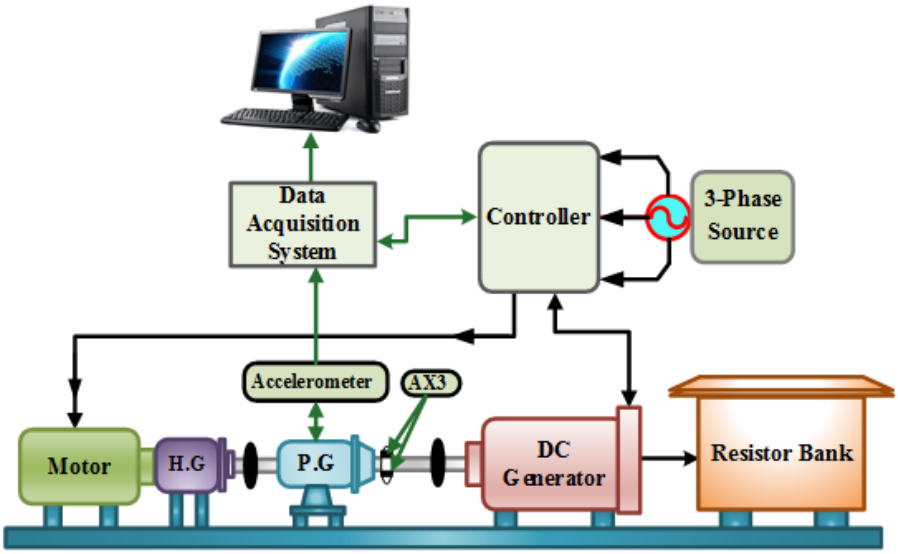

Figure 8-2 Schematic diagram of planetary gearbox test facility

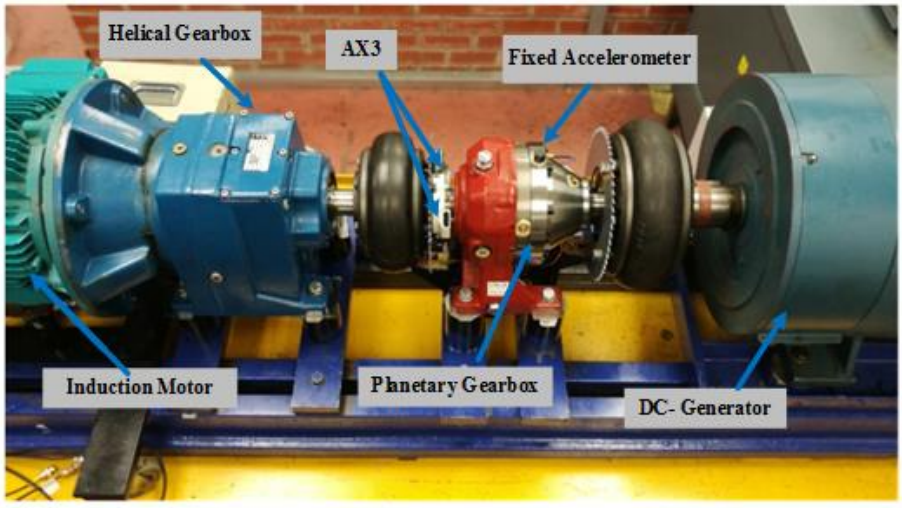

Figure 8-3 Planetary gearbox test rig and

It mainly comprises a 3-phase induction motor with 11 kW 1465rpm rating, a two-stage helical gearbox, a DC generator for providing load to the gearbox, a planetary gearbox manufactured by STM Power Transmission Ltd and two flexible tyre couplings.

The running state of the planetary gearbox was monitored using on-rotor MEMS accelerometers. The input shaft of the planetary gearbox was driven by an induction motor, the speed of which it was regulated by a speed controller with a maximum speed of 40% ≈ 584 rpm. This suggests that the input speed to the planetary gearbox was reduced to 159 rpm by the helical gearbox, with a ratio of 3.667 and thereafter the speed was again increased to 1144 rpm by the planetary gearbox with a ratio of 7.2.

As shown in Figure8-3, the accelerometers are fixed diametrically opposite to each other on the low speed input shaft of a planetary gearbox and close to the centre to record the on-rotor acceleration signals.

8.2.2 Fault Simulations

In this study, two different areas of damage were simulated in both the sun and planet gears in order to simulate the real faults in the mechanism during operation. Figure. 8-4 shows the damage in the sun gear produced by removing around 60% of the gear tooth face along the width, whilst the damage created in the planet gear by removing parts of the tooth is also presented in Figure 8-5.

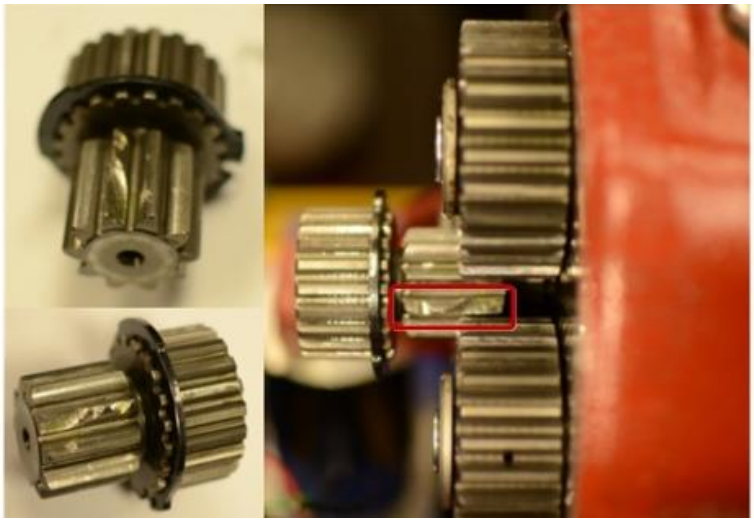

Figure 8-4 Sun Gear Tooth Fault simulation

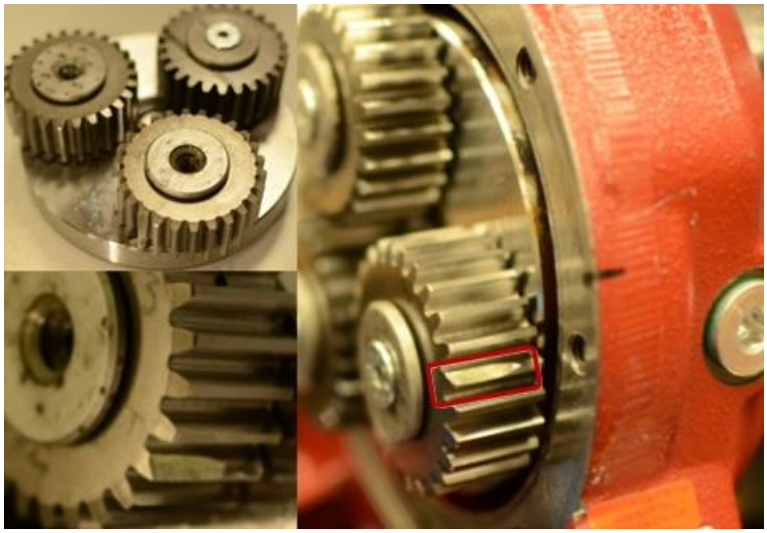

Figure 8-5 Planet Gear Tooth Fault simulation

8.2.3 Test Procedure

For the testing period, both AX3s were set for operation within a ±16g dynamic range at a 1600 Hz sampling rate. This enabled the characteristics of the dynamic rotor to be inspected adequately. The acquired data were stored in a memory compacted in AX3 data logger during planetary gearbox run-time, and thereafter are transferred to a computer for post-processing once the system is shut down. In this experimental work, three different datasets have been acquired to evaluate the performance of the MEMS accelerometers. The first data was collected in healthy condition (BL) with no faults occurred in the system. The other groups of data were acquired from the system with a damage produced on the sun gear and planet gear teeth. For each condition, the test was performed under input speed of 439.5 rpm, which is 30% of the full speed of the AC motor, and under five different load conditions, including zero load and 25%, 50%, 75%, 90% of the full load.

8.3 Results and Discussion

Figure 8-6 shows the signals obtained from the both MEMS sensors and their spectra in frequency domain at 30% of its maximum speed under 90% of its full load capacity when the system was running under healthy condition. The effect of gravitational acceleration can be removed by introducing a new parameter called tangential acceleration, which is the summation of the measured signals presented in Figure 8-7.

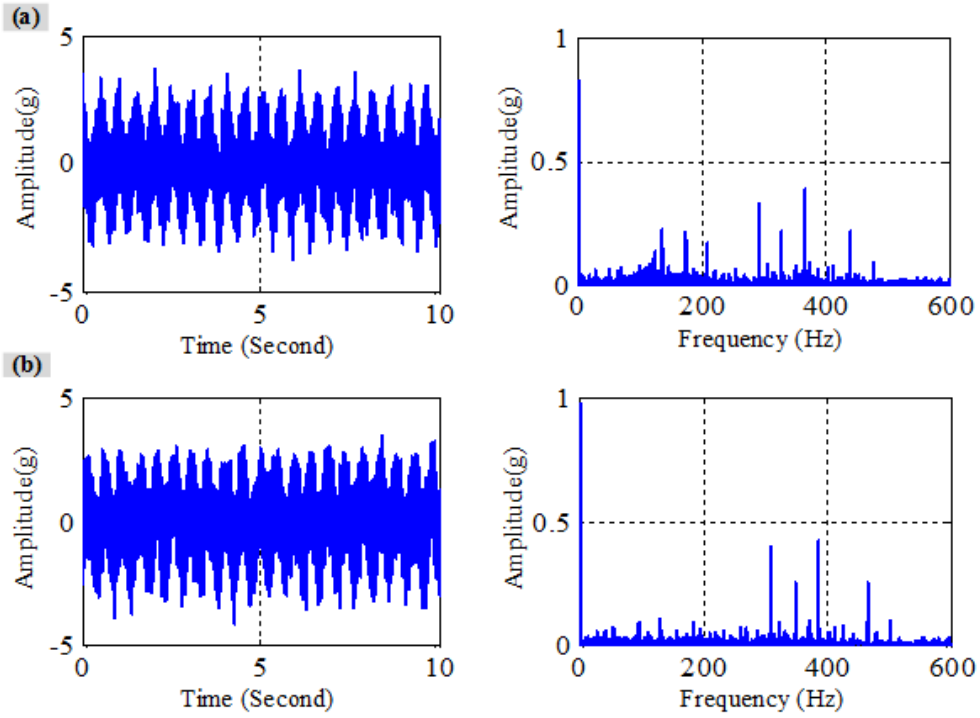

Figure 8-6 X-axis filtered acceleration signals and its spectra with 90% load and 30% speed for (a) Sensor 1 and (b) Sensor 2

From Figure 8-7b it is clear that the largest frequency component for tangential acceleration is situated at about 2.067 Hz, which denotes carrier speed, (considered the fundamental component of the low-speed input shaft).

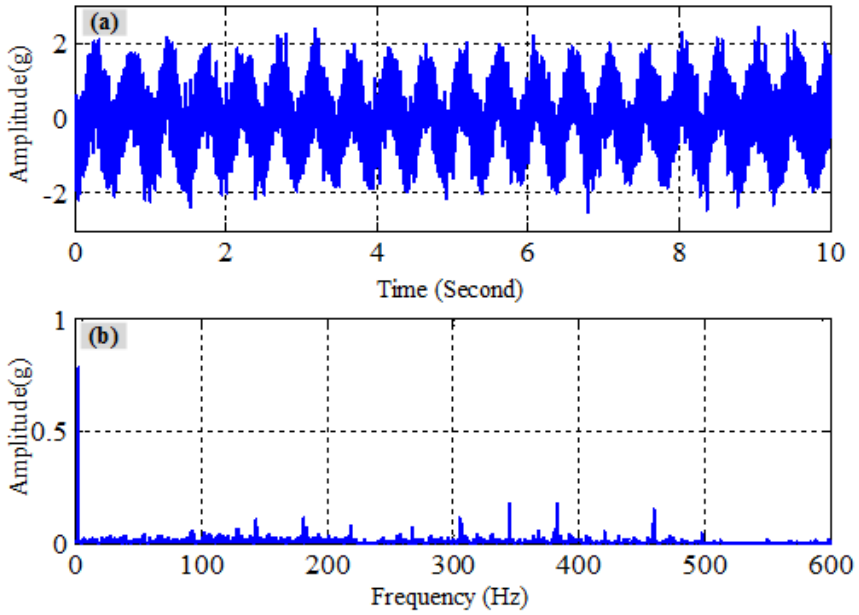

Figure 8-7 Tangential acceleration signal and spectra at 30% speed and 90% load

In the meantime, the low frequency spectra of the tangential acceleration measured at 30% speed with different loads for the sun fault and planet fault cases are presented in Figure 8-8 and Figure 8-9 respectively. We note from the figures that the amplitudes of low frequency spectra are affected by the damage and the amplitudes of many frequency components such as f_{sf} and f_{pf} *has* become higher which indicates that such frequencies can be used to denote the sun and planet gears fault.

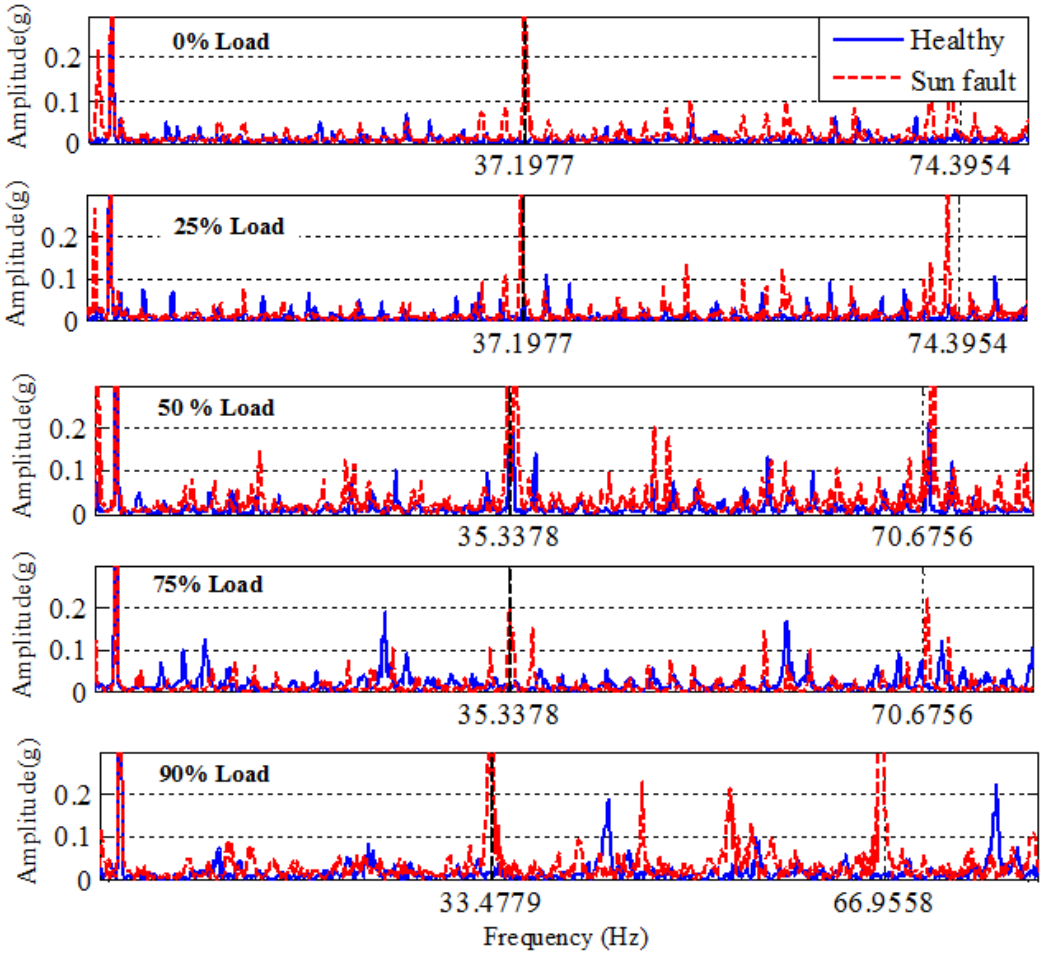

Figure 8-8 Spectrum in the low frequency range for the healthy and sun fault cases at 30% speed

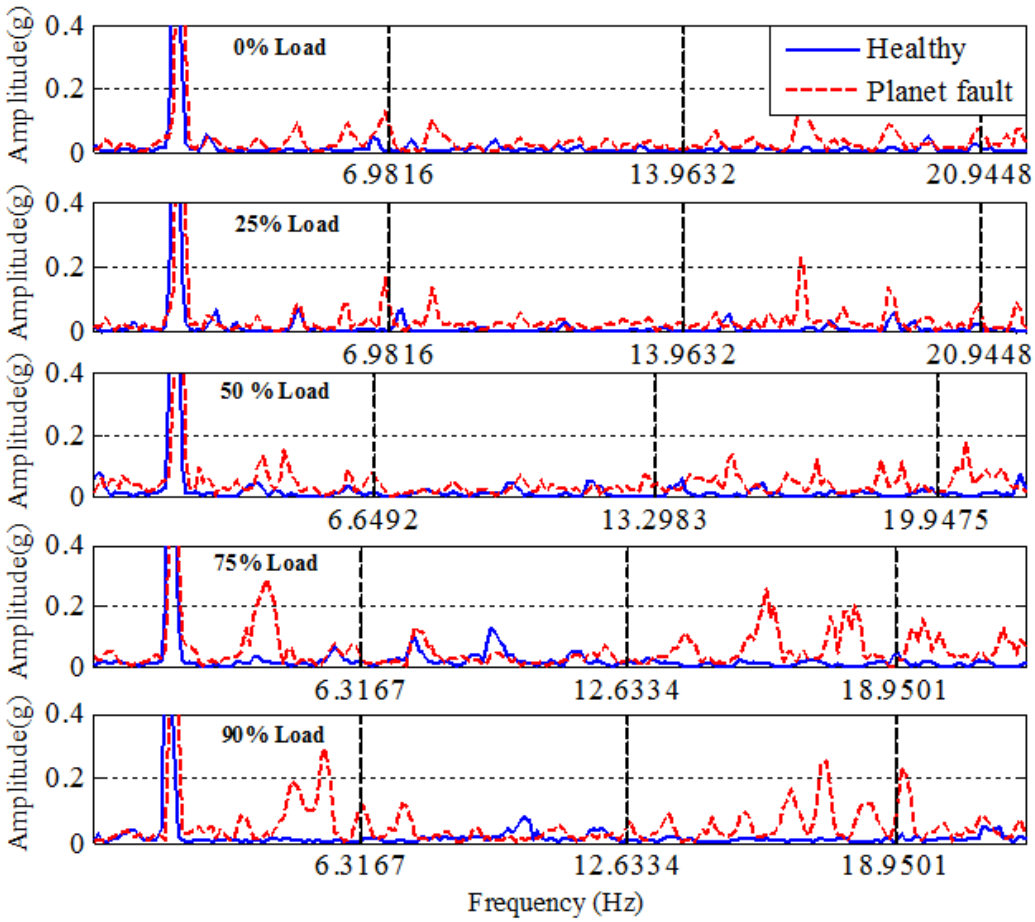

Figure 8-9 Spectrum in the low frequency range for the healthy and planet fault cases at 30% speed

To investigate the sun gear and planet gear faults more precisely, the high frequency range of the spectrum of the tangential acceleration at 30% speed with different loads are presented in Figure 8-10 and Figure 8-11.

In both cases, the amplitudes of the harmonics around the meshing frequency (f_m) are generally higher than that of the low frequency range sections. From the literature review it has been found that the high frequency spectra analysis of the vibration signals has been reported by many researchers and most of these studies have concluded that sideband signals around the 3rd harmonic of the meshing frequency can be effectively used to indicate different faults. From Figure 8-10 and Figure 8-11, it is noticeable that the sidebands amplitudes around the 3rd harmonic of the meshing frequency higher compared to the 1st and 2nd harmonics. The sidebands around the 3rd harmonic of the meshing frequency are analyzed and some distinctive

peak components have been found that can be useful for the fault diagnosis of planetary gear box. For example, $3f_m+f_{rc}$, $3f_m+2f_{rc}$, $3f_m-f_{sf}$, $3f_m+f_{sr}$, $3f_m-f_{sf,}+f_{rc}$, and $3f_m+f_{sf,}+f_{rc}$ could be useful to indicate the sun gear fault, whilst, $3f_m-3f_{pf}$,$3f_m+10f_{pf}$, *and* $3f_m-6f_{pf,}-f_{rc}$can successfully indicate the planet gear fault.

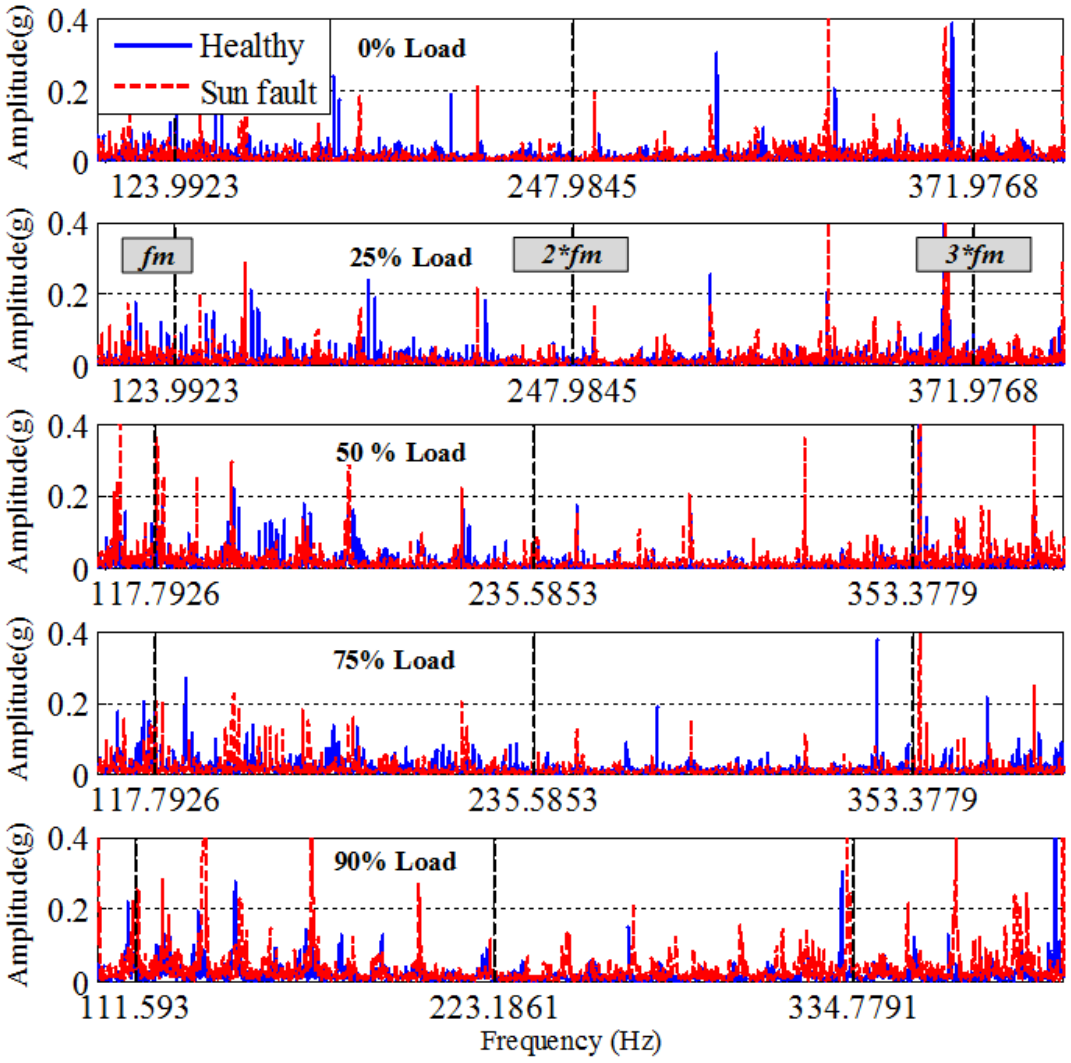

Figure 8-10 Spectrum in the high frequency range for the healthy and sun fault cases

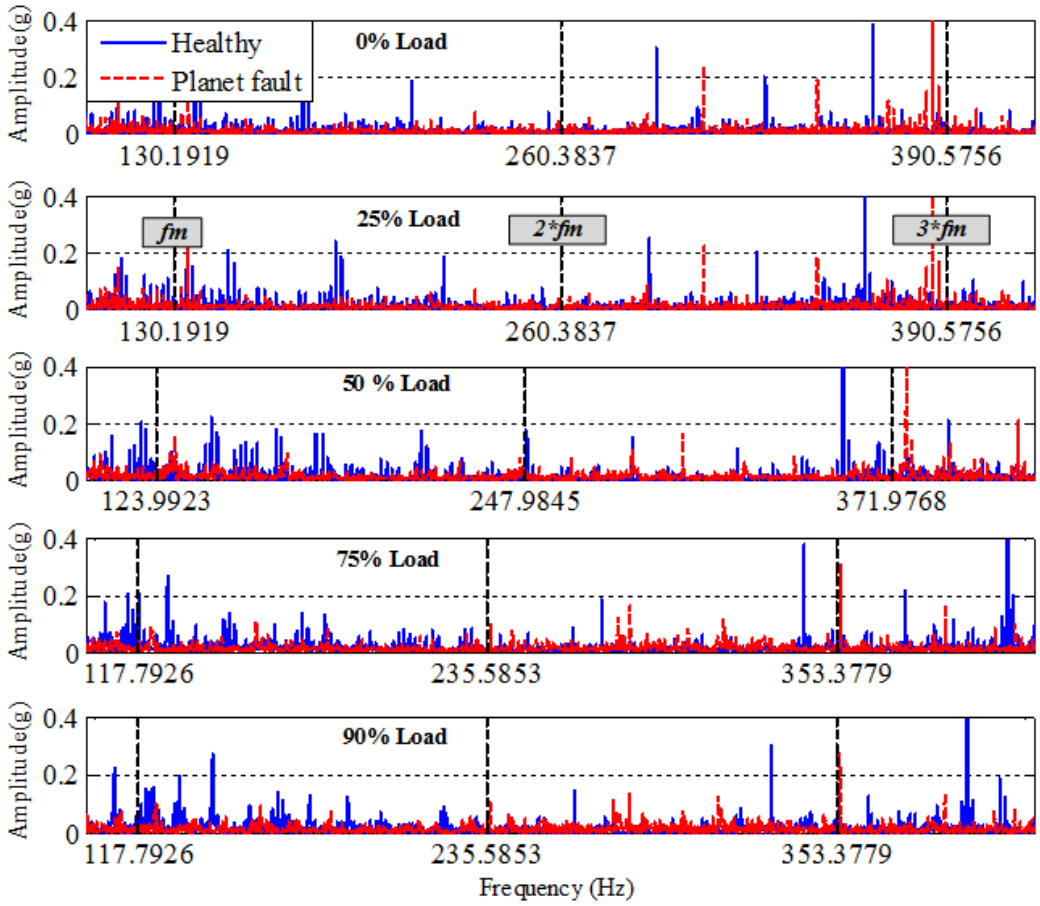

Figure 8-11 Spectrum in the high frequency range for the healthy and planet fault cases

To evaluate the on-rotor MEMS accelerometer performance, a conventional accelerometer was also installed on the gear housing to measure the overall vibration signals. The performance of the on-rotor MEMS accelerometer deployed on the planetary gearbox is investigated by examining the peak values at the corresponding characteristic frequencies for planetary gearbox. Figure 8-12 shows the amplitude change of the vibration signal at f_{sf} with the load for both data acquired by AX3 and fixed accelerometer. From this figure, it can be seen that the amplitudes at f_{sf} of the planetary gear with sun gear fault at different load conditions are higher than that of the healthy planetary gearbox which implies that this feature can be used to indicate the sun fault. However, the fixed accelerometer cannot indicate the fault at the load of 50%.

The harmonic sidebands around the 3rd meshing frequency were also examined and some distinctive peak components were found and could be used for fault diagnosis. The amplitudes

of $3f_{pm}$-f_{rs}, $3f_{pm}$+frs, 3 fpm+fsf, and $3fpm$-fsf changing with the load are presented in Figures 8-13, 8-14, 8-15 and 8-16. It is noticeable that the sun gear fault can be clearly indicated providing an accurate, cheaper and reliable method for planetary gearbox condition monitoring.

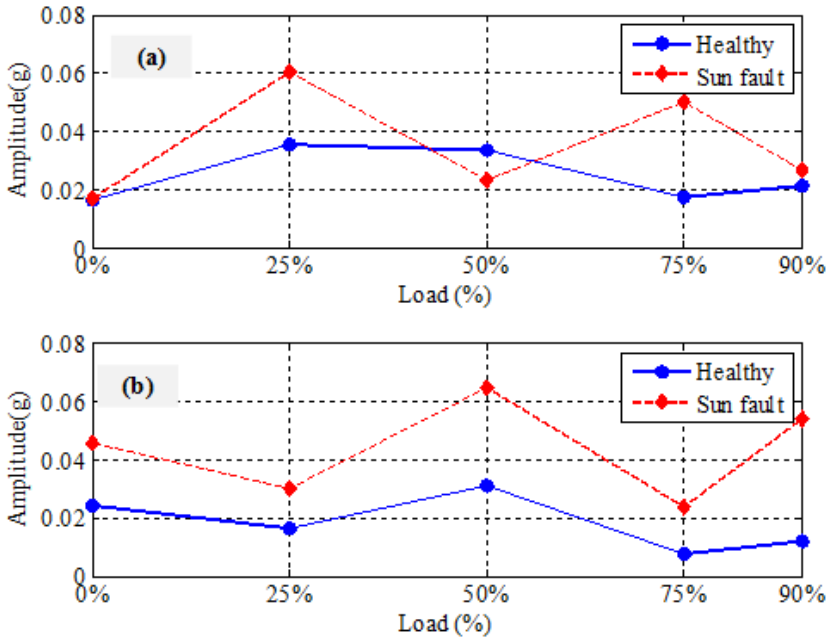

Figure 8-12 Amplitude of acceleration signal at the sun gear fault frequency vs. load (a) Fixed accelerometer and (b) MEMS

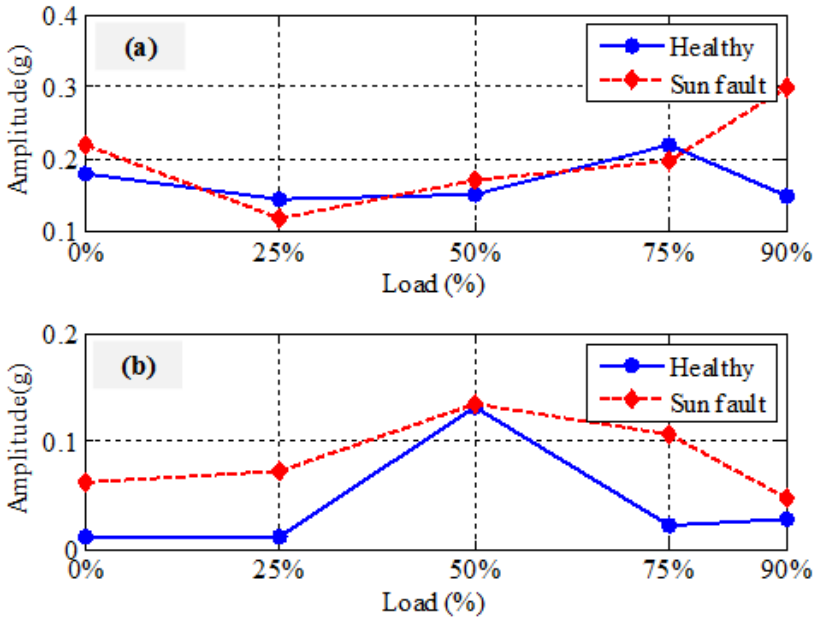

Figure 8-13 Amplitude of acceleration signal at $3f_{pm}$+frs frequency vs. load (a) Fixed accelerometer and (b) MEMS

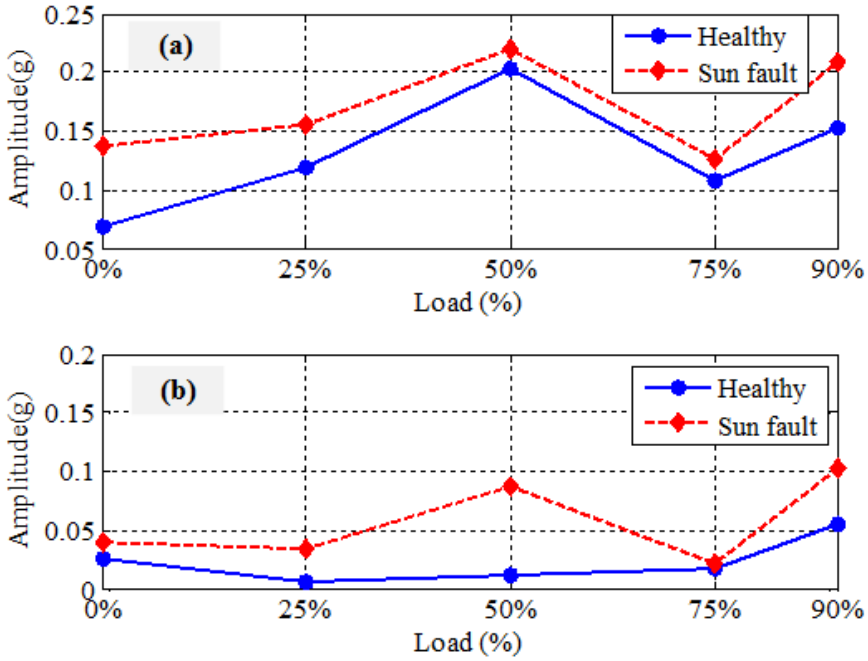

Figure 8-14 Amplitude of acceleration signal at $3f_{pm}$-f_{rs} frequency vs. load (a) Fixed accelerometer and (b) MEMS

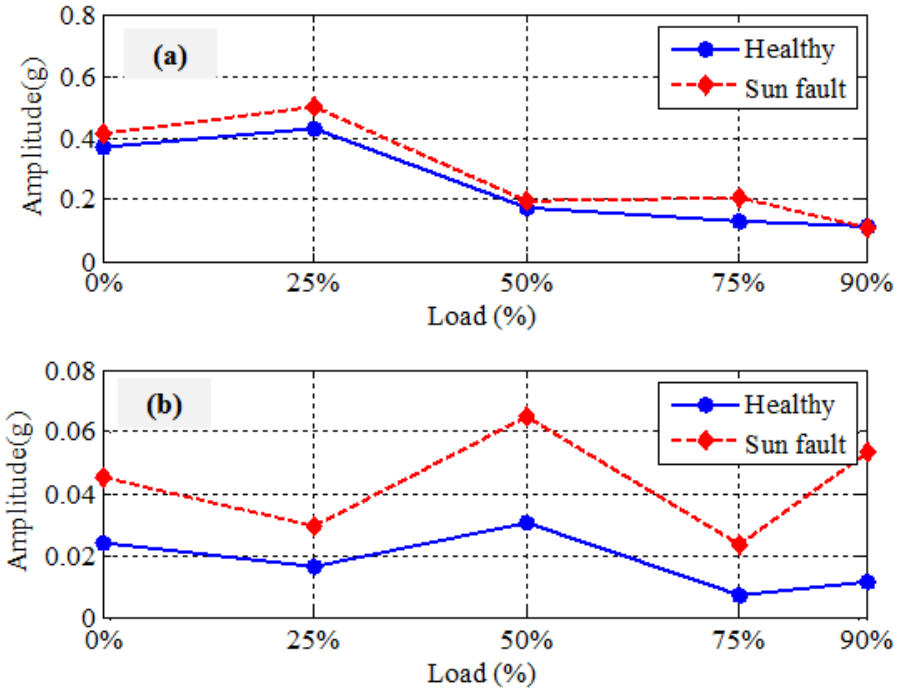

Figure 8-15 Amplitude of acceleration signal at $3f_{pm}$-f_{sf} frequency vs. load (a) Fixed accelerometer and (b) MEMS

The analysis of the performance-data obtained from the on-rotor MEMS accelerometer attached on the planetory gearbox can be investigated by the corresponding peak values at the characteristic frequencies in low range of the gearbox. Figure 8-16 represents the sun gear fault frequency amplitudes whereas Figure 8-17 shows its 2nd harmonic with the change in percentage load. From the analysis it can be seen that the fault frequency amplitudes at f_{sf} and $2f_{sf}$ are higher than the healthy sun gear of the planetary gearbox, thus making the method suitable to find out the sun gear fault from the gearbox system.

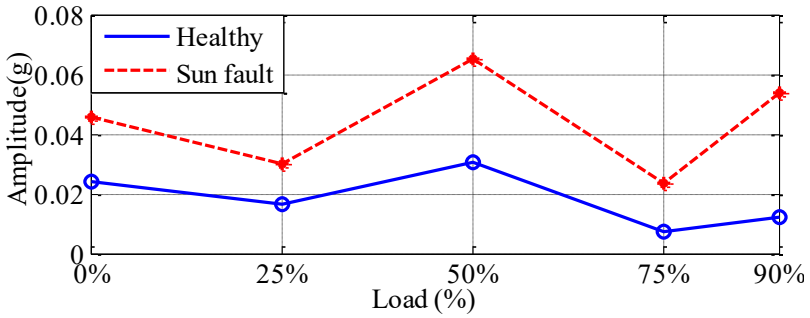

Figure 8-16 Amplitude of acceleration signal at the sun gear fault frequency vs. load

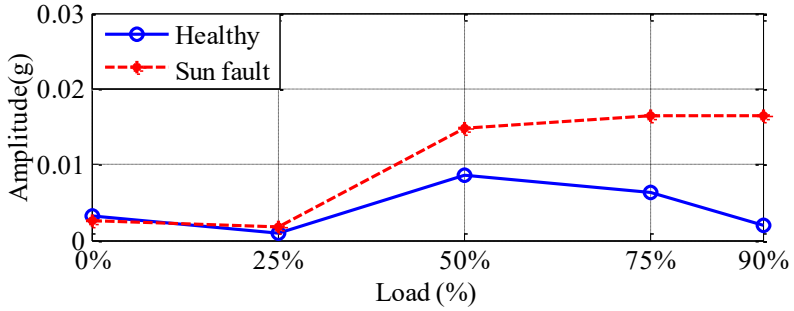

Figure 8-17 Amplitude of acceleration signal at the 2nd harmonics of sun gear fault frequency vs. load

A new feature parameter for the condition monitoring of planetary gear box is introduced by measuring the average of the sun fault frequency and its 2nd harmonics.

$$A_{sun} = \frac{A_{fsf} + A_{2\,fsf}}{2} \tag{8-3}$$

where A_{fsf}, $A_{2\,fsf}$ are the amplitudes of the sun gear fault frequency and its 2nd harmonic respectively. A_{sun} is the average value of both amplitudes.

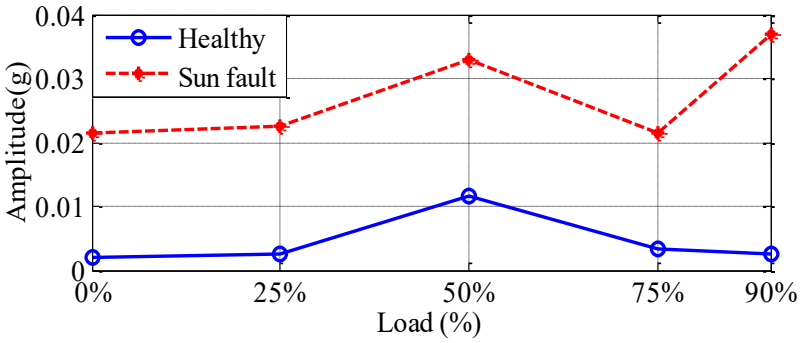

Figure 8-18 Average amplitude for sun fault under different loads

Figure 8-18 represents the average spectral value A_{avg} for the healthy condition and the faulty conditions with the breakage of the tooth in sun gear. From the figure it can be found that both the conditions can be seperated successfully.

To figure out the impact more closely in the planet gear, the planet fault frequency and its 2nd harmonics are presented against the various loads in Figure 8-19 and Figure 8-20 respectively. The analysis results show that these two peaks can successfully diagnose the health conditions of the planet gear in the plantary gearbox system.

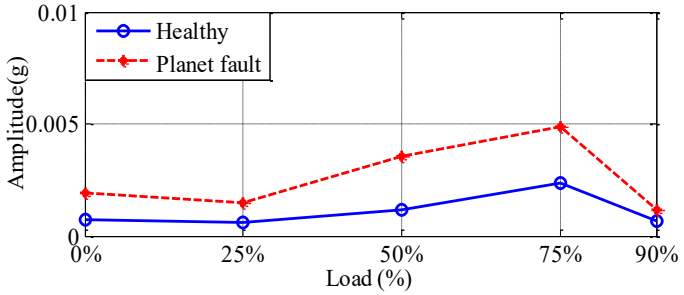

Figure 8-19 Amplitude of acceleration signal at the planet gear fault frequency vs. load

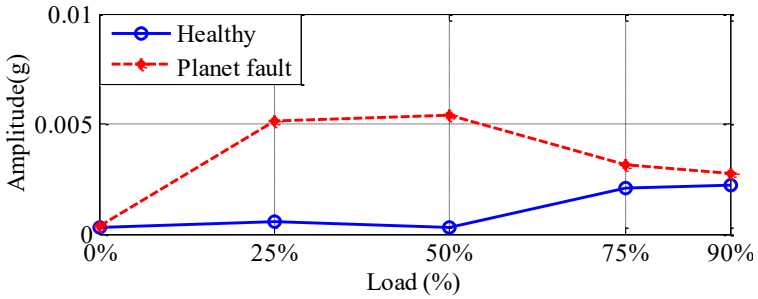

Figure 8-20 Amplitude of acceleration signal at the 2nd harmonic of the planet gear fault frequency vs. load

Similar to the sun gear fault case, the proposed new parameter is also applied for the monitoring of planet gear fault in the planetary gearbox. This time the average spectral value presented in Equation 8-4 is obtained by calculating the average of the planet gear fault frequwncy and its 2nd harmonic.

$$B_{planet} = \frac{B_{fpf} + B_{2\,fpf}}{2} \tag{8-4}$$

where B_{fpf} , $B_{2\,fpf}$ are the amplitudes of the planet fault frequency and its 2nd harmonic respectively. B_{planet} is the average value of both the frequency amplitudes.

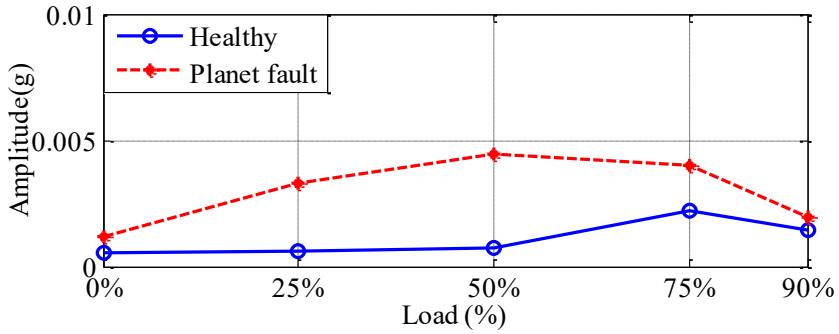

Figure 8-21 Aveage amplitude for planet fault under different loads

Figure 8-21 represents the average spectral value B_{avg} for the healthy condition and the faulty conditions with the breakage of the tooth in planet gear. From the figure it can be found that both the conditions can be seperated successfully.

The experimental results show that the acceleration measurement sensed by on-rotor MEMS accelerometer outperforms the vibration results obtained by the fixed accelerometers, which makes the proposed on-rotor method a good alternative for the fixed accelerometer used in monitoring the condition of the planetary gearboxes.

8.4 Summary

This chapter has introduced a novel method for planetary gearbox condition monitoring and fault diagnosis. It is based on MEMS accelerometers mounted on the shaft to collect the on-rotor dynamics. Based on the findings, the on-rotor accelerations signal can clearly indicate both faults seeded in this work. Moreover, from the comparison results obtained from the fixed

accelerometer and AX3, it is noticeable that the on-rotor acceleration measurement outperformes the vibration acquired by a conventional accelerometers, which clearly indicates that the on-rotor method could be a good and cheap alternative for the fixed accelerometer used for planetary gear box condition monitoring.

CHAPTER 9 CONCLUSION AND FUTURE WORK

This chapter summarizes the significant outcomes from the study and draws inferences based on the results presented in this thesis. It gives a brief summary of the contributions to the knowledge achieved by the research. Finally, several recommendations are suggested for the future work on the usage of a wireless MEMS accelerometer as an on-rotor accelerometer.

9.1 Review of Aim, Objectives and Achievements

This chapter begins with a description of the achievements and novel contributions to the knowledge gained from this work. The target of the research is to use wireless MEMS accelerometer for the machinery condition monitoring and fault diagnosis. The central outcomes of the work are presented below in the same sequence appeared in Section 1.5.

Objective one: To review the popular condition monitoring techniques used in industrial environment and to find an efficient method to monitor the health grade of both the reciprocating compressor and the planetary gearbox.

Achievement one: Some techniques used for machinery condition monitoring have been investigated in chapter one. From this review, it has been found that the vibration is one of the most common techniques employed in the industrial environment due to its susceptibility to the abnormal machinery conditions, providing a reliable way to find the faults at an early stage.

Objective two: Review of the MEMS technology and the availability of the accelerometers that can be used for on-rotor measurements based on that technology.

Achievement two: Information provided in chapter three explained the benefits of MEMS technology and its feasibility in easy monitoring of the rotating machine by mounting a tiny wireless MEMS sensor directly on the rotor has been demonstrated. In this work, ADXL345 is selected to measure on- rotor accelerations because of its small size and cost effectiveness. It also has an advantage of measuring three acceleration inputs along the Cartesian coordinates.

Objective three: Investigate the different wireless protocols that can be used in wireless condition monitoring and study the merits and demerits of the each protocol. Also define how to select a suitable protocol for various applications.

Achievement three: The investigation shown in chapter three explains that the different protocols have been designed for wireless communications to meet unique requirements needed in various applications. Considering WSN applications, the most applicable standards are IEEE802.15.1 and IEEE802.15.4. Meanwhile, industrial machinery runs in a harsh environment for, and the difficulties involved in this environment need to be taken into account when selecting the best data transmission approach.

Objective four: Study the mathematical model of the rotating acceleration and develop a signal processing method to extract the true tangential signal by eliminating the effect of gravity signal in the rotor dynamics.

Achievement four: Chapter three provides the basic information about the acceleration signals measured from the on-rotor MEMS outputs and its mathematical model. A novel method based on Hilbert Transform has been introduced to remove the gravitational acceleration.

Objective five: Benchmark the performance of the reconstructed signals for the condition monitoring of rotating machines.

Achievement five: For performance evaluation of the reconstructed signals, an experimental work was carried out on a two-stage reciprocating compressor. The findings presented in chapter five show that the different health conditions of compressor can be efficiently identified and the simulated faults can be diagnosed efficiently using an on-rotor MEMS accelerometer.

Objective six: Achieve a remote condition monitoring technique for a reciprocating compressor by using wireless MEMS accelerometer.

Achievement six: In chapter six, the data collection method was improved by bringing in the wireless data transmission technique in which the BLE protocol was chosen to send the on-rotor MEMS measurements.

Furthermore, a remote condition monitoring and common fault diagnostic method for the reciprocating compressor has been proposed by using only one MEMS accelerometer.

Objective seven: Measure the IAS signal from the reciprocating compressor using an optical encoder and compare the results with that obtained from the on-rotor MEMS accelerometer.

Achievement seven: The optical encoder was used to benchmark the on-rotor MEMS accelerometer. From findings shown in chapter six, it is found that the IAS signal calculated using the reconstructed tangential acceleration from the wireless MEMS sensor is similar with the signal obtained from the traditional encoder and there is an explicit agreement in both waveform and spectrum, giving evidence that the reconstructed tangential acceleration from the on-rotor accelerometer is accurate and reliable.

Objective eight: Comparison between the two methods used to eliminate the gravitational acceleration projection effect.

Achievement eight: The particulars of the one MEMS method has been discussed in chapter three whereas the two MEMS accelerometers method has been presented in chapter seven. A comparative study can be found from the results obtained by using these methods. At the end, the one MEMS sensor method outperform the other method with lower error range though both methods provide very similar results in term of waveform shapes, amplitudes and frequency components.

Objective nine: Introduce a novel method for planetary gearbox condition monitoring by measuring the acceleration signals with the help of MEMS accelerometer.

Achievement nine: A new method for planetary gearbox condition monitoring has been suggested in chapter eight. It is based on the MEMS accelerometers installed on the shaft to measure the on-rotor dynamics. Based on the experimental results, the on-rotor acceleration signal clearly indicates the faults seeded in this study.

Objective ten: Evaluate the performance of the on-rotor measurement for planetary gearbox condition monitoring by comparing it with the vibration based measurement obtained by a conventional fixed accelerometer.

Achievement ten: From the comparison results obtained from the fixed accelerometer installed on the housing and AX3 attached on the low-speed input shaft and presented in chapter eight, it is confirmed that the on-rotor acceleration measurement outperformed the vibration based measurement, which implies that the on-rotor method can be a good and cheap alternative for the fixed accelerometer used for planetary gear box condition monitoring.

9.2 Conclusions

This study investigates the application of employing MEMS accelerometers for measuring on-rotor accelerations. By employing this technique, it is possible to reduce the cost of the condition monitoring and fault diagnostics for rotating machinery significantly. Based on the investigations from the theoretical and experimental work achieved in this thesis, the following key conclusions have been drawn:

1) This research introduces the mathematical model of the rotating acceleration and an effective signal processing method is presented to extract the true tangential signal by eliminating the effect of gravity signal in the rotor dynamics.

2) Experimental results obtained from the data acquired by AX3 data logger sensor confirm that the reconstructed signals can be effectively used to indicate different faults occurred in a reciprocating compressor.

3) A performance test of a wireless MEMS accelerometer is carried out for different faults simulated in a reciprocating compressor. The measured signals from the wireless sensor are compared with the signals obtained from a traditional optical encoder.

4) The experimental results demonstrate that the acceleration signals from the wireless sensor and the encoder are similar to each other and there is a very good matching in both waveform and spectrum, indicating that the reconstructed tangential acceleration from on-rotor accelerometer is accurate and reliable.

5) Furthermore, a remote condition monitoring technique for fault diagnosis of a reciprocating compressor can be achieved by using a wireless MEMS accelerometer.

6) Based on the experimental results, by installing just one wireless sensor on the flywheel, the different faults can be diagnosed over a wide operating pressure range which makes this method very effective and efficient in wireless condition monitoring and fault diagnostic.

7) Based on the experimental results, the on-rotor acceleration signals can clearly indicate the fault seeded in this work. Moreover, from the comparison results obtained from the fixed accelerometer and AX3, it is noticeable that the on-rotor acceleration measurement outperformed the vibration acquired by a conventional accelerometer, which means the on-rotor method could be a good and cheap alternative for the fixed accelerometer used for the planetary gear box condition monitoring.

9.3 Contributions to Knowledge

First Contribution: The mathematical model of on-rotor MEMS accelerometer and the method used to take away the gravitational projection signals has not been studied previously. Besides this obtaining the tangential acceleration useful for the condition monitoring of rotating machines is the significant contribution.

Second Contribution: The first and third harmonics of the tangential acceleration signatures are sufficiently accurate to monitor the full operating range of a two cylinder reciprocating compressor machine.

Third Contribution: The IAS calculation using tangential acceleration signals aquired by a wireless MEMS accelerometer is reliable and accurate, compared to the conventional IAS measurement and this is a novel contribution for monitoring reciprocating compressor condition.

Fourth Contribution: The fault detection and diagnosis of the planetary gearbox using MEMS accelerometer produces more relaible diagnostic information, both the tangential and centripetal accelerations from the on-rotor MEMS accelerometer on carrier shaft show the higher signal to noise ratio (SNR) for monitoring a planetary gearbox with low rotational responses.This has not been included in any previous research.

9.4 Recommended Future Work on Wireless MEMS Accelerometer

Recommendation 1:

In the current work, Lithium-ion battery is employed to power the sensor with the Bluetooth module. This battery is rechargeable and can be used up to six months in the connection mode. It will be really good if a wireless charger or harvesting can be implemented.

Recommendation 2:

Implementation of the reconstructed tangential acceleration from the sensor node and transmit it to the wireless module with minimum bandwidth requirement.

Recommendation 3:

Investigation of the embedded schemes on the sensor nodes to perform IAS for the diagnostic purpose.

Recommendation 4:

An application based on Android operating system might be developed to receive and display the accelerations collected by the on-rotor sensor node. With the recent technological development of smart phones or tablets, it could be the promising computation and visualization platform for condition monitoring.

Recommendation 5: The on-rotor MEMS accelerometer used in this work has three outputs and only the signals in both tangential and radial (X-axis and Y-axis) directions have been used to show machine conditions. More investigations could be carried out by examining the on-rotor MEMS accelerometer output in Z direction or axil direction as it may give more comprehensive information regarding to the dynamics of whole rotor system and hence more accurate diagnostics.

REFERENCES

1. Yang, Z.M., D. Djurdjanovic, and J. Ni, *Maintenance scheduling in manufacturing systems based on predicted machine degradation.* Journal of intelligent manufacturing, 2008. **19**(1): p. 87-98.
2. Eti, M.C., S. Ogaji, and S. Probert, *Reducing the cost of preventive maintenance (PM) through adopting a proactive reliability-focused culture.* Applied energy, 2006. **83**(11): p. 1235-1248.
3. Salonen, A. and M. Deleryd, *Cost of poor maintenance: A concept for maintenance performance improvement.* Journal of Quality in Maintenance Engineering, 2011. **17**(1): p. 63-73.
4. Ahmad, R. and S. Kamaruddin, *An overview of time-based and condition-based maintenance in industrial application.* Computers & Industrial Engineering, 2012. **63**(1): p. 135-149.
5. Márquez, F.P.G., A.M. Tobias, J.M.P. Pérez, and M. Papaelias, *Condition monitoring of wind turbines: Techniques and methods.* Renewable Energy, 2012. **46**: p. 169-178.
6. Yam, R., P. Tse, L. Li, and P. Tu, *Intelligent predictive decision support system for condition-based maintenance.* The International Journal of Advanced Manufacturing Technology, 2001. **17**(5): p. 383-391.
7. Jardine, A.K., D. Lin, and D. Banjevic, *A review on machinery diagnostics and prognostics implementing condition-based maintenance.* Mechanical systems and signal processing, 2006. **20**(7): p. 1483-1510.
8. Eftekharnejad, B., A. Addali, and D. Mba, *Shaft crack diagnostics in a gearbox.* Applied Acoustics, 2012. **73**(8): p. 723-733.
9. Tsang, A.H., *Condition-based maintenance: tools and decision making.* Journal of Quality in Maintenance Engineering, 1995. **1**(3): p. 3-17.
10. De Silva, C.W., *Vibration monitoring, testing, and instrumentation*. 2007: CRC Press.
11. Wang, L. and R.X. Gao, *Condition monitoring and control for intelligent manufacturing*. 2006: Springer Science & Business Media.
12. Hunt, T.M., *Condition monitoring of mechanical and hydraulic plant: a concise introduction and guide*. 1996: Chapman & Hall.
13. Stander, C. and P. Heyns, *Instantaneous angular speed monitoring of gearboxes under non-cyclic stationary load conditions.* Mechanical Systems and Signal Processing, 2005. **19**(4): p. 817-835.
14. Mones, Z., G. Feng, U. Ogbulaor, T. Wang, F. Gu, and A. Ball. *Performance evaluation of wireless MEMS accelerometer for reciprocating compressor condition monitoring*. in *Power Engineering: Proceedings of the International Conference on Power Transmissions 2016 (ICPT 2016), Chongqing, PR China, 27–30 October 2016*. 2016. Taylor & Francis.
15. Devendiran, S. and K. Manivannan, *Vibration Based Condition Monitoring and Fault Diagnosis Technologies For Bearing and Gear Components-A Review.* International Journal of Applied Engineering Research, 2016. **11**(6): p. 3966-3975.
16. Dalpiaz, G. and A. Rivola, *Condition monitoring and diagnostics in automatic machines: comparison of vibration analysis techniques.* Mechanical Systems and Signal Processing, 1997. **11**(1): p. 53-73.
17. Lebold, M., K. McClintic, R. Campbell, C. Byington, and K. Maynard. *Review of vibration analysis methods for gearbox diagnostics and prognostics*. in *Proceedings of the 54th meeting of the society for machinery failure prevention technology*. 2000.
18. Yoon, J., D. He, B. Van Hecke, T.J. Nostrand, J. Zhu, and E. Bechhoefer, *Vibration-based wind turbine planetary gearbox fault diagnosis using spectral averaging.* Wind Energy, 2016. **19**(9): p. 1733-1747.

19. Randall, R., *A new method of modeling gear faults.* Journal of Mechanical Design, 1982. **104**(2): p. 259-267.
20. Schoen, R.R. and T.G. Habetler, *Effects of time-varying loads on rotor fault detection in induction machines.* IEEE Transactions on Industry Applications, 1995. **31**(4): p. 900-906.
21. Liu, Z., X. Yin, Z. Zhang, D. Chen, and W. Chen, *Online rotor mixed fault diagnosis way based on spectrum analysis of instantaneous power in squirrel cage induction motors.* IEEE Transactions on Energy Conversion, 2004. **19**(3): p. 485-490.
22. Suh, I.-S., *Application of time-frequency representation techniques to the impact-induced noise and vibration from engines*. 2002, SAE Technical Paper.
23. Al-Badour, F., M. Sunar, and L. Cheded, *Vibration analysis of rotating machinery using time–frequency analysis and wavelet techniques.* Mechanical Systems and Signal Processing, 2011. **25**(6): p. 2083-2101.
24. Peng, Z. and F. Chu, *Application of the wavelet transform in machine condition monitoring and fault diagnostics: a review with bibliography*. Mechanical systems and signal processing, 2004. **18**(2): p. 199-221.
25. Atlas, L.E., G.D. Bernard, and S.B. Narayanan, *Applications of time-frequency analysis to signals from manufacturing and machine monitoring sensors.* Proceedings of the IEEE, 1996. **84**(9): p. 1319-1329.
26. Mateo, C. and J.A. Talavera, *Short-Time Fourier Transform with the Window Size Fixed in the Frequency Domain (STFT-FD): Implementation.* SoftwareX, 2017.
27. Nikolaou, N. and I. Antoniadis, *Demodulation of vibration signals generated by defects in rolling element bearings using complex shifted Morlet wavelets.* Mechanical systems and signal processing, 2002. **16**(4): p. 677-694.
28. Yiakopoulos, C. and I. Antoniadis, *Wavelet based demodulation of vibration signals generated by defects in rolling element bearings.* Shock and Vibration, 2002. **9**(6): p. 293-306.
29. Kronland-Martinet, R., J. Morlet, and A. Grossmann, *Analysis of sound patterns through wavelet transforms.* International Journal of Pattern Recognition and Artificial Intelligence, 1987. **1**(02): p. 273-302.
30. Hou, L. and N.W. Bergmann, *Novel industrial wireless sensor networks for machine condition monitoring and fault diagnosis.* IEEE Transactions on Instrumentation and Measurement, 2012. **61**(10): p. 2787-2798.
31. Doe, U., *Industrial wireless technology for the 21st century*. Report, Technology Foresight, Winter, 2004.
32. Mainwaring, A., D. Culler, J. Polastre, R. Szewczyk, and J. Anderson. *Wireless sensor networks for habitat monitoring*. in *Proceedings of the 1st ACM international workshop on Wireless sensor networks and applications*. 2002. Acm.
33. Lynch, J.P., *An overview of wireless structural health monitoring for civil structures.* Philosophical Transactions of the Royal Society of London A: Mathematical, Physical and Engineering Sciences, 2007. **365**(1851): p. 345-372.
34. Carullo, A., S. Corbellini, M. Parvis, and A. Vallan, *A wireless sensor network for cold-chain monitoring.* IEEE Transactions on Instrumentation and Measurement, 2009. **58**(5): p. 1405-1411.
35. Hashemian, H. and W. Strasser. *What you need to know about sensor reliability before and after and accident*. in *IAEA, Vienna, Austria http://www. iaea. org/NuclearPower/Downloadable/Meetings/2011/2011-05-24-05-26-TWGNPPIC/Day-3. Thursday/IC-performance/What-you-need-to-know. pdf [10 August 2014]*. 2011.
36. Bloch, H.P. and J.J. Hoefner, *Reciprocating Compressors:: Operation and Maintenance*. 1996: Gulf Professional Publishing.
37. Brown, R.N., *Compressors: Selection and sizing*. 1997: Gulf Professional Publishing.

38. Kolodziej, J.R. and J.N. Trout, *An image-based pattern recognition approach to condition monitoring of reciprocating compressor valves.* Journal of Vibration and Control, 2017: p. 1077546317726453.
39. Robison, D. and P. Beaty, *Compressor types, Classifications, and Applications.* Online]. Disponível: http://turbolab. tamu. edu/proc/turboproc, 1992. **21**.
40. Saidur, R., N. Rahim, and M. Hasanuzzaman, *A review on compressed-air energy use and energy savings.* Renewable and Sustainable Energy Reviews, 2010. **14**(4): p. 1135-1153.
41. Schmidt, C. and K. Kissock, *Modeling and simulation of air compressor energy use.* 2005.
42. Townsend, J., M.A. Badar, and J. Szekerces, *Updating temperature monitoring on reciprocating compressor connecting rods to improve reliability.* Engineering science and technology, an international journal, 2016. **19**(1): p. 566-573.
43. Robison, D.H. and P.J. Beaty. *Compressor Types, Classifications, And Applications*. in *Proceedings of the 21st Turbomachinery Symposium*. 1992. Texas A&M University. Turbomachinery Laboratories.
44. Mokhatab, S. and W.A. Poe, *Handbook of natural gas transmission and processing*. 2012: Gulf professional publishing.
45. Elhaj, M., F. Gu, A. Ball, A. Albarbar, M. Al-Qattan, and A. Naid, *Numerical simulation and experimental study of a two-stage reciprocating compressor for condition monitoring.* Mechanical Systems and Signal Processing, 2008. **22**(2): p. 374-389.
46. Elhaj, M.A. and A. Ball, *Condition monitoring of reciprocating compressor valves*. 2005: University of Manchester.
47. Albert, M.B., D. Avery, F. Narin, and P. McAllister, *Direct validation of citation counts as indicators of industrially important patents.* Research policy, 1991. **20**(3): p. 251-259.
48. *Integrated publishing*. Available from: http://constructionmanuals.tpub.com/14050/css/Intercoolers-204.htm.
49. P. K. Gupta , S.P.A., N. Gupta, *A Study Based On Design of Air Compressor Intercooler.* International Journal of Research in Aeronautical and Mechanical Engineering, 2013. **1**(7): p. 186-203.
50. AlThobiani, F. and A. Ball, *An approach to fault diagnosis of reciprocating compressor valves using Teager–Kaiser energy operator and deep belief networks.* Expert Systems with Applications, 2014. **41**(9): p. 4113-4122.
51. Brun, K., M.G. Nored, A.J. Smalley, and J.P. Platt. *Reciprocating compressor valve plate life and performance analysis*. in *proceedings of 4th Conference of the EFRC, Antwerp, Belgium*. 2005.
52. Liang, B., F. Gu, and A. Ball, *A preliminary investigation of valve fault diagnosis in reciprocating compressors.* Maintenance & Asset Management Journal, 1996. **11**(2): p. 2-8.
53. Muo, U.E., M. Madamedon, A.D. Ball, and F. Gu. *Wavelet packet analysis and empirical mode decomposition for the fault diagnosis of reciprocating compressors*. in *Automation and Computing (ICAC), 2017 23rd International Conference on*. 2017. IEEE.
54. Ahmed, M., A. Smith, F. Gu, and A. Ball. *Fault diagnosis of reciprocating compressors using revelance vector machines with a genetic algorithm based on vibration data*. in *Automation and Computing (ICAC), 2014 20th International Conference on*. 2014. IEEE.
55. Elhaj, M., M. Almrabet, M. Rgeai, and I. Ehtiwesh, *A combined practical approach to condition monitoring of reciprocating compressors using IAS and dynamic pressure.* World Academy of Science, Engineering and Technology, 2010. **63**(39): p. 186-192.
56. Gu, F. and A. Ball, *Automating the diagnosis of valve faults in reciprocating compressors.* Maintenance & Asset Management Journal, 1996. **11**(3): p. 19-22.
57. Appadoo, R., A. Ball, and F. Gu, *Optimizing condition monitoring techniques applied to a three stage reciprocating compressor in a FMCG industry*. 2010, University of Huddersfield.

58. Naid, A., F.S. Gu, Y.M. Shao, S. Al-Arbi, and A. Ball. *Bispectrum Analysis of Motor Current Signals for Fault Diagnosis of Reciprocating Compressors*. in *Key Engineering Materials*. 2009. Trans Tech Publ.
59. Ahmed, M., S. Abdusslam, M. Baqqar, F. Gu, and A. Ball. *Fault classification of reciprocating compressor based on neural networks and support vector machines*. in *Automation and Computing (ICAC), 2011 17th International Conference on*. 2011. IEEE.
60. Davis, J.R., *Gear materials, properties, and manufacture*. 2005: ASM International.
61. Radzevich, S.P., *Dudley's handbook of practical gear design and manufacture*. 2016: CRC Press.
62. Nice, K. *How Gears Work*. [cited 2018 10.2]; Available from: https://science.howstuffworks.com/transport/engines-equipment/gear2.htm.
63. Budynas, R.G. and J.K. Nisbett, *Shigley's mechanical engineering design*. Vol. 8. 2008: McGraw-Hill New York.
64. Oberg, E., F.D. Jones, H.L. Horton, H.H. Ryffel, and J.H. Geronimo, *Machinery's handbook*. 2016: Industrial Press, Incorporated.
65. Amarnath, M. and I.P. Krishna, *Local fault detection in helical gears via vibration and acoustic signals using EMD based statistical parameter analysis.* Measurement, 2014. **58**: p. 154-164.
66. Van Khang, N., T.M. Cau, and N.P. Dien, *Modelling parametric vibration of gear-pair systems as a tool for aiding gear fault diagnosis.* technische mechanik, 2004. **24**: p. 3-4.
67. Bartelmus, W. *Gearbox damage process*. in *Journal of Physics: Conference Series*. 2011. IOP Publishing.
68. Radzevich, S.P. and D.W. Dudley, *Handbook of practical gear design*. 1994: CRC press.
69. Panwar, V. and S. Mogal, *A case study on various defects found in a gear system.* International Research Journal of Engineering and Technology, 2015. **2**(3): p. 425-9.
70. Joshi, H.D. and K. Kothari, *Mode and Cause of Failure of a Bevel gear-A Review.* International Journal of Advance Engineering and Research Development (IJAERD, 2014. **1**(2): p. 2348-4470.
71. Feng, Y., Y. Qiu, C.J. Crabtree, H. Long, and P.J. Tavner. *Use of SCADA and CMS signals for failure detection and diagnosis of a wind turbine gearbox*. in *European Wind Energy Conference and Exhibition 2011, EWEC 2011*. 2011. Sheffield.
72. NCEL. *Solving Gearbox & Gear Problems*. 2016 [cited 2018 5-2]; Available from: http://www.tribology.co.uk/articles-papers/gearbox-gear-problems/.
73. Lei, Y., D. Han, J. Lin, and Z. He, *Planetary gearbox fault diagnosis using an adaptive stochastic resonance method.* Mechanical Systems and Signal Processing, 2013. **38**(1): p. 113-124.
74. Yoon, J., D. He, B. Van Hecke, T.J. Nostrand, J. Zhu, and E. Bechhoefer. *Planetary Gearbox Fault Diagnosis Using a Single Piezoelectric Strain Sensor*. in *2014 Annual Conference of the Prognostics and Health Management Society, PHM 2014*. 2014. Prognostics and Health Management Society.
75. Chang, Y., E. Aziz, S. Esche, and C. Chassapis, *A framework for developing collaborative training environments for assembling.* Computers in Education Journal, 2013. **23**(4): p. 44-59.
76. Takahashi, T., T. Naraki, and E. Kawahara, *Automatic transmission for vehicle*. 2002, Google Patents.
77. Lewicki, D.G., K.E. LaBerge, R.T. Ehinger, and J. Fetty, *Planetary gearbox fault detection using vibration separation techniques.* 2011.
78. Feng, Z. and M. Liang, *Fault diagnosis of wind turbine planetary gearbox under nonstationary conditions via adaptive optimal kernel time–frequency analysis.* Renewable Energy, 2014. **66**: p. 468-477.
79. Simpson, H.W., *Four speed transmission*. 1958, Google Patents.
80. Lei, Y., J. Lin, M.J. Zuo, and Z. He, *Condition monitoring and fault diagnosis of planetary gearboxes: A review.* Measurement, 2014. **48**: p. 292-305.

81. Blunt, D.M. and J.A. Keller, *Detection of a fatigue crack in a UH-60A planet gear carrier using vibration analysis.* Mechanical Systems and Signal Processing, 2006. **20**(8): p. 2095-2111.
82. Bartelmus, W. and R. Zimroz, *Vibration spectra characteristic frequencies for condition monitoring of mining machinery compound and complex gearboxes*. Prace Naukowe Instytutu Górnictwa Politechniki Wrocławskiej. Studia i Materiały, 2011. **133**(40): p. 17-34.
83. Miao, Q. and Q. Zhou, *Planetary gearbox vibration signal characteristics analysis and fault diagnosis.* Shock and Vibration, 2015. **2015**.
84. Gu, F., G.M. Abdalla, R. Zhang, H. Xun, and A. Ball, *A Novel Method for the Fault Diagnosis of a Planetary Gearbox based on Residual Sidebands from Modulation Signal Bispectrum Analysis.* 2014.
85. Samuel, P.D. and D.J. Pines, *A review of vibration-based techniques for helicopter transmission diagnostics.* Journal of sound and vibration, 2005. **282**(1-2): p. 475-508.
86. Yuksel, C. and A. Kahraman, *Dynamic tooth loads of planetary gear sets having tooth profile wear*. Mechanism and Machine Theory, 2004. **39**(7): p. 695-715.
87. Lei, Y., D. Kong, J. Lin, and M.J. Zuo, *Fault detection of planetary gearboxes using new diagnostic parameters.* Measurement Science and Technology, 2012. **23**(5): p. 055605.
88. Xue, S. and I. Howard, *Torsional vibration signal analysis as a diagnostic tool for planetary gear fault detection.* Mechanical Systems and Signal Processing, 2018. **100**: p. 706-728.
89. Tian, X., G.M. Abdallaa, I. Rehab, F. Gu, A.D. Ball, and T. Wang. *Diagnosis of combination faults in a planetary gearbox using a modulation signal bispectrum based sideband estimator*. in *Automation and Computing (ICAC), 2015 21st International Conference on*. 2015. IEEE.
90. Zeng, Q., M. Zainab, Y. Shao, F. Gu, and A.D. Ball. *Planetary gear fault diagnosis based on instantaneous angular speed analysis*. in *Automation and Computing (ICAC), 2017 23rd International Conference on*. 2017. IEEE.
91. McFadden, P. and J. Smith, *An explanation for the asymmetry of the modulation sidebands about the tooth meshing frequency in epicyclic gear vibration.* Proceedings of the Institution of Mechanical Engineers, Part C: Journal of Mechanical Engineering Science, 1985. **199**(1): p. 65-70.
92. Feng, Z. and M.J. Zuo, *Vibration signal models for fault diagnosis of planetary gearboxes.* Journal of Sound and Vibration, 2012. **331**(22): p. 4919-4939.
93. Hong, L., Y. Qu, Y. Tan, M. Liu, and Z. Zhou, *Vibration Based Diagnosis for Planetary Gearboxes Using an Analytical Model.* Shock and Vibration, 2016. **2016**.
94. Inalpolat, M. and A. Kahraman, *A dynamic model to predict modulation sidebands of a planetary gear set having manufacturing errors*. Journal of Sound and Vibration, 2010. **329**(4): p. 371-393.
95. Robinson, J.C., Z. Czyzewski, and J.W. Pearce, *Wireless machine monitoring and communication system*. 1999, Google Patents.
96. Arebi, L., F. Gu, N. Hu, and A. Ball, *Misalignment detection using a wireless sensor mounted on a rotating shaft.* 2011.
97. Feng, G., N. Hu, Z. Mones, F. Gu, and A. Ball, *An investigation of the orthogonal outputs from an on-rotor MEMS accelerometer for reciprocating compressor condition monitoring*. Mechanical Systems and Signal Processing, 2016. **76**: p. 228-241.
98. Albarbar, A., S. Mekid, A. Starr, and R. Pietruszkiewicz, *Suitability of MEMS accelerometers for condition monitoring: An experimental study.* Sensors, 2008. **8**(2): p. 784-799.
99. Arebi, L., F. Gu, and A. Ball, *Rotor misalignment detection using a wireless sensor and a shaft encoder.* 2010.
100. Baghli, L., J.F. Pautex, and S. Mezani. *Wireless instantaneous torque measurement, application to induction motors*. in *Electrical Machines (ICEM), 2010 XIX International Conference on*. 2010. IEEE.

101. Jiménez, S., M.O. Cole, and P.S. Keogh, *Vibration sensing in smart machine rotors using internal MEMS accelerometers.* Journal of Sound and Vibration, 2016. **377**: p. 58-75.
102. Bao, M., *Analysis and design principles of MEMS devices*. 2005: Elsevier.
103. Bao, M. and W. Wang, *Future of microelectromechanical systems (MEMS).* Sensors and Actuators A: Physical, 1996. **56**(1-2): p. 135-141.
104. Fan, L.-S., Y.-C. Tai, and R.S. Muller, *Integrated movable micromechanical structures for sensors and actuators.* IEEE Transactions on Electron Devices, 1988. **35**(6): p. 724-730.
105. Fan, L.-S., Y.-C. Tai, and R.S. Muller, *IC-processed electrostatic micromotors.* Sensors and actuators, 1989. **20**(1-2): p. 41-47.
106. Andrejašic, M. *Mems accelerometers*. in *University of Ljubljana. Faculty for mathematics and physics, Department of physics, Seminar*. 2008.
107. Tanner, D.M., *MEMS reliability: Where are we now?* Microelectronics reliability, 2009. **49**(9): p. 937-940.
108. Lee, I., G.H. Yoon, J. Park, S. Seok, K. Chun, and K.-I. Lee, *Development and analysis of the vertical capacitive accelerometer.* Sensors and Actuators A: Physical, 2005. **119**(1): p. 8-18.
109. Shaeffer, D.K., *MEMS inertial sensors: A tutorial overview.* IEEE Communications Magazine, 2013. **51**(4): p. 100-109.
110. Kavitha, S., R.J. Daniel, and K. Sumangala, *Design and analysis of MEMS comb drive capacitive accelerometer for SHM and seismic applications.* Measurement, 2016. **93**: p. 327-339.
111. Bernstein, J., *An overview of MEMS inertial sensing technology*. 2003.
112. Ganssle, J., *A Designer's Guide to MEMS Sensors.* Digikey. com [online], 2012. **7**.
113. Feng, G., D. Zhen, M. Aliwan, F. Gu, and A. Ball, *Investigation of wireless protocols for remote condition monitoring.* 2013.
114. Elforjani, B., G. Feng, F. Gu, and A. Ball, *Energy Harvesting Based Wireless Sensor Nodes for The Monitoring Temperature of Gearbox.* 2016.
115. Sarkimaki, V., R. Tiainen, J. Ahola, and T. Lindh. *Wireless technologies in condition monitoring and remote diagnostics of electric drives; requirements and applications*. in *Power Electronics and Applications, 2005 European Conference on*. 2005. IEEE.
116. Sidhu, B., H. Singh, and A. Chhabra, *Emerging wireless standards-wifi, zigbee and wimax.* World Academy of Science, Engineering and Technology, 2007. **25**: p. 308-313.
117. Ferro, E. and F. Potorti, *Bluetooth and Wi-Fi wireless protocols: a survey and a comparison.* IEEE Wireless Communications, 2005. **12**(1): p. 12-26.
118. Townsend, K., C. Cufí, and R. Davidson, *Getting started with Bluetooth low energy: tools and techniques for low-power networking*. 2014: " O'Reilly Media, Inc.".
119. Li, X., D. Li, J. Wan, A.V. Vasilakos, C.-F. Lai, and S. Wang, *A review of industrial wireless networks in the context of industry 4.0.* Wireless networks, 2017. **23**(1): p. 23-41.
120. Pothuganti, K. and A. Chitneni, *A comparative study of wireless protocols: Bluetooth, UWB, ZigBee, and Wi-Fi.* Advance in Electronic and Electric Engineering, 2014. **4**(6): p. 655-662.
121. Lacage, M., M.H. Manshaei, and T. Turletti. *IEEE 802.11 rate adaptation: a practical approach*. in *Proceedings of the 7th ACM international symposium on Modeling, analysis and simulation of wireless and mobile systems*. 2004. ACM.
122. Hashemian, H., *Wireless sensors for predictive maintenance of rotating equipment in research reactors.* Annals of Nuclear Energy, 2011. **38**(2-3): p. 665-680.
123. Ergen, S.C., *ZigBee/IEEE 802.15. 4 Summary, September 2004.* Retrieved April, 2015.
124. Korkua, S.K. and W.-J. Lee. *Wireless sensor network for performance monitoring of electrical machine*. in *North American Power Symposium (NAPS), 2009*. 2009. IEEE.
125. Feng, G.-J., J. Gu, D. Zhen, M. Aliwan, F.-S. Gu, and A.D. Ball, *Implementation of envelope analysis on a wireless condition monitoring system for bearing fault diagnosis.* International Journal of Automation and Computing, 2015. **12**(1): p. 14-24.

126. Aydın, İ., M. Karaköse, and E. Akın, *Combined intelligent methods based on wireless sensor networks for condition monitoring and fault diagnosis.* Journal of Intelligent Manufacturing, 2015. **26**(4): p. 717-729.
127. Aakvaag, N., M. Mathiesen, and G. Thonet. *Timing and power issues in wireless sensor networks-an industrial test case*. in *Parallel Processing, 2005. ICPP 2005 Workshops. International Conference Workshops on*. 2005. IEEE.
128. Gungor, V.C. and G.P. Hancke, *Industrial wireless sensor networks: Challenges, design principles, and technical approaches.* IEEE Transactions on industrial electronics, 2009. **56**(10): p. 4258-4265.
129. Mackensen, E., M. Lai, and T.M. Wendt. *Performance analysis of an Bluetooth Low Energy sensor system*. in *Wireless Systems (IDAACS-SWS), 2012 IEEE 1st International Symposium on*. 2012. IEEE.
130. Patel, V.K. and M.N. Patel, *Development of Smart Sensing Unit for Vibration Measurement by Embedding Accelerometer with the Arduino Microcontroller*. International Journal of Instrumentation Science, 2017. **6**(1): p. 1-7.
131. Lee, J.-S., Y.-W. Su, and C.-C. Shen. *A comparative study of wireless protocols: Bluetooth, UWB, ZigBee, and Wi-Fi*. in *Industrial Electronics Society, 2007. IECON 2007. 33rd Annual Conference of the IEEE*. 2007. Ieee.
132. Gomez, C., J. Oller, and J. Paradells, *Overview and evaluation of bluetooth low energy: An emerging low-power wireless technology.* Sensors, 2012. **12**(9): p. 11734-11753.
133. Siekkinen, M., M. Hiienkari, J.K. Nurminen, and J. Nieminen. *How low energy is bluetooth low energy? comparative measurements with zigbee/802.15. 4*. in *Wireless Communications and Networking Conference Workshops (WCNCW), 2012 IEEE*. 2012. IEEE.
134. Erdelj, M., N. Mitton, and E. Natalizio, *Applications of industrial wireless sensor networks.* Industrial Wireless Sensor Networks: Applications, Protocols, and Standards, 2013: p. 1-22.
135. Lee, S., I. Lee, S. Kim, S. Lee, and A.C. Bovik, *A pervasive network control algorithm for multicamera networks.* IEEE Sensors Journal, 2014. **14**(4): p. 1280-1294.
136. Azevedo, J. and F. Santos, *Energy harvesting from wind and water for autonomous wireless sensor nodes.* IET Circuits, Devices & Systems, 2012. **6**(6): p. 413-420.
137. Zhang, X., J. Fang, F. Meng, and X. Wei, *A novel self-powered wireless sensor node based on energy harvesting for mechanical vibration monitoring.* Mathematical Problems in Engineering, 2014. **2014**.
138. Tan, Y.K. and S.K. Panda, *Energy harvesting from hybrid indoor ambient light and thermal energy sources for enhanced performance of wireless sensor nodes.* IEEE Transactions on Industrial Electronics, 2011. **58**(9): p. 4424-4435.
139. Rodrigues, L.M., C. Montez, G. Budke, F. Vasques, and P. Portugal, *Estimating the Lifetime of Wireless Sensor Network Nodes through the Use of Embedded Analytical Battery Models.* Journal of Sensor and Actuator Networks, 2017. **6**(2): p. 8.
140. Low, K.S., W.N.N. Win, and M.J. Er. *Wireless sensor networks for industrial environments*. in *Computational Intelligence for Modelling, Control and Automation, 2005 and International Conference on Intelligent Agents, Web Technologies and Internet Commerce, International Conference on*. 2005. IEEE.
141. Miao, Q. and V. Makis, *Condition monitoring and classification of rotating machinery using wavelets and hidden Markov models.* Mechanical systems and signal processing, 2007. **21**(2): p. 840-855.
142. Miyachi, T. and K. Seki. *An investigation of the early detection of defects in ball bearings using vibration monitoring, practical limit of detectability and growth speed of defects*. in *Proceedings of the international Conference of Rotordynamics*. 1986.
143. Tandon, N. and B. Nakra, *Detection of defects in rolling element bearings by vibration monitoring.* Indian Journal of Mechanical Engineering Division, 1993. **73**: p. 271-282.

144. Gu, F., X. Tian, Z. Chen, T. Wang, I. Rehab, and A. Ball, *Fault severity diagnosis of rolling element bearings based on kurtogram and envelope analysis*. 2014, Institute of Research Engineers and Doctors.
145. Ogbulafor, U.E., G. Feng, Z. Mones, F. Gu, and A. Ball, *Application of Wavelet Packet Transform and Envelope Analysis to Non-stationary Vibration Signals For Fault Diagnosis of a Reciprocating Compressor*. 2017.
146. Li, B., P.-l. Zhang, Q. Mao, S.-s. Mi, and P.-y. Liu, *Gear fault detection using adaptive morphological gradient lifting wavelet.* Journal of Vibration and Control, 2013. **19**(11): p. 1646-1657.
147. Roy, S.K., A.R. Mohanty, and C.S. Kumar, *Fault detection in a multistage gearbox by time synchronous averaging of the instantaneous angular speed.* Journal of Vibration and Control, 2016. **22**(2): p. 468-480.
148. Li, Y., F. Gu, G. Harris, A. Ball, N. Bennett, and K. Travis, *The measurement of instantaneous angular speed.* Mechanical Systems and Signal Processing, 2005. **19**(4): p. 786-805.
149. Raj, V.P., K. Natarajan, and T. Girikumar. *Induction motor fault detection and diagnosis by vibration analysis using MEMS accelerometer*. in *Emerging Trends in Communication, Control, Signal Processing & Computing Applications (C2SPCA), 2013 International Conference on*. 2013. IEEE.
150. Kumar, P.S., L. Xie, and B.-H. Soong. *Feasibility of wireless RF communication inside rotating electrical machines for condition monitoring applications*. in *Electrical Machines and Systems (ICEMS), 2016 19th International Conference on*. 2016. IEEE.
151. Medina-García, J., T. Sánchez-Rodríguez, J.A.G. Galán, A. Delgado, F. Gómez-Bravo, and R. Jiménez, *A Wireless Sensor System for Real-Time Monitoring and Fault Detection of Motor Arrays.* Sensors, 2017. **17**(3): p. 469.
152. Arebi, L., F. Gu, and A. Ball. *A comparative study of misalignment detection using a novel Wireless Sensor with conventional Wired Sensors*. in *Journal of Physics: Conference Series*. 2012. IOP Publishing.
153. Z. Mones, G.F., X. Tang, U. Haba, F. Gu, A.D. Ball, *A comparative study of gravitational acceleration cancellation from on-rotor MEMS accelerometers for condition monitoring*, in *24th International Congress on Sound and Vibration ICSV*. 2017: London.
154. Gu, F., I. Yesilyurt, Y. Li, G. Harris, and A. Ball, *An investigation of the effects of measurement noise in the use of instantaneous angular speed for machine diagnosis*. Mechanical Systems and Signal Processing, 2006. **20**(6): p. 1444-1460.
155. Axivity, *http://axivity.com/files/resources/AX3_Data_Sheet.pdf*. AX3 Data sheet, 2015.
156. Devices, A., *ADXL345 datasheet.* USA: Analog Devices, 2010.
157. Tierean, M. and L. Baltes. *Design of Valves Used in Reciprocating Compressors*. in *Recent Advances in Applied and Theoretical Mechanics, Proceedings of the 5th WSEAS International Conference on Applied and Theoretical Mechanics (MECHANICS'09)*.
158. Li, B., X. Zhang, and J. Wu, *New procedure for gear fault detection and diagnosis using instantaneous angular speed.* Mechanical Systems and Signal Processing, 2017. **85**: p. 415-428.
159. Renaudin, L., F. Bonnardot, O. Musy, J. Doray, and D. Rémond, *Natural roller bearing fault detection by angular measurement of true instantaneous angular speed.* Mechanical Systems and Signal Processing, 2010. **24**(7): p. 1998-2011.
160. Gubran, A.A. and J.K. Sinha, *Shaft instantaneous angular speed for blade vibration in rotating machine.* Mechanical Systems and Signal Processing, 2014. **44**(1): p. 47-59.
161. Nurmi, J., J. Honkakorpi, J. Vihonen, and J. Mattila. *Micro-electromechanical system sensors in unscented Kalman filter-based condition monitoring of hydraulic systems*. in *Advanced Intelligent Mechatronics (AIM), 2013 IEEE/ASME International Conference on*. 2013. IEEE.
162. Binder, J., *New generation of automotive sensors to fulfil the requirements of fuel economy and emission control.* Sensors and Actuators A: Physical, 1992. **31**(1-3): p. 60-67.

163. Ellin, A. and G. Dolsak, *The design and application of rotary encoders.* Sensor Review, 2008. **28**(2): p. 150-158.
164. Hildebrand, F.B., *Introduction to numerical analysis*. 1987: Courier Corporation.
165. Liu, L., X. Liang, and M.J. Zuo, *Vibration signal modeling of a planetary gear set with transmission path effect analysis.* Measurement, 2016. **85**: p. 20-31.